Unraveling the Mechanisms of Apical Cadherin-Based Adhesion in Brush Border and Junction Assembly

By

Caroline Susanne Cencer

Dissertation

Submitted to the Faculty of the

Graduate School of Vanderbilt University

in partial fulfillment of the requirements

for the degree of

DOCTOR OF PHILOSOPHY

in

Cell and Developmental Biology

December 16, 2023

Nashville, TN

Approved:

Matthew J. Tyska, Ph.D., Advisor

Irina N. Kaverina, Ph.D., Committee Chair

D. Borden Lacy, Ph.D.

Ian G. Macara, Ph.D.

Roy Zent, MD, Ph.D.

DEDICATION

For all the explorers, may you seize your love for discovery and follow it.

ACKNOWLEDGEMENTS

To my scientific mentors: First, to the staff and scientists at the Oakland University Eye Research Institute, thank you for creating a program that gives undergraduates the opportunity to work in a laboratory. The space you have built is such a special outlet for aspiring students to learn about research as a career – I wouldn't have discovered my love for research science without it.

Dr. Giblin, you were the best first research mentor I could've asked for. I appreciate your continued support for me throughout graduate school. It has been so fun to email you over the years to update you on my research successes. Thank you for giving me the chance to work in your laboratory as an undergraduate and to publish my first research paper. My love for microscopy that continues to this day started in your lab. I'll always have fond memories of bringing you data on my flash drive to show you project updates. Even though you thought I was slightly crazy to want to pursue a Ph.D., look at me now! I couldn't have done it without your encouragement.

Matt, quite probably the coolest boss and mentor that I will ever have in life, thank you for being so supportive and being my biggest advocate. You were one of the only PIs that I met with about lab rotations that didn't make me feel anxious or clueless. When I left your office that first time, I texted my friend to say that I was joining your lab even before you told me that you had the room! I'm so glad that you did, because this has been the best graduate school experience that I could have ever wished for. Even at my lowest points, you put faith back into me that I could finish a Ph.D. – I left each one-on-one meeting feeling inspired and excited to do science again. Thank you for always acknowledging my skills and talents, and rest assured that I have passed my brain power on to our other lab members. I wish I could stay and work in your lab forever and I'll miss your funny texts and love of cat memes. Please don't kick me off the group chat.

To my thesis committee, thank you for your insight and advice over the years. I appreciate your wisdom and your contributions truly made a difference in my thesis project. Thank you for taking the time to join me for committee meetings and engaging in enlightening discussions.

To my lab mates: Those past and present, thank you for making my time in the Tyska lab such a memorable one. Aaron, Angelo, Bella, Colbie, Deanna, Gill, Jen, Julissa, Kianna, Leah, Leslie, Meagan, Olivia, Rocio, Suli, and Zach, it is because of wonderful people like you that it is so hard to leave and move on to the next place. At the start, I was scared to join a big lab, coming from such a small undergraduate one, but I am so happy to have known all of you and am certain that I will never have coworkers who feel so much like family. Thank you to everyone for your readiness to help with protocols and donate reagents to my sorry cause. I hope that my microscope troubleshooting was sufficient payment for your trouble. I'll miss watching movies in our joint Airbnbs at conferences and all the fun times had at lab outings. You have all left your mark on my life, and I will never forget you.

To my partner in life: Kevin, I feel so lucky to have had you by my side the last few years of graduate school. Shoutout to Matt and Borden for connecting us on a project and giving me one of the brightest spots in my life. Thank you for your patience and guidance with experiments and putting up with my western blot incompetence. Your knowledge and love for science and constant stream of new ideas is such an inspiration to be around and I am excited to see all the great things you do in the future. Thank you for always believing in me and instilling confidence in me, even when I don't believe in myself. I'll forever be Superwoman posing though life thanks to your encouragement. Cheers to being the raddest pair of PhD's. Love, CC.

To my family: To my nieces Nora, Abigail, Kira, Elizabeth, Amelia, Melanie, and Bonnie, thank you for bringing me so much joy throughout graduate school. May you all grow up with boundless opportunities to learn and explore what you love while knowing that you can do anything and be anyone you want to be! I can't wait to see how your unique personalities and interests take shape as you grow. I'm thrilled that some of you already show a love for frogs and collecting rocks. If you ever want to talk about a career in science, let me know. Wink, wink.

To my siblings and siblings-in-law, we may be separated in age and distance, but I have always felt your support and have appreciated having you along for this ride, sharing in my successes along the way. Bethany and Dave, you inspire me to find and get my dream job; I know everything will work out in the end. We're all in the Ph.D. club now. Jenny and Peter, you remind me to have fun even when there is a lot of work to be done. You both exude a youthful spirit and inspire me to just be an awesome human and do what I love, with no regrets. Jeremy and Ashley, thank you for always being my biggest cheerleaders and being proud of how I have grown more independent throughout graduate school. I know I can go to you whenever I need help and you will drop everything, even with a house full of kids. Shawn and Janet, I love your creativity and how much you appreciate the world around us. You've shown me that it is possible to work hard while still having time to do what you love.

To my parents, words cannot express how thankful I am for all that you have done for me. It is because of you that I had the best education and opportunities to learn. Thank you for letting me pursue my passions, even when they were ever-changing. I know you gave a lot for me, and I promise you that I won't ever take it for granted. Thank you for always celebrating my successes, especially when experiments worked, and papers got published. It means the world to me to have parents who care so much about me.

TABLE OF CONTENTS

LIST OF FIGURES

LIST OF ABBREVIATIONS

ABR	actin binding region
ADP	adenosine diphosphate
ANKS4B	ankyrin repeat and sterile alpha motif domain containing 4B
Arp2/3	actin related protein 2/3
ATP	adenosine triphosphate
BSA	bovine serum albumin
CACO-2_{BBE}	colonic adenocarcinoma cells-2 brush border expressing
CDH1	embryonic (E)-cadherin
CDH2	neural (N)-cadherin
CDH3	placental (P)-cadherin
CDH23	cadherin related family member 23
CDHR2	cadherin related family member 2
CDHR5	cadherin related family member 5
CL4	LLC-PK1-Clone 4 cells
CRISPR	clustered regularly interspaced short palindromic repeats
DPC	days post-confluency
EC	extracellular cadherin
EDTA	ethylenediaminetetraacetic acid
EHEC	enterohemorrhagic *Escherichia coli*
Ena/VASP	enabled/vasodilator-stimulated phosphoprotein
EPEC	enteropathogenic *Escherichia coli*
EPS8	epidermal growth factor pathway substrate 8

ESPN	espin
F-actin	filamentous actin
FRAP	fluorescence recovery after photobleaching
G-actin	globular (monomeric) actin
IBD	inflammatory bowel disease
IMAC	intermicrovillar adhesion complex
IRTKS	insulin receptor tyrosine kinase substrate
JAM	junctional adhesion molecule
K_C	critical concentration
KD	knockdown
KO	knockout
LASER	light amplification by stimulated emission of radiation
LLC-PK1-CL4	Lilly Laboratories Culture-Porcine Kidney 1-Clone 4
LUT	look-up table
MAD	membrane adjacent domain
MaxIP	maximum intensity projection
MISP	mitotic spindle positioning
MLD	mucin-like domain
MYO7B	myosin-7B
NGS	normal goat serum
NM2C	non-muscle myosin-2C
N-WASP	Neural Wiskott–Aldrich syndrome protein
OCT	optimal cutting temperature

PCDH15	protocadherin-15
PDZ	PSD-95/discs large/ZO-1
SEM	scanning electron microscopy
SD	standard deviation
SH3	src homology 3 domain
SIM	structured illumination microscopy
TEER	transepithelial electrical resistance
TH1	tail homology 1
USH1C	Usher syndrome type-1C
WH2	WASP homology 2 domain
WT	wildtype
ZO-1	zonula occludens protein

CHAPTER I

INTRODUCTION

Morphogenesis and the Cytoskeleton

In the late nineteenth century, architect Louis Sullivan coined the phrase "form follows function" (Sullivan, 1896). This principle proposes that a structure's purpose inspires its design. A similar concept can be seen throughout biological tissues, wherein cellular architecture determines a tissue's function. Morphogenesis, or the process in which a cell, tissue, organ, or organism acquires its final shape, is fundamental to building the body. To adapt to their specialized roles in tissues, cells rely on both spatial and mechanical mechanisms that control their shapes. Similar developmental mechanisms have been observed in ancient organisms including algae and choanoflagellates, suggesting that the theme of form follows function is conserved across organisms (Brunet et al., 2019; Katsaros et al., 2006). At the center of this defining process is the cytoskeleton, a family of three protein filaments – actin, microtubules, and intermediate filaments. In concert with force-generating myosin motor proteins, cells use actin-tethered pushing and pulling forces to expand and contract, respectfully. These shape changes ultimately allow cells to transform into higher-order tissue structures (Clarke and Martin, 2021).

Actin Monomers and Filament Polymerization

Actin exists in two forms, monomeric (G-actin) and filamentous (F-actin). Its 42 kDa globular state is expressed as six main isoforms in humans each suited to different functions: $\alpha_{skeletal}$-actin, $\alpha_{cardiac}$-actin, α_{smooth}-actin, and γ_{smooth}-actin, are expressed primarily in skeletal, cardiac, and smooth muscle, while the other isoforms, β_{cyto}-actin and γ_{cyto}-actin, are expressed

across all tissues (Perrin and Ervasti, 2010). G-actin undergoes polymerization to create a filament of F-actin, the building block used to assemble higher order structures that support membranes including lamellipodia, filopodia, stereocilia, and microvilli. However, a single filament only generates ~0.8 pN of force compared to the estimated 30 pN required to deform the plasma membrane (Footer et al., 2007; Mogilner and Rubinstein, 2005). The combined power of bundled filaments and myosin motor proteins, however, can generate enough force to deform membranes and create distinct shapes (Fitz et al., 2023; Kovar and Pollard, 2004).

To build actin networks, actin must first create a stable nucleus of three subunits to pass the lag phase of growth (**Fig. 1-1A**). Two actin subunits have less contacts with each other, making binding relatively weak, while the addition of a third monomer makes sufficient contact to stabilize the nucleus (Sept and McCammon, 2001). This rate-limiting step of stable trimer formation can be sped up by actin nucleators, proteins that facilitate polymerization of branched or straight filaments, such as the Arp2/3 complex and formins, respectfully (Firat-Karalar and Welch, 2011).

The next stage, the growth phase, can then begin during which the actin filament polymerizes and elongates. Asymmetric actin subunits in the filament cause each end to have a different structure, creating a polarized structure with a barbed (-) end and pointed (+) end, named for their appearance when coated with myosin subfragment-1. This difference in turn causes the two filament ends to grow at different rates (Pollard and Borisy, 2003). The rates of actin monomer association and disassociation (k_{on} and k_{off}, respectfully) are larger at the plus, fast-growing end vs. the minus, slow-growing end (Pollard, 1986). This process is tightly controlled by ATP binding and hydrolysis in which added monomers bound to ATP undergo hydrolysis as they move through the filament. When phosphate (P_i) is released, the filament is destabilized, and the ADP-bound monomers readily dissociate (**Fig. 1-1A**) (Carlier, 1990). Additionally, the actin critical

concentration (K_C), or the G-actin concentration above which actin filament assembly will take place, is approximately fivefold higher at the pointed end versus the barbed end (0.6 μM vs 0.12 μM) (Pollard, 1986). An interesting phenomenon occurs, however, when the free G-actin monomer concentration is greater than the K_C of the barbed end, but less than the K_C for the pointed end ($K_{C\ barbed} < [\text{G-actin}] < K_{C\ pointed}$). This allows the actin filament to reach a steady state during which the number of subunits coming on to one end of the filament is equal to the number coming off the other, called treadmilling (Wegner, 1976). This net flux of subunits through the actin filament is also the driving mechanism for cellular and actin-based structure motility (**Fig. 1-1B**) (Meenderink et al., 2019; Pantaloni et al., 2001; Pollard and Borisy, 2003).

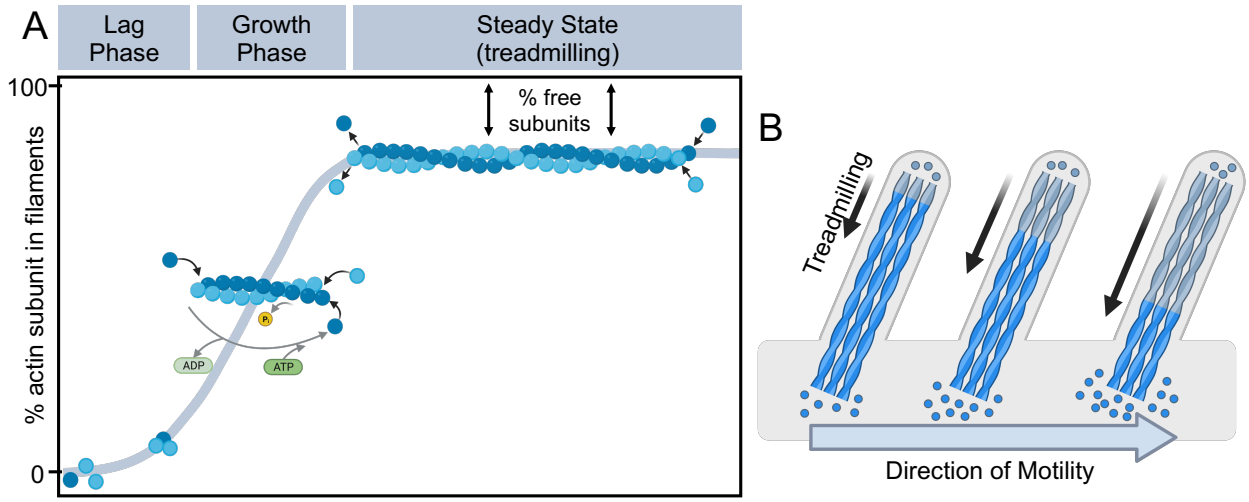

Figure 1-1. The process and function of actin polymerization in microvillar motility.
(**A**) Actin polymerization must surpass an initial lag phase by forming a stable nucleus of three monomers to which ATP-actin monomers are added. ATP hydrolysis drives the flux of monomers through the filament. Treadmilling occurs when the number of monomers added at one end is equal the number leaving the other end, creating a steady state. (**B**) Model for how treadmilling propels actin-based microvilli protrusions across the apical cell surface, driving their motility.

Actin-based Protrusions

Actin networks come in different architectures, branched and linear. Lamellipodia at the leading edge of motile cells are supported by a branched network (**Figure 1-2A**), nucleated by the

actin related protein 2/3 (Arp2/3) complex which upon activation by a nucleation promoting factor, such as N-WASP, binds to preexisting filaments and mimics a new barbed end from which monomers can polymerize (Suraneni et al., 2012; Volkmann et al., 2001). Filopodia, on the other hand, protrude outwards from this branched network, reinforced by linear actin filaments elongated by formin proteins and Enabled/Vasodilator-Stimulated Phosphoprotein (Ena/VASP) (Paul and Pollard, 2009; Winkelman et al., 2014).

Another linear actin-based protrusion, stereocilia, exist within the inner ear on the surface of hair cells (**Figure 1-2B**). Arranged in a staircase pattern of three rows of increasing heights, stereocilia are deflected by sound, causing mechanotransduction channels to open sending electrical signals to the auditory nerve for processing (Hudspeth, 1985; Tilney et al., 1992). Stereocilia core actin bundles are estimated to contain hundreds of filaments at their distal tips tapering down to only ~30 filaments at their base (Tilney and DeRosier, 1986; Tilney et al., 1980). This makes them quite large protrusions with a length of 1-120 μm and diameter of 100-500 nm, depending on row arrangement (Engstrom and Engstrom, 1978; Manor and Kachar, 2008).

Lastly, microvilli situated on the surface of transporting epithelial cells present as 1 μm long by 100 nm wide protrusions with a core bundle of 20-40 linear actin filaments enveloped in apical cell membrane (**Figure 1-2C**) (Mooseker and Tilney, 1975; Ohta et al., 2012). Thousands of microvilli exist on the surface of each cell, amplifying surface area in tissues that require optimization for absorptive functions, which will be discussed in more detail in the next section.

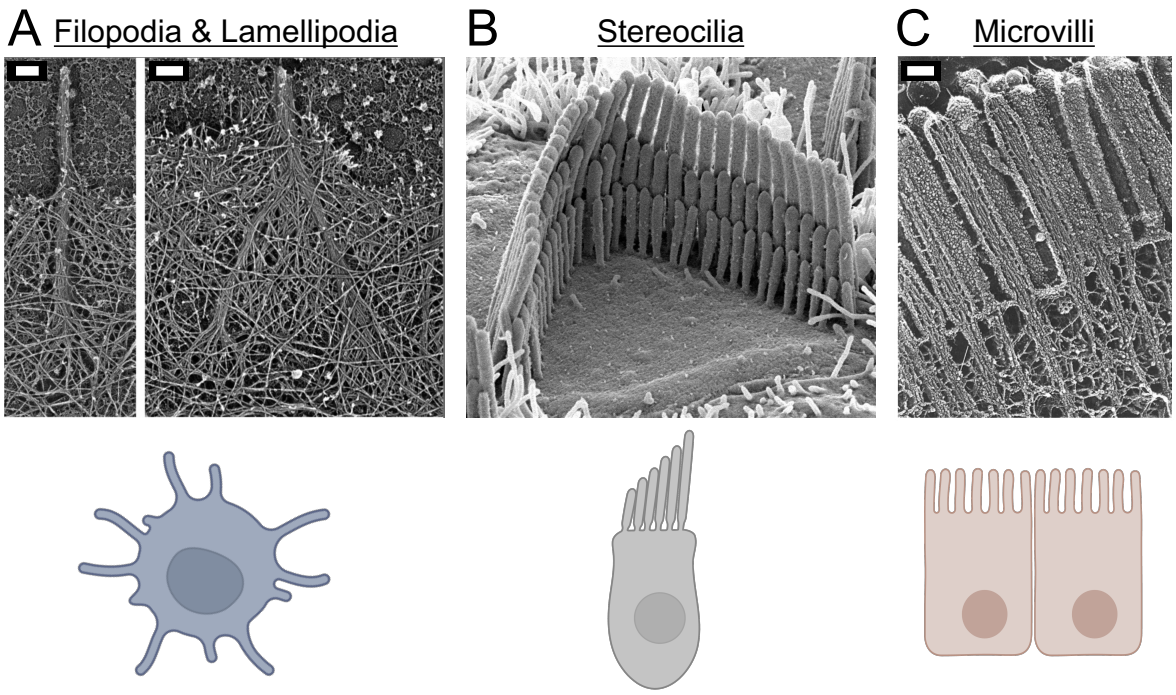

Figure 1-2. Parallel actin bundles can be found in various specialized cell structures. (**A**) Protruding from the cell edge, filopodia and lamellipodia are built from linear and branched actin networks, respectfully. Figure adapted from (Svitkina et al., 2003) Scale bars represent 200 nm. (**B**) Stereocilia exhibit a staircase pattern and are examples of linear actin-based protrusions. [Hair cell of inner ear. Dr David Furness. Attribution-NonCommercial 4.0 International (CC BY-NC 4.0). Source: Wellcome Collection.] (**C**) Microvilli on the surface of transporting epithelial cells also contain linear actin filament bundles. Figure adapted from (Hirokawa et al., 1982). Scale bar represents 100 nm.

Transporting Epithelia

Epithelial sheets can be found in tissues throughout the body that form a barrier between the internal and external environments (Honda, 2017). Transporting epithelia are made up of polarized epithelial cells that create tight intercellular contacts, or junctions, and control the movement of solutes between cells (paracellular) and across the membrane (transcellular) with various apical membrane transporters (Garcia-Castillo et al., 2017).

Transporting epithelial cells can be found in the small intestine, a hollow tube comprised of three sections: the duodenum, the jejunum, and the ileum from proximal to distal. The intestinal

epithelial sheet is molded into upright fingerlike folds called villi, interspersed with deep stem cell containing crypts (**Fig. 1-3A-B**). As the primary location for nutrient absorption, the small intestine is largely home to absorptive cells called enterocytes which harbor thousands of apical microvilli that collectively form the brush border. Together, villi and microvilli expand the membrane surface area available for absorption to an estimated 30-40 m^2 in humans (Helander and Fandriks, 2014).

The intestinal epithelium is unique in that it self-regenerates, renewing its cells over the course of 3-5 days. Lgr5+ stem cells within the crypts give rise to transit-amplifying cells, that migrate as they divide before differentiating into mature villus cells (**Fig. 1-3B-C**) (Krndija et al., 2019; van der Flier and Clevers, 2009). This cell division cycle was classically considered to control the conveyor belt movement of cells from villus base to tip, however, recent evidence suggests that the cells may also implement basal actin-rich "feet" to actively migrate (Krndija et al., 2019). Once reaching the tip of the villus, the cells undergo apoptosis and are extruded into the lumen. This, in turn, helps control the rate of crypt cell proliferation and provide balance to the regenerating epithelium (Hall et al., 1994). Interestingly, the apical morphology of immature transit-amplifying cells is distinct from mature enterocytes. While cells on the villus contain a hexagonally packed and organized brush border, transit-amplifying cell surfaces are sparse, with few microvilli (**Fig. 1-3C**) (Cencer et al., 2023; Crawley et al., 2014a). The stark transition between these two domains has created a persistent question of how microvilli become organized in time to create a functionally mature brush border.

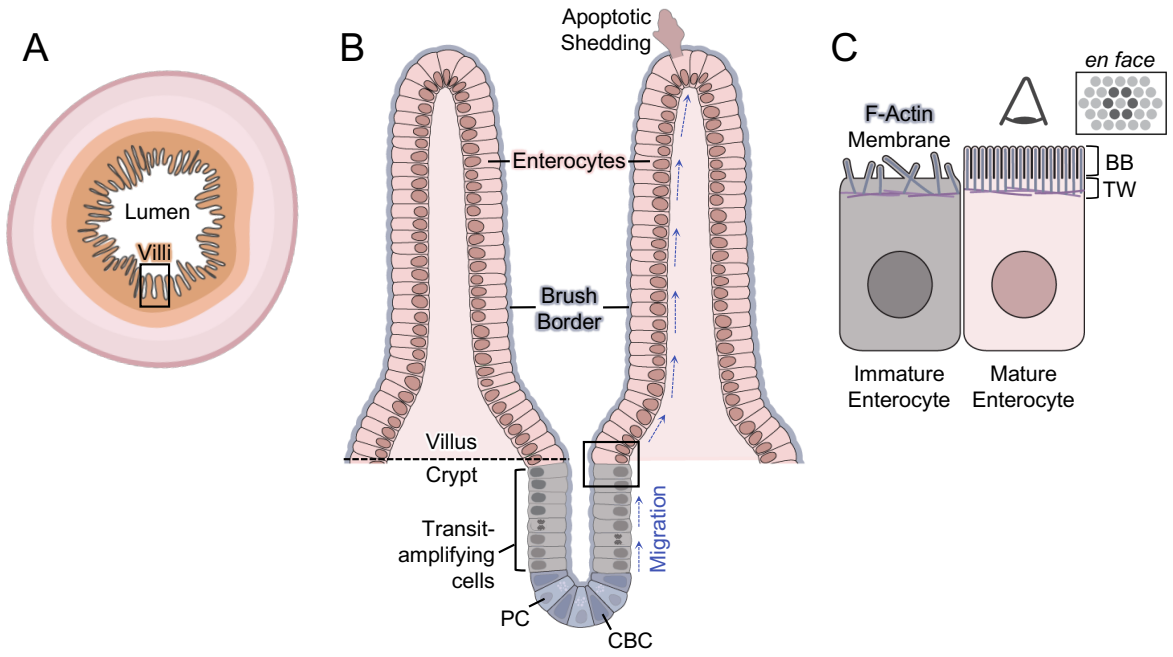

Figure 1-3. Organization of the intestinal epithelium across scale. (**A**) Cross-section of the small intestine highlighting the central lumen and villi, finger like tissue folds protruding into the lumen and increase surface area. (**B**) Enlarged view of two adjacent villi and an intestinal crypt in cross-section. The crypt houses the stem cell niche comprised of proliferative crypt base columnar (CBC) cells and Paneth cells (PC). Cells divide and migrate up the crypt-villus axis, differentiating into multiple cell types with the most common type being enterocytes. Over the course of 3-5 days, the intestinal epithelium is replaced as old cells undergo apoptosis and are shed at the villus apex. (**C**) The apical surface of enterocytes is packed with actin-supported membrane protrusions called microvilli. Collective microvilli of the intestine make up the brush border (BB) and are anchored in the terminal web (TW). Apical surface organization changes dramatically across the crypt-villus axis, with *en face* view of the brush border revealing a hexagonal packing pattern. Schematic adapted from (Crawley et al., 2014a).

As another major site of solute uptake in the body, the kidney contains transporting epithelial cells that also rely on an apical brush border for optimal function. The kidney's main function is to filter the blood, balancing fluid and electrolytes while eliminating waste through urine. The kidney proximal tubule within the nephron is full of apical transporters, and thus the main area where reabsorption of water, nutrients, and minerals occurs (Zhuo and Li, 2013). Accordingly, this is where most microvilli-containing cells are found, packed into a brush border facing a central lumen (**Fig. 1-4B**) (Rice et al., 2013). There are also predictions that kidney

microvilli have a mechanosensory function in which fluid flow through the lumen can influence their structure and function, such as sodium absorption (Birdsall and Hammond, 2021; Du et al., 2004). Like the small intestine, kidney microvilli also increase functional surface area, by an estimated 36-fold (Welling and Welling, 1975).

Epithelial Cell Culture Models

As noted above, transporting epithelia rely on a brush border of apical microvilli to amplify membrane surface area available for transport, offering fascinating model systems for understanding functional epithelium design and higher-order actin networks (**Fig. 1-4**). Fortunately, well-described cell culture models exist that recapitulate these polarized tissues *in vitro*, providing systems to study the process and importance of brush border assembly.

The porcine proximal kidney tubule LLC-PK1 cell line was first widely used as a model for renal physiology and nephrotoxicity studies (Nielsen et al., 1998; Nielsen et al., 2001; Steinmassl et al., 1995). But even the earliest work with these cells recognized their ability to form apical microvilli and junctional complexes in a confluent monolayer (Hull et al., 1976; Perantoni and Berman, 1979). Since then, LLC-PK1 cells have undergone clonal selection and expansion, yielding clone 4 (CL4). At that time, CL4 cells were acknowledged as a more morphologically homogenous population than their parental line with more apical solute transporters (Amsler and Cook, 1985). However, in more recent years CL4 cells have become a robust model in our laboratory for observing the process of microvilli growth and brush border formation on different time scales (Gaeta et al., 2021a; Gaeta et al., 2021b; Meenderink et al., 2019). When sparsely plated, CL4 cells contain few microvilli followed by growth and then higher-order clustering until

the apical surface has formed what resembles a brush border within a few days post-confluency (DPC) (**Fig. 1-4C**).

Originally derived from a human colorectal adenocarcinoma patient, the CACO-2 cell line is a popular intestinal cell culture model for modeling the brush border and barrier function (Hidalgo et al., 1989). This parental cell line creates a brush border at time points up to 21 DPC, however, the heterogeneity of the cells made them less reliable for brush border assembly and structure studies (Jumarie and Malo, 1991; Lea, 2015; Rousset, 1986). Recognizing this flaw, Peterson and Mooseker isolated the CACO-2_{BBE} clonal line with enhanced "Brush Border Expression" to create a more uniform model for future studies focused on intestinal differentiation (**Fig. 1-4F**) (Peterson and Mooseker, 1992; Peterson and Mooseker, 1993).

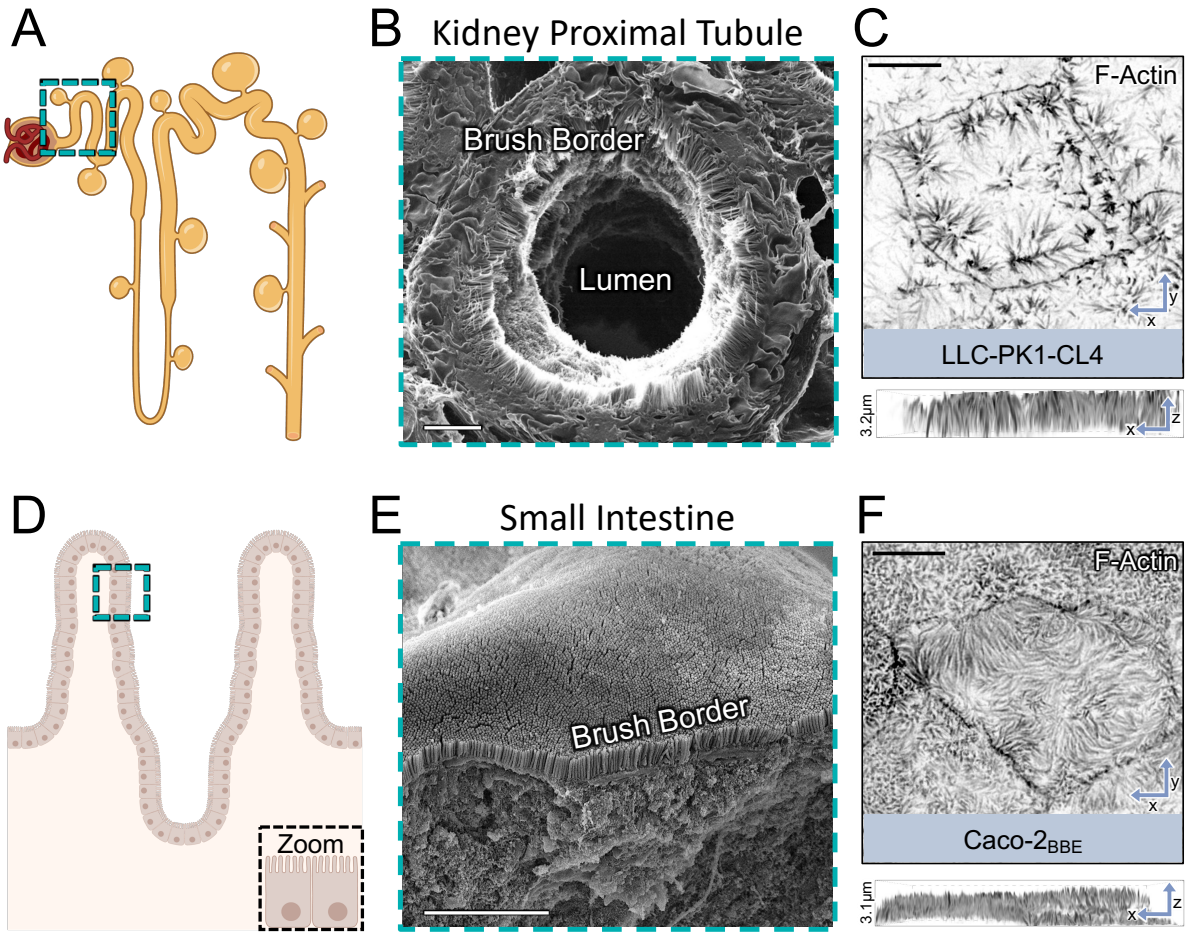

Figure 1-4. Transporting epithelial tissues and models. (**A**) Cartoon of the kidney nephron, with the dashed box highlighting the proximal tubule. (**B**) Helium ion scanning micrograph of the rat proximal tubule. Brush border microvilli protrude into the central lumen. Adapted from (Rice et al., 2013); Creative Commons Attribution License. (**C**) Structured illumination microscope (SIM) image of CL4 porcine proximal tubule cells grown to 3 DPC and stained for F-actin. (**D**) Cartoon of small intestine. The dashed box highlights the cells shown in the zoom that represent absorptive enterocytes. (**E**) Scanning electron micrograph (SEM) of mouse small intestinal brush border. (**F**) SIM image of CACO-2_{BBE} human colon cells grown to 12 DPC and stained for F-actin. All scale bars represent 5 μm.

Brush Border Assembly and Organization

Distal Tip Complex:

The microvillus core consists of 20-40 bundled parallel actin filaments with their barbed ends oriented towards the apical surface (Mooseker and Tilney, 1975; Ohta et al., 2012). This orientation is key in that the fast-growing end of the actin filaments can utilize polymerization to generate force and deform the cell membrane (Gov, 2006). There is growing evidence, however, that myosins coupled to the actin bundle, such as myosin-10 in filopodia, are also integral to generating force to push on the membrane and form protrusions including microvilli (Fitz et al., 2023; Houdusse and Titus, 2021). Another essential piece to microvillus initiation is the "tip complex." First discovered with TEM as an electron dense matrix at the distal ends of microvilli, it was proposed that the proteins residing in this area could play a part in the nucleation of actin filaments required to generate actin-based protrusions (Mooseker and Tilney, 1975; Tilney and Cardell, 1970). Indeed, this tip complex observed in microvilli, filopodia, and stereocilia contains proteins necessary for their growth and maintenance, including EPS8 and IRTKS in microvilli, described in detail below (**Fig. 1-5A-A'**) (Kachar et al., 2000; Svitkina et al., 2003).

EPS8: Classically defined as an actin capping and bundling protein by *in vitro* protein purification and genetic perturbation studies, epidermal growth factor pathway substrate 8 (EPS8) is integral

to the initiation and persistence of microvilli (Disanza et al., 2004; Gaeta et al., 2021a; Hertzog et al., 2010; Postema et al., 2018). The striking localization of EPS8 to microvilli tips also makes it a useful fiducial marker for actin protrusions in cells, labeling the distal ends in distinct puncta (Gaeta et al., 2021a; Manor et al., 2011). Notably, the capping of actin barbed ends is an established mechanism for controlling the growth of actin filaments, which in turn regulates the formation and motility of protrusions (Pantaloni et al., 2001). Mutations to the C-terminal actin binding domain of EPS8 predicted to impact capping and bundling functions are still able to localize to the filament barbed ends, however, the growth rate of new microvilli is significantly slower in the capping mutant. Interestingly, if a microvillus loses EPS8 from its tip, the actin bundle collapses, suggesting that tip-enriched proteins are vital for microvillar maintenance (Gaeta et al., 2021a). Additionally, innovative techniques to identify proximal interacting partners of proteins such as EPS8 have opened the door to discovering new microvillar proteins important for protrusion growth initiation. One example is KIAA1671, a previously uncharacterized protein that also localizes to puncta with EPS8 at the start of actin-bundle formation, but exclusively moves to the base of the growing microvillus where it ultimately resides (Gaeta and Tyska, 2023).

IRTKS: The distinct outward, negative membrane curvature of actin-based protrusions is coordinated by Inverse-Bin/Amphiphysin/RVS (I-BAR) domain containing proteins including IRSp53, MIM, and IRTKS (Ahmed et al., 2010; Zhao et al., 2011). This curvature is regulated by dimerization into a crescent shape that deforms and bends the membrane (Nepal et al., 2021; Rao and Haucke, 2011). As the only identified I-BAR protein in microvilli, insulin receptor tyrosine kinase (IRTKS, also known as BAIAP2L1) was originally implicated in insulin signaling and glucose homeostasis (Huang et al., 2013; McConnell et al., 2011). However, studies in our laboratory demonstrated that IRTKS is also crucial for the elongation of microvilli via two

mechanisms. The first requires a C-terminal WASP homology 2 (WH2) domain that binds actin and mediates crosstalk between the membrane and microvillus core actin bundle (Paunola et al., 2002; Postema et al., 2018). In the second mechanism, IRTKS recruits EPS8 via a src Homology 3 (SH3) protein-protein interaction domain, to further drive microvilli elongation (Kurochkina and Guha, 2013). As a result, IRTKS and EPS8 are some of the first proteins to appear at the initiation of microvillus growth (Gaeta et al., 2021a).

Parallel Actin Bundling Proteins:

To bundle numerous actin filaments together and generate enough force to deform membranes, protrusions rely on actin bundling proteins (**Fig. 1-5A**). In microvilli, the core actin bundlers were originally identified as villin, fimbrin, and espin (Bartles et al., 1998; Bretscher and Weber, 1979; Bretscher and Weber, 1980; Mooseker et al., 1980). Surprisingly, a triple knockout (KO) mouse for all three bundling proteins still formed brush borders, though microvilli length was reduced by 40%, suggesting that additional bundlers may compensate for their loss (Revenu et al., 2012). Indeed, our laboratory discovered a fourth actin bundler, situated at the base – or rootlets – of microvilli, called mitotic spindle positioning (MISP) (Morales et al., 2022). While villin and espin localize primarily to the upper membrane-wrapped portion of the microvillus, fimbrin spans the entire length of the core actin bundle, favoring the rootlet region (Grimm-Gunter et al., 2009). Early *in vivo* studies on these proteins found that villin and fimbrin localize with actin at the surface of immature enterocytes prior to microvillus growth (Heintzelman and Mooseker, 1990). Espin also has roles in the initiation of microvilli and is present at the earliest stages of protrusion emergence from the cell membrane (Gaeta et al., 2021a; Loomis et al., 2003).

Membrane-Actin Linkers:

The crosslinking of bundled actin filaments to the overlying plasma membrane is facilitated by membrane to cytoskeletal crosslinking proteins including myosin 1-a, myosin-6, and ezrin (**Fig. 1-5B**). Not only do these linkers support the microvillus core bundle, but they also prevent neighboring protrusions within the densely packed brush border from coalescing due to membrane surface tension (Atilgan et al., 2006; Crawley et al., 2014a).

Myosin-1a: Myosin-1a is a single-headed motor that localizes within the lateral bridges along the length of the core actin bundle viewed in early microvilli TEM images (Mooseker and Tilney, 1975). Its tail homology 1 (TH1) domain contains two membrane-binding motifs that are essential for keeping myosin-1a near the membrane (Mazerik et al., 2014; Mazerik and Tyska, 2012). As a result, myosin-1a KO mice exhibit brush border morphological changes including fused microvilli (Tyska et al., 2005).

Myosin-6: As the only minus-end-directed actin motor, myosin-6 is quite unique. Within the brush border, this attribute causes it to localize to the base, or terminal web region of microvilli. Like myosin-1a, myosin-6 KO mice also exhibit microvillar fusion in addition to plasma membrane lifting (Hegan et al., 2012). While the lack of a membrane-binding domain made myosin-6's mode of crosslinking a longstanding question, recent work now suggests that it remodels lipid membranes into favorable "saddle-shaped" geometries creating a curvature-dependent interaction (Rogez et al., 2019).

Ezrin: Ezrin is the only ERM (ezrin, radixin, moesin) protein family member expressed in the intestine and plays a versatile role by binding to membrane lipids, F-actin, and transmembrane scaffolding proteins (**Fig. 1-5B-B'**) (Algrain et al., 1993). Interactions between its own N-terminal

and C-terminal domains cause ezrin to exist in a closed, inactive state, preventing it from binding to actin or its transmembrane partners (Gary and Bretscher, 1995). This head to tail folding is regulated by lipid binding and subsequent phosphorylation in which ezrin first localizes to the membrane by binding phosphatidylinositol 4,5-bisphosphate ($PI(4,5)P_2$) via an N terminal FERM domain, followed by phosphorylation of a conserved threonine residue in ezrin's C terminal C-ERMAD domain (T567) (Fievet et al., 2004; Niggli et al., 1995). This in turn brings ezrin into its open, active state, allowing it to interact fully with F-actin and its transmembrane counterparts. Overall, with this controlled activation mechanism ezrin can regulate different stages of brush border differentiation. For example, ezrin appears alongside espin at the earliest steps of protrusion growth soon after IRTKS and EPS8 mark the site of growth. Furthermore, loss of ezrin signal from a microvillus bundle leads to its collapse (Gaeta et al., 2021a).

The Intermicrovillar Adhesion Complex:

The packed array of brush border microvilli was first observed in the 1950s with electron microscopy of thin small intestine sections. The microvilli were so densely packed, in fact that it was difficult to resolve individual processes apart from in the thinnest cut sections of ~0.05 μm (Granger and Baker, 1950). Modern microscopy techniques, including *en face* freeze etch SEM, have since revealed that neighboring microvilli within the brush border are uniformly connected via intermicrovillar links with an average distance of ~50 nm (Crawley et al., 2014b). In depth studies of these links have uncovered an intermicrovillar adhesion complex (IMAC) containing the proteins CDHR2, CDHR5, ANKS4B, USH1C, CALML4, and myosin-7b, (**Fig. 1-5C-C'**) each described in more detail below (Choi et al., 2020; Crawley et al., 2014b; Crawley et al., 2016; Li et al., 2017; Weck et al., 2016). Fascinatingly, a similar adhesion-based complex exists within the inner ear, bridging stereocilia protrusions to control mechanotransduction and hearing (Pan and

Zhang, 2012; Sakaguchi et al., 2009). These parallels demonstrate the importance of such scaffolding protein complexes across multiple organ systems that carry out different functions, making them a relevant topic of study.

CDHR2 and CDHR5: The adhesive nature of the IMAC comes from complexes made up of the protocadherins CDHR2 and CDHR5 (Crawley et al., 2014b). Specific attributes of their adhesion will be discussed in depth in the next section. In brief, these proteins insert into the membrane surrounding each microvillus with a single pass transmembrane domain and extend extracellular domains of varying lengths to physically link neighboring microvilli. This trans-heterophilic complex is dependent on calcium and plays a vital role in maintaining brush border organization and packing (Cencer et al., 2023; Pinette et al., 2019). CDHR2 and CDHR5 also employ C-terminal PDZ-binding motifs to interact with their IMAC counterparts. Notably, there are two major splice isoforms of CDHR5 within microvilli, a long and short (Crawley et al., 2014b; Goldberg et al., 2000; Moulton et al., 2004). A recent preprint study identified isoform-specific localizations, with short-CDHR5 targeting specifically to microvilli tips and long-CDHR5 appearing more distributed along the entire microvillus and in subapical puncta. This study proposed that the larger isoform is less efficient at getting to distal tips due to its added mucin-like domain (Matoo et al., 2023). Studies like these provide evidence that there is still much to be discovered about these IMAC members.

USH1C: First linked to the hearing and vision loss disease type one Usher syndrome, Usher syndrome type-1C, (USH1C, a.k.a. harmonin) has also been localized to the brush border (Crawley et al., 2014b; Verpy et al., 2000). Normally, USH1C serves as a scaffolding protein in the inner ear hair cell tip-link complex, connecting cadherin CDH23 to USH1G (a.k.a. Sans) to the myosin-7a motor protein (Grati and Kachar, 2011). Point and frameshift mutations in USH1C have been

implicated in Usher syndrome and most likely impact its ability to tie the stereocilia tip link complex together (Whatley et al., 2020). Interestingly, Usher syndrome patients may also experience intestinal disease in addition to deaf blindness (Bitner-Glindzicz et al., 2000). Our laboratory later discovered that USH1C was in fact a part of the brush border proteome, and an integral member of the IMAC contributing to tip targeting and brush border assembly (Crawley et al., 2014b; McConnell et al., 2011). Specifically, interruption of binding between USH1C's three PSD-95/discs large/ZO-1 (PDZ) domains and the C-terminal PDZ ligand of CDHR2 or CDHR5 prevents microvillar clustering in CACO-2_{BBE} cells. Furthermore, deletion of USH1C in a KO mouse model also disrupts brush border formation in vivo, with a loss of myosin-7b tip targeting (Crawley et al., 2014b).

ANKS4B: Ankyrin repeat and sterile alpha motif domain containing 4B (ANKS4B) was identified in the brush border proteomic screen and verified to localize to microvilli tips in intestinal and kidney tissues and cell lines (Crawley et al., 2016; McConnell et al., 2011). Apical targeting is controlled in part by a N-terminal ankyrin repeat domain, though the precise mechanism remains unclear. What is known is that ANKS4B has a C-terminal sterile alpha motif (SAM), central (CEN) region, and a PDZ-binding motif that facilitates its interaction with USH1C. KD of ANKS4B in CACO-2_{BBE} cells results in decreased microvillar clustering and packing and a loss of intermicrovillar links demonstrating its role in IMAC formation and function (Crawley et al., 2016).

Myosin-7b: While the IMAC proteins had been localized by immunofluorescence staining to the tips of brush border microvilli, it was not clear exactly how they were directed to this zone. Myosin-7a had been previously identified to target stereocilia tip-link complexes in the inner ear, offering some insight into the IMAC mechanism (Bement et al., 1994). While myosin-7a is a

stereocilia-specific myosin motor, a homologue of this protein was identified in microvilli named myosin-7b (Chen et al., 2001; Houdusse and Titus, 2021). When labeled in small intestine, myosin-7b signal was enriched at microvilli tips (Chen et al., 2001; Crawley et al., 2014b). Further investigation into myosin-7b revealed that it is responsible for carrying the other IMAC components towards microvilli core actin bundle distal ends (Weck et al., 2016). This barbed-end-directed motion requires the activity of its N-terminal motor domain, a central neck domain of several IQ motifs, and a C-terminal MyTH4-FERM (MF) domain and SH3 tail (Chen et al., 2001). Within myosin-7b's cargo binding tail lies the attachment regions for the other IMAC protein members. The first, more N-terminally localized MF domain binds to ANKS4B and the second MF domain binds to the C-terminals of CDHR2 or CDHR5. This second MF domain also binds to the PDZ domain of USH1C (**Fig. 1-5C'**) (Crawley et al., 2014b; Crawley et al., 2016; Li et al., 2017). Myosin-7b KD in CACO-2_{BBE} cells results in brush border defects including decreased microvillar clustering and aberrant intermicrovillar contacts (i.e., base-base and tip-base). Furthermore, KD also causes a significant loss of IMAC tip enrichment which was observed in cells expressing myosin-7b motor domain mutations (Weck et al., 2016).

CALML4: As the newest classified member of the IMAC, calmodulin-like protein 4 (CALML4) directly binds to myosin-7b, acting as a light chain associating with its central IQ motifs (Choi et al., 2020). Expression levels of CALML4 increase with myosin-7b throughout the course of CACO-2_{BBE} cell brush border differentiation. Furthermore, CALML4 KD CACO-2_{BBE} cells exhibit a lack of microvillar clustering, a phenotype seen in other IMAC protein perturbation studies (Cencer et al., 2023; Crawley et al., 2014b; Crawley et al., 2016; Weck et al., 2016).

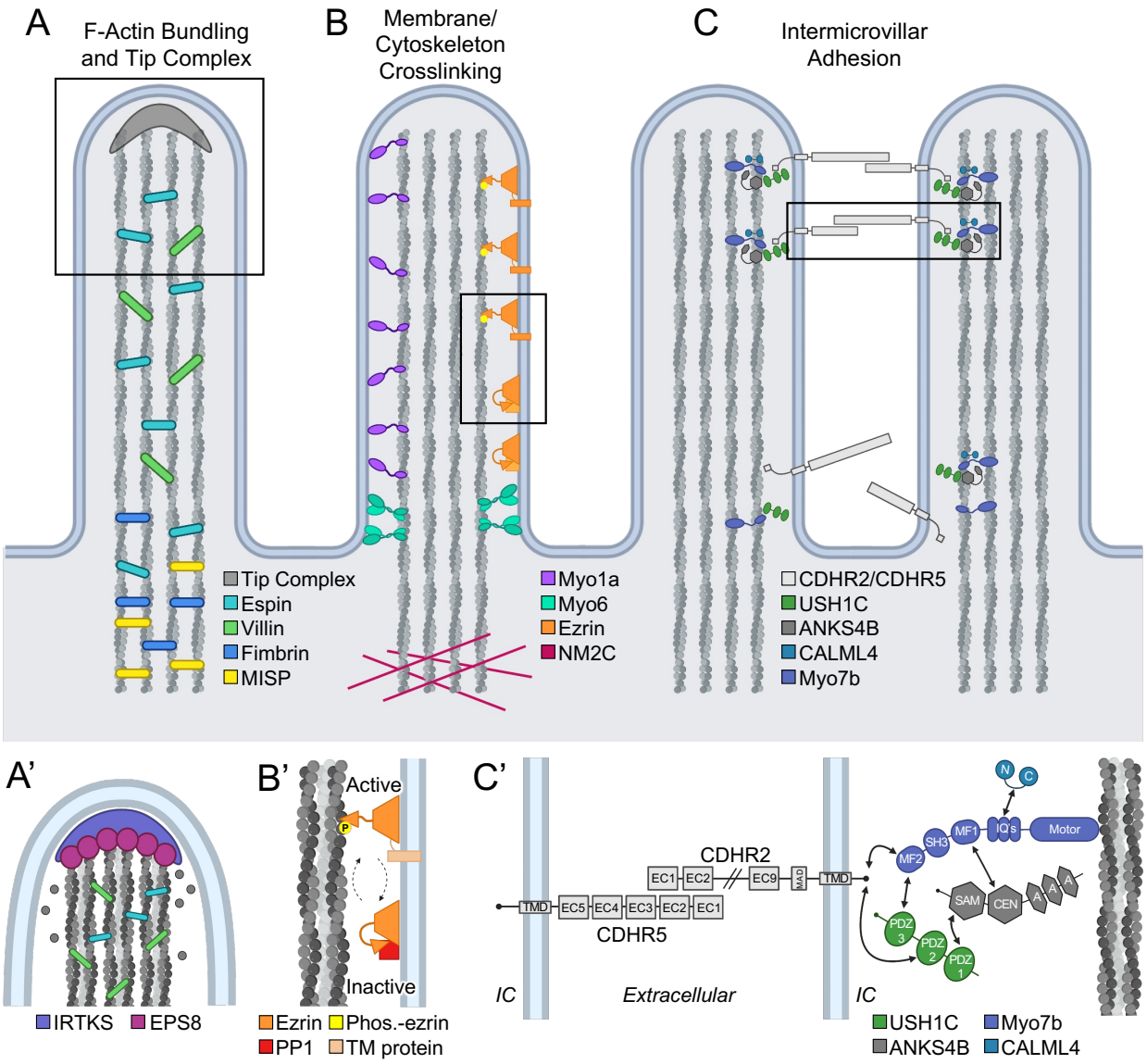

Figure 1-5. Protein-level organization of the intestinal microvillus. (**A**) Actin bunding proteins espin, villin, fimbrin, and MISP are responsible for holding the actin core together. (**A'**) An electron dense "tip complex" composed of I-BAR protein IRTKS and the actin-binding protein EPS8 exists at microvilli tips. (**B-B'**) Proteins linking the membrane encapsulating each microvillus to the F-actin core bundle include myo1a, myo6, and active, phosphorylated ezrin. Ezrin can be inactivated, by proteins such as phosphatase 1 (PP1). Additionally, NM2C anchors F-actin of the core bundle in the terminal web. (**C-C'**) The IMAC links neighboring microvilli together to ensure brush border packing. A protein complex consisting of protocadherins CDHR2 and CDHR5, ANKS4B, and USH1C are trafficked to the microvillus tip via myosin-7b (Myo7b). IC notation represents "intracellular" space.

Cadherin Adhesion Complexes

Cadherins were discovered serendipitously by postdoctoral researcher Masatoshi Takeichi upon using a different trypsin solution in his new laboratory. Cells which used to re-aggregate in suspension culture after trypsinization in his doctoral laboratory now seemed to have permanently disrupted cell-cell adhesion. The culprit was the addition of EDTA, a chelating agent with a proclivity for binding to and sequestering calcium (Ca^{2+}) ions. Downstream studies from this initial observation led to the discovery of a new branch of Ca^{2+}-dependent adhesion molecules, named cadherins (Takeichi, 1977; Takeichi, 2018). The first identified cadherins were designated according to the tissues in which they were found: E-cadherin (epithelial), N-cadherin (neural), and P-cadherin (placental) – CDH1, CDH2, and CDH3, respectfully. In the present day, hundreds of cadherin proteins now make up a large family of cell-cell adhesion molecules with roles in a range of cellular processes including embryo development, tissue morphogenesis, mechanotransduction, tumor suppression, and signaling (Gumbiner, 2005; Halbleib and Nelson, 2006; Kaszak et al., 2020; Klezovitch and Vasioukhin, 2015). Despite their wide range of localizations and diverse roles, cadherins share some common features. Broadly, each protein contains some N-terminal stretch of extracellular cadherin (EC) repeat domains, transmembrane domain(s), and a cytoplasmic domain (Pokutta and Weis, 2007; Shapiro et al., 1995). However, classification of the cadherin superfamily has been difficult due to the high degree of variation in each of these regions (Pouliot, 1992).

Groupings are based on a combination of EC repeat number and cytoplasmic domain homology, which initially separated cadherins into three main groups: classical, desmosomal, and protocadherins. However, as more cadherins were discovered this prompted the formation of subgroups: type I and type II classical cadherins, desmocollin and desmoglein desmosomal

cadherins, α, β, and ɣ-type clustered protocadherins, and non-clustered protocadherins (Sotomayor et al., 2014). In general, classical cadherins, such as CDH1, CDH2, and CDH3, contain 5 EC repeats and can bind catenins with their cytoplasmic domains, often at cell-cell junctions (Oda and Takeichi, 2011; Takeichi, 1995). Desmosomal cadherins also have 5 EC repeats, but are designed to anchor intermediate filaments at desmosomes, per their nomenclature (Saito et al., 2012). Protocadherins have any number of EC repeats and distinct cytoplasmic domains. While the clustered protocadherins all have 6 EC repeats in their extracellular domain, the non-clustered protocadherins exhibit upwards of 34 EC repeats and signature protein binding sequences in their cytoplasmic domains such as PDZ domain binding motifs (Kim et al., 2011; Wolverton and Lalande, 2001). The brush border protocadherins CDHR2 and CDHR5 as well as the stereocilia protocadherins CDH23 and PCDH15 are examples of non-clustered protocadherins (**Fig. 1-6**) (Crawley et al., 2014b; Kazmierczak et al., 2007).

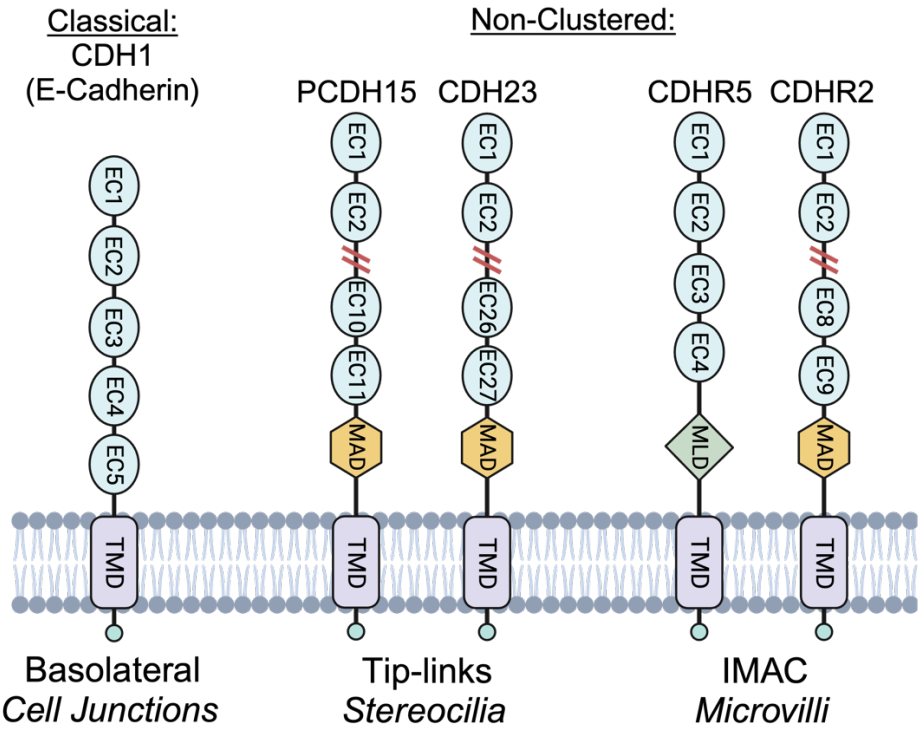

Figure 1-6. Classification of the cadherin superfamily. Cadherins are grouped into subfamilies corresponding to their N-terminal extracellular cadherin (EC) repeat domains and cytoplasmic domain sequences. Non-clustered protocadherin pairs include PCDH15 and CDHR23 in stereocilia tip-links as well as CDHDR5 and CDHR2 in the brush border IMAC that connects neighboring microvilli. TMD = transmembrane domain; MAD = membrane adjacent domain; MLD = mucin-like domain.

Extracellular Cadherin Domains:

EC repeats are the elements that give cadherins their adhesive function. Consisting of ~110 amino acids with a diameter of ~4.5 nm, EC repeats are strung together to create stretches of extracellular domains. The size of this region can vary, with the largest cadherins containing upwards of 34 EC repeats (Sotomayor et al., 2014). Structurally, an EC repeat resembles a "Greek key" with a β-barrel containing seven antiparallel β-strands (**Fig. 1-7A**) (Gray et al., 2021; Hutchinson and Thornton, 1993). Importantly, three Ca^{2+} binding sites exist at the interface between conjoining EC repeats, which explains the calcium-dependent adhesion first observed by Takeichi in his postdoctoral research. This dependence has been shown in multiple contexts, including within the brush border IMAC. In this case, CDHR2 and CDHR5 fail to make intermicrovillar links in CACO-2_{BBE} cells treated with BAPTA – a highly specific calcium chelator (**Fig. 1-7B, arrows**) (Collatz et al., 1997; Crawley et al., 2014b). The same phenomenon has been observed in stereocilia cadherin-based tip links, where BAPTA treatment leads to disrupted tips and shortened stereocilia (Rzadzinska et al., 2004).

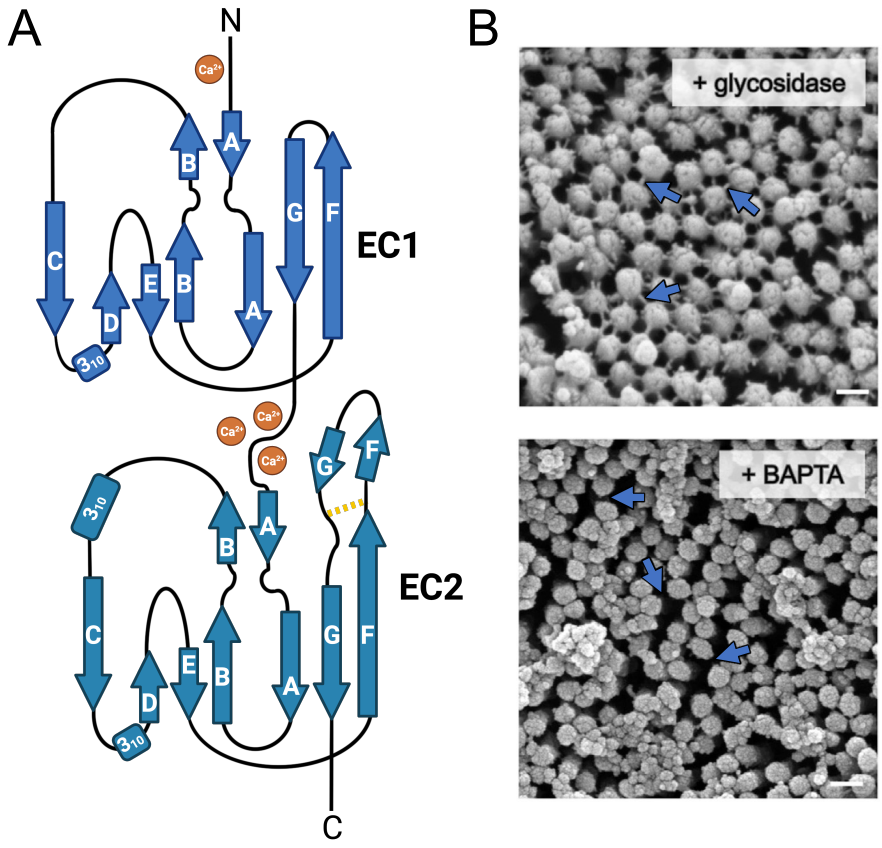

Figure 1-7. Extracellular Cadherin (EC) repeat domains are dependent on calcium for binding. (**A**) Seven β-strand topology of CDHR2's EC2 and EC2 domains, comparable to all cadherin EC repeat domain structures adapted from (Gray et al., 2021); Creative Commons Attribution License. Three Ca^{2+} ions bind at the joining EC domain interfaces. (**B**) Treatment of 20 DPC CACO-2_{BBE} monolayers with the calcium chelator, BAPTA, but not glycosidase, leads to disruption of the IMAC links (arrows) due to impairment of CDHR2 and CDHR5 Ca^{2+}-dependent binding. Adapted from (Crawley et al., 2014b) with permission from Elsevier; License Number 5667730209431. Scale bars represent 150 nm.

More recent structural studies have provided key information on the binding interface between EC1-EC2 in complexes of CDHR2 and CDHR5 (Gray et al., 2021). Mutation of two tryosine residues (Y67 and Y71) near the center of this interface were identified to have opposite effects on protein bead aggregation, a readout for adhesion complex formation. Interestingly, Y67A strengthened aggregation and Y71A impaired it, suggesting that Y67 may have roles in

tuning the flexibility of the binding interface and Y71 blocks the binding interface (Gray et al., 2021).

Interactions of CDHR2 and CDHR5:

At the time of their discovery in the brush border proteome, CDHR2 and CDHR5 were poorly characterized, but initial staining in CACO-2_{BBE} cells revealed their colocalization within brush border microvilli (McConnell et al., 2011). What remained unknown, however, was exactly how they interacted. As discussed above, classical cadherin proteins, such as E-cadherin, exist within cell-cell junctions and not at the apical surface. Only one other instance of apical cadherin complex binding was known at the time of the brush border proteomic screen, within the inner ear stereocilia tip-links where PCDH15 and CDH23 bind in a *trans* heterophilic manner, bridging adjacent stereocilia (Sakaguchi et al., 2009). Therefore, it was assumed that CDHR2 and CDHR5 also formed a heterophilic adhesion complex, connecting adjacent microvilli. Later biochemical studies, however, provided strong evidence that CDHR2 and CDHR5 could also form homophilic adhesion complexes (Crawley et al., 2014b). To make matters more complicated, additional structural studies found that homophilic adhesion differs among species, with homophilic complexes of CDHR2 forming in humans and complexes of CDHR5 in mouse (**Fig. 1-8**). The exact reason for this difference is not yet clear, but has been predicted to be due to variances in gut microbiomes putting evolutionary pressure on IMAC composition (Gray et al., 2021). What is apparent, however, is that having heterophilic or homophilic complexes could provide flexibility in the developing brush border based on differences in IMAC linkage lengths. The calculated total lengths of 36 nm (homophilic CDHR5) to 90 nm (homophilic CDHR2) fall within reported measurements in mouse intestine and CACO-2_{BBE} cells (~20-80 nm) (**Fig. 1-8 A-C**) (Crawley et al., 2014b). Growing evidence also suggests that heterophilic adhesion is stronger than homophilic

adhesion, potentially playing specific roles in microvilli organization during development (Cencer et al., 2023; Crawley et al., 2014b).

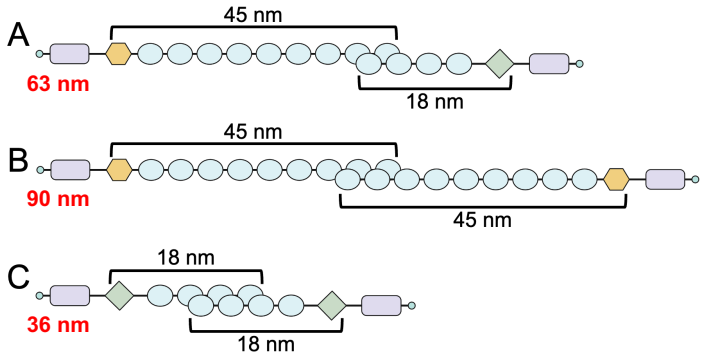

D

Minimal Adhesive Units

Interaction	*H. sapiens*	*M. musculus*
CDHR2/ CDHR5	EC1:EC1	EC1-2:EC1-2
CDHR2/ CDHR2	EC1:EC1	
CDHR5/ CDHR5		EC1-3:EC1-3

Figure 1-8. Species-dependent heterophilic and homophilic binding of CDHR2 and CDHR5. (**A**) Heterophilic binding of CDHR2/CDHR5 is predicted to span 63 nm (4.5 nm per EC domain), (**B**) homophilic CDHR2 complexes could span 90 nm, and (**C**) homophilic CDHR5 36 nm. **(D)** The minimal EC repeat domains needed to form the relevant complex, summarized from (Gray et al., 2021); Creative Commons Attribution License.

IMAC Perturbation Studies:

As expected from an adhesion complex localized to intermicrovillar links, loss of CDHR2 in a KO intestinal specific mouse model leads to disruption of microvillar packing and organization (**Fig. 1-9**) (Pinette et al., 2019). Interestingly, this also leads to a decrease in the signal of the other IMAC members, CDHR5, USH1C, and myosin-7b, suggesting that the maintenance of the IMAC at the tips of microvilli is in part controlled by adhesion, rather than just myosin-7b transport.

Perhaps the most dramatic effect of broken apical adhesion is the loss of ~1/3 of total surface microvilli (**Fig. 1-9D,F**), most likely due to decreased packing efficiency. The loss of microvillar packing in the CDHR2 KO mouse mirrors what has been seen in CACO-2$_{BBE}$ KD cells (**Fig. 1-9G,H**), where brush border disorganization is clear (Crawley et al., 2014b). Interestingly, brush border disorganization and a dramatic decrease in microvillar clustering is a feature of all IMAC perturbation models. These models include an USH1C KO mouse, CDHR2 or CDHR5 KD CACO cells, myosin-7b KO mouse, ANKS4B KD CACO cells, and CALML4 KD CACO cells (Choi et al., 2020; Crawley et al., 2014b; Crawley et al., 2016; Li et al., 2017; Weck et al., 2016). Again, demonstrating the importance of every member of the tip-targeted complex in brush border assembly and maintenance.

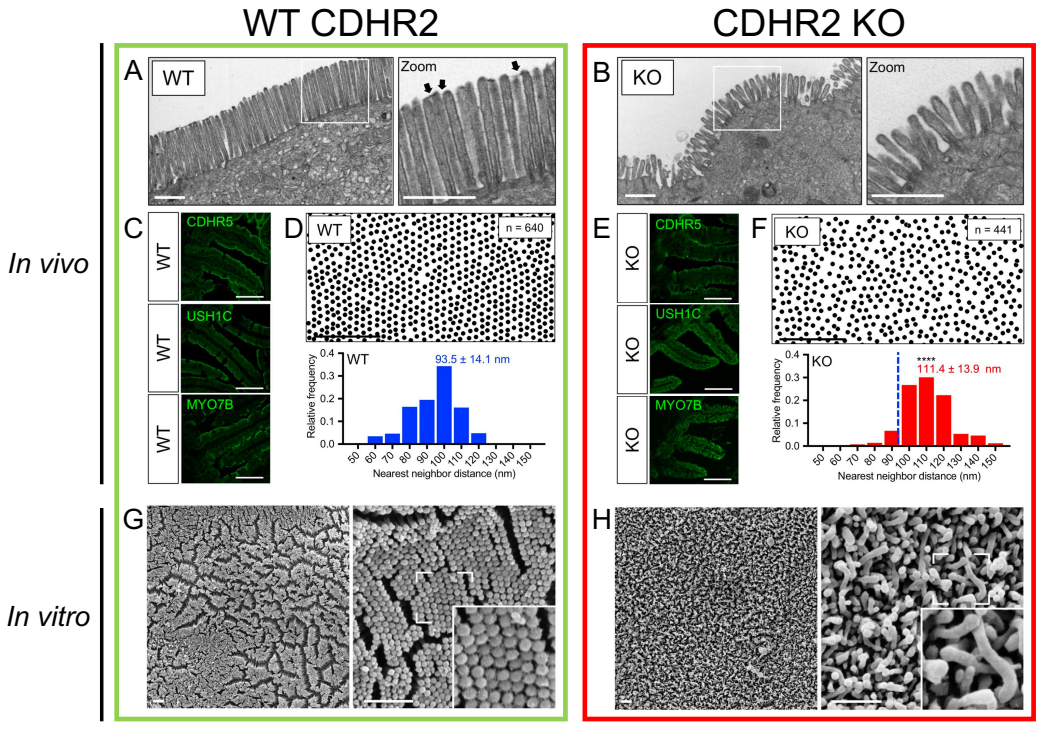

Figure 1-9. Loss of CDHR2 leads to brush border morphology and IMAC defects. (**A**) WT mouse small intestine TEM section showing uniform microvilli, with IMAC links (Zoom, arrows). (**B**) CDHR2 Villin-Cre KO mouse TEM section with splayed microvilli and a loss of tip links (Zoom). Scale bars of A-B represent 500 nm. (**C**) WT mouse staining for CDHR5, USH1C, and MYO7B. Scale bars represent 100 µm. (**D**) Nearest neighbor analysis with a mean distance of 93.5 ± 14.1 nm between neighboring microvilli. (**E**) CDHR5, USH1C, and MYO7B signal is lost from

the brush border in CDHR2 KO mice. Scale bars represent 100 μm. (**F**) KO mice also exhibit an increased distance between neighboring microvilli with a mean of 111.4 ± 13.9 nm, resulting in ~1/3 loss of total microvilli number. Data in A-F adapted from (Pinette et al., 2019); Creative Commons BY-NC-SA 3.0. (**G**) Scramble shRNA CACO-2_{BBE} cells grown to 12 DPC have tightly packed microvilli. (**H**) CDHR2 KD 12 DPC CACO cells have disorganized microvilli, and a loss of tight packing. Scale bars represent 100 μm. Data in G-H adapted from (Crawley et al., 2014b) with permission from Elsevier; License Number 5667730209431.

Junction Barrier Function and Disease

The brush border is often cited as having a dual role in nutrient absorption optimization and prevention of pathogen colonization (Crawley et al., 2014a; Delacour et al., 2016). Despite the common partnership of these two statements, information on how they may be tied together in these roles is lacking. What is well-defined is how the cell-cell junction creates a tight barrier against foreign pathogens, especially important in transporting epithelia that are exposed to the outside environment within the lumen (Paradis et al., 2021). Junctions are classically broken into several parts, making one continuous vertical interface (**Fig. 1-10**). The tight junction lies closest to the apical surface and contains proteins such as junctional adhesion molecule (JAM), occludins, claudins, and zonula occludens (ZO) proteins. Together, the tight junction and its members create a ~ 15 nm gap, that warrants precise passage of molecules into the underlying tissue (Farquhar and Palade, 1963; Vanslembrouck et al., 2022). Underneath the tight junction lies the adherens junction, home to E-cadherin which binds β-catenin. Junction connection to the actin cytoskeleton is mediated by α-catenin, creating the circumferential adhesion belt surrounding each cell (Meng and Takeichi, 2009). Desmosomes are the next junctional component, made up of desmosomal cadherins that bind to intermediate filaments via a cluster of cytoplasmic plaque proteins including desmoplakin (Kowalczyk and Green, 2013). The entire cell-cell junction interface plays a vital role in maintaining a tight barrier in the face of disease (Wei and Huang, 2013).

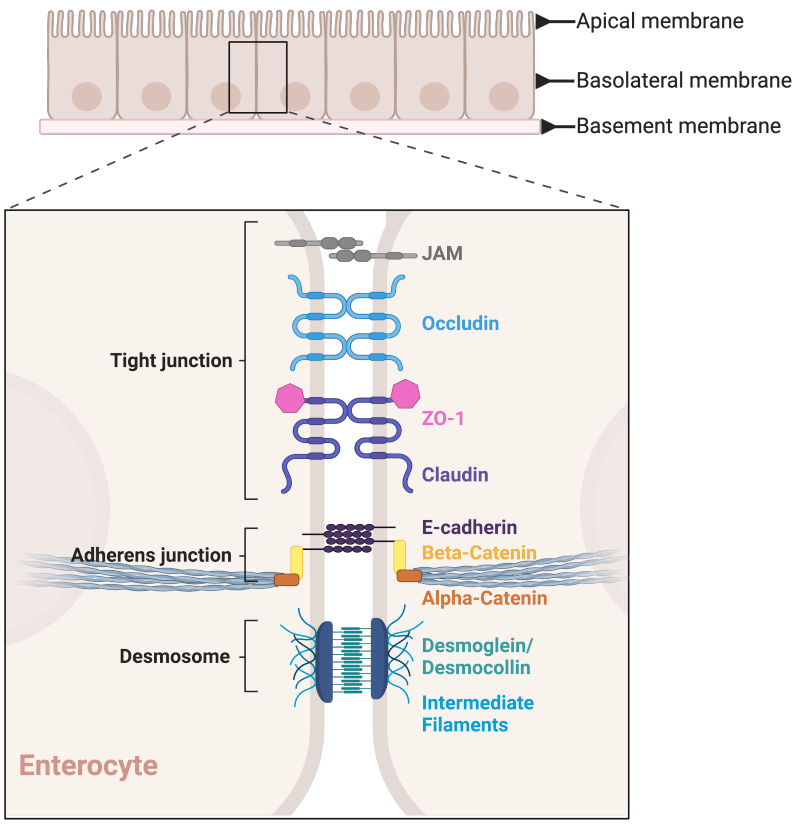

Figure 1-10. Transporting epithelial cells have established junctional contacts.
Tight, adherens, and desmosome junctions and some key proteins of each, as labeled. Figure adapted from BioRender.

Decreased barrier function is a common feature of many intestinal diseases including the inflammatory bowel diseases (IBD) Crohn's and ulcerative colitis (Buning et al., 2012; Hollander et al., 1986; Turpin et al., 2020; Wyatt et al., 1993). As such, expression of the tight junction protein ZO-1 is down-regulated in IBD patients (Kuo et al., 2021). Furthermore, *in vitro* studies of cultured monolayers have shown that increased permeability of junctions is linked to decreased ZO-1 levels (Rodgers et al., 2013; Van Itallie et al., 2009). However, a recent *in vivo* study characterizing the ZO-1 intestinal KO mouse suggests otherwise. In this model, barrier function was not impacted by the loss of ZO-1, rather it imparted misorientation of mitotic spindles in dividing crypt cells, leading to a loss of daughter cells into the intestinal lumen (Kuo et al., 2021).

Interestingly, a recent study analyzing common intestinal protein levels in Crohn's disease patients found that the IMAC proteins are significantly decreased (VanDussen et al., 2018). Accordingly, the question that arises is whether there is a connection between the IMAC and the maintenance of basolateral junctions – discussed in Chapters 4 and 5 of this thesis.

Brush Border Assembly Summary and Unanswered Questions

Microvilli are motile structures, utilizing steady state actin treadmilling for persistent motion (Meenderink et al., 2019). Until the present study outlined in Chapter 3 of this thesis, the only temporal information regarding brush border differentiation occurred at the earliest and later stages of apical maturation (Gaeta et al., 2021a; Meenderink et al., 2019) (**Fig. 1-11**). Nascent cells modeled by sparsely plated CACO-2_{BBE} and CL4 cells in culture give insight into what occurs in transit amplifying cells residing in intestinal crypts. Our laboratory has demonstrated that these early cells contain unstable microvilli that can collapse back into the apical surface upon losing key microvilli core bundling and cross-linking proteins, such as EPS8 and ezrin (**Fig. 1-11A-B**) (Gaeta et al., 2021a). Yet upon exiting the crypt and reaching the villus zone, the mature apical surface is full of a densely packed brush border. This implies that there must be some mechanism in place to stabilize the earliest dynamic protrusions on nascent cells (**Fig. 1-11C-D**). At the tips of microvilli reside the adhesive protocadherin proteins, CDHR2 and CDHR5, primed to perform this very function (Crawley et al., 2014b). Indeed, studies on other cadherins, such as E-cadherin, have shown that they can have stabilizing functions at cell-cell junctions in combination with actin and scaffolding proteins (Cavey et al., 2008). Chapter 3 of this thesis details a mechanism in which strong heterophilic CDHR2/5 adhesion complexes connect microvilli of neighboring cells while spanning junctions. These transjunctional adhesion complexes stabilize microvilli at cell margins and in turn regulate brush border packing (Cencer et al., 2023).

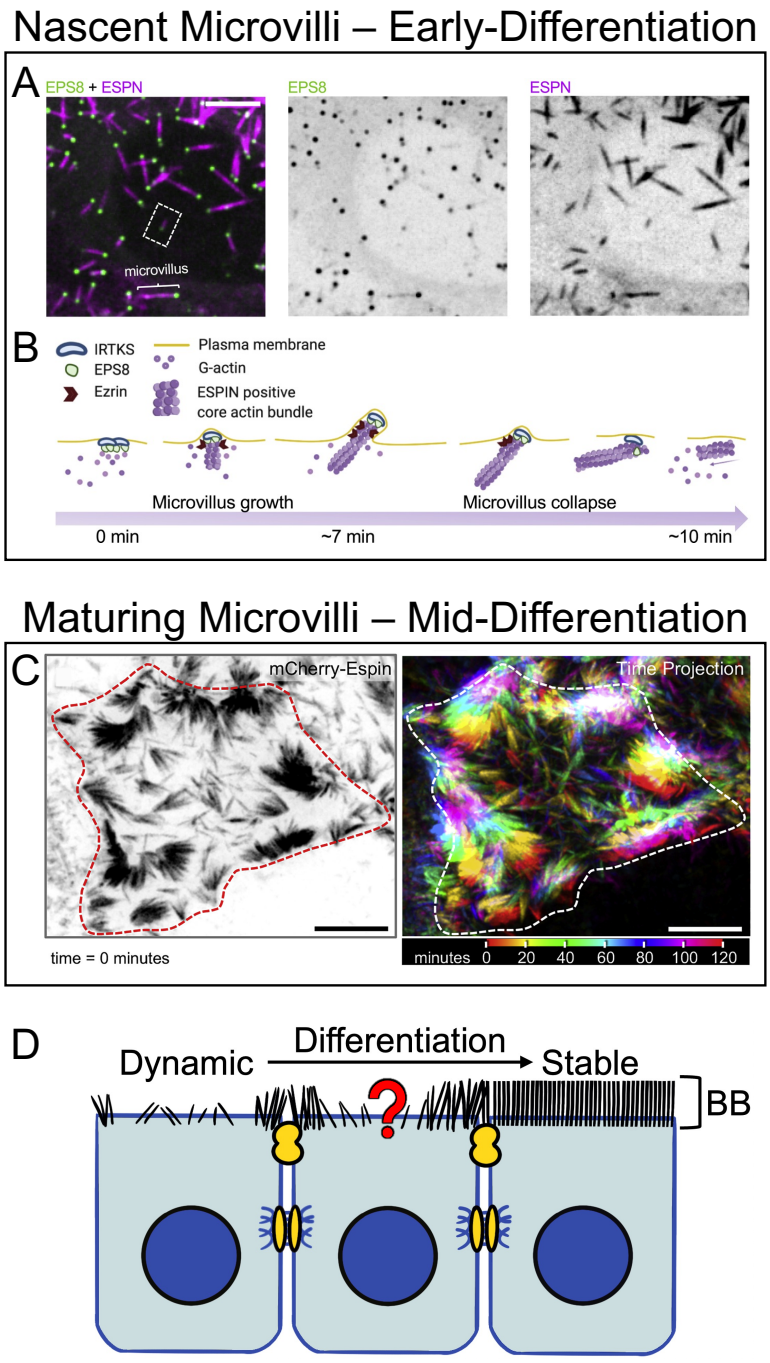

Figure 1-11. Brush border differentiation relies on the stabilization of nascent microvilli, of which the mechanism remains unclear. (**A**) Sub confluent CL4 cells overexpressing EGFP-EPS8 (green) and mCherry-Espin (magenta) in nascent microvilli. (**B**) Model of microvillus growth and collapse in the earliest stage of brush border formation adapted from (Gaeta et al., 2021a); Author Permissions. (**C**) Confluent islands of CL4 cells overexpressing mCherry-Espin at time 0 (left) and over 120 minutes (right, time projection) adapted from (Meenderink et al., 2019); Author Permissions. (**D**) Model for the biological question of how nascent, dynamic microvilli become stabilized over time to form the final brush border structure.

Additionally, the intestinal brush border helps optimize nutrient absorption and blocks colonization from non-commensal pathogens (Delacour et al., 2016). Interestingly, little research has been done to connect how the structure of microvilli and their densely packed nature may influence barrier function. This thesis offers in part a potential mechanism whereby microvilli crossing over the junctions of neighboring epithelial cells linked via transjunctional IMACs may lend an additional level of protection against pathogens that typically gain passage via damaged cell junctions such as *Salmonella* and *E. coli* (Paradis et al., 2021). Chapter 4 of this thesis proposes a mechanism for how apical adhesion complexes that lend stability to differentiating brush border microvilli may also stabilize basolateral junctions, beneath the transjunctional adhesion complex.

CHAPTER II

MATERIALS AND METHODS

Experimental Models

Cell culture models:

LLC-PK1-CL4 (porcine kidney proximal tubule) cells were grown in 1X high glucose DMEM containing 2mM L-glutamine (Corning #10-013-CV) supplemented with 1% L-glutamine (Corning # 25-005-CI) and 10% fetal bovine serum (FBS) (R&D Systems). CACO-2_{BBE} (human colonic adenocarcinoma) cells were grown in the same medium but supplemented with 20% FBS. Cells were maintained in culture incubated at 37°C and 5% CO_2. Cells were tested for mycoplasma monthly using the MycoAlert PLUS Mycoplasma Detection Kit (Lonza #LT07-710) and/or MycoStrip Mycoplasma Dectection Kit (InvivoGen #rep-mys-50).

Animal models:

CDHR2-EGFP mice were created in collaboration with the Vanderbilt Genome Editing Resource. A C57Bl/6N strain containing a *CDHR2* C-terminal EGFP sequence insertion. [crRNA sequence: TGGACACCACAGATCTGTGA] Ribonucleoprotein complexes containing ctRNA and WT SpCas9 protein were targeted to the C-terminus of *CDHR2* were assembled and injected with a single stranded 944 nt DNA donor into 1-cell C57Bl/6N embryos. crRNA, tracrRNA, and WT SpCas9 protein was sourced from Millipore Sigma. The single stranded DNA was produced by Genewiz. Pups were screened for CDHR2-EGFP sequence insertions by PCR and validated by Sanger sequencing (Fig. 3-4). Animal experiments were carried out in accordance with Vanderbilt University Medical Center Institutional Animal Care and Use Committee guidelines under IACUC Protocol ID#: M1600206-02.

Cloning and Constructs

A C-terminally tagged pHALO-N3-CDHR2 (CDHR2-HALO) construct was generated by taking full length CDHR2 via PCR from pEGFP-N3-PCDH24 (CDHR2-EGFP) with the primers CDHR2-Fwd: ATGGCCCAGCTATGGCTG and CDHR2-Rev: CAGGTCCGTGGTGTCCAGG. The product was then TOPO cloned into the pCR8/GW/TOPO vector (Invitrogen #K250020) and then placed into the pHALO-N3 backbone, adapted for Gateway cloning using the Gateway conversion kit (Invitrogen #11828029). All other overexpression constructs listed in this dissertation were previously created and/or reported.

Cell Line Generation

Cells expressing one plasmid were transfected with FuGENE 6 (Promega #E2691) at a FuGENE:DNA (μL:μg) ratio of 3:1 following the reagent protocol in a T25 cell culture flask. The next day, all cells were split up to a T75 flask with the addition of 1mg/mL G418 sulfate for antibiotic selection. Cells were maintained in culture under constant G418 selection to create a stably expressing cell line. Cells co-expressing two plasmids were transiently transfected with Lipofectamine 2000 (Invitrogen #11668019) according to the manufacturer's protocol. The next day, cells were split to plasma-cleaned 35mm glass bottom dishes (CellVis #D35-20-1.5-N) for subsequent imaging. The EGFP-EPS8/mCherry-ESPN CL4 stable cell line was previously created (Gaeta et al., 2021a) by transducing a G418-selected EGFP-EPS8 stable cell line with lentiviral mCherry-ESPN followed by 10 μg/mL puromycin selection. See citation for detailed protocol. The Halo-CDHR2/EGFP-CDHR5 co-expressing CL4 cells were a transient transfection, and not stably selected. mNeon-Green-β-Actin stably expressing CL4 cells were created using the G418 selection method detailed above and sorted with FACS for mid-high expressing cells.

Fluorescence-activated cell sorting (FACS):

Cells were spun down into a pellet and resuspended in "pre-sort medium" containing Phenol free 1X DMEM (Gibco #21063-029) plus 5% FBS, and 1% L-glutamine. Cells were sorted by Vanderbilt University Medical Center's Flow Cytometry Shared Resource on a 5-Laser FACS Aria III system with a 100 μm sized nozzle. All fluorescent positive cells were deposited into a single well of a 6-well plate containing "post-sort medium" of 1X DMEM (Corning #10-013-CV) with Phenol red, 10% FBS, 1% L-glutamine, and 10μL/mL anti-anti (Gibco #15240062). 24 hours post-sort, the media was changed to CL4 culture media (as detailed in cell culture methods) and 1 mg/mL G418 was added for maintaining stable plasmid overexpression. Sorted cell lines were maintained in this media and under antibiotic selection.

CRISPR

CRISPR CDHR2 knockout line generation:

CL4 Cells: Guide RNA's targeting the porcine CDHR2 genetic locus were designed using the CRISPR Guide Benchling tool for single guides 20 bp in length with a NGG PAM within exon 4 of CDHR2. Two guides were selected based on the highest on-target scores provided by Benchling and assembled *in silico* into the lentiCRISPR v2 plasmid (Addgene #52961). Oligo sequences including overhangs for cloning (see Feng Zhang cloning protocol via Addgene) were exported and synthesized by Sigma-Aldrich via Vanderbilt's DNA Core. Oligos were resuspended to 100 μM in molecular grade water. Cloning was performed following the lentiCRISPR v2 cloning protocol (Addgene, Feng Zhang). In brief, the plasmid was digested with BsmBI-v2 (NEB #R0739) and gel purified (Macherey-Nagel #740609.50). Phosphorylated and annealed gRNA oligos were ligated into the purified digested plasmid and the product was transformed into NEB

Stable competent *E. coli* (NEB #C3040H). Bacterial clones were grown on carbenicillin agar plates, isolated, DNA purified, and sequenced using a U6 universal sequencing primer to validate correct gRNA insertion. CRISPR virus was harvested from HEK293FT cells as previously described (Gaeta et al., 2021b). Wildtype CL4 cells were transduced at 70% confluence in a 6-well plate with either gRNA 4(1), gRNA 4(2), or Control (no gRNA) lentiCRISPRv2 virus plus 10 μg/mL Polybrene and placed under 10 μg/mL puromycin selection 48 hours post-transduction. Cells were maintained for 3 weeks under puromycin selection alongside a non-transduced population of WT CL4 cells with puromycin as a marker for 100% cell death.

CACO-2$_{BBE}$ cells: The same general protocol was followed for generating CDHR2 KO CACO cell populations, except gRNA's were designed against the human CDHR2 sequence targeting exon 3 and exon 4 and selected with puromycin as detailed above.

CRISPR clone screening:

After puromycin selection, the heterogenous KO populations were seeded into a 24 well plate at a density of ≤ 1 cell per well. Once single cells had grown into small islands, one per well representing individual clonal populations, they were trypsinized and expanded for screening via antibody staining and DNA sequencing.

DNA Extraction:

Clonal "KO" populations were seeded in 6-well plates, 2 wells per clone, and grown to 100% confluence. Prior to DNA extraction, cells were rinsed in cold 1X DPBS (Corning Cat# 21-031-CV). A mixture of 484 μL Nuclei Lysis Solution (Promega Cat# A795A), 116 μL 0.5M EDTA (Corning Cat# 46-034-Cl), and 10 μL (20 mg/mL) Proteinase K (Sigma Cat# P4850) was added to the cells on ice, 300 μL per well. Cells were scraped and collected in 2 mL Eppendorf tubes and

incubated for 1 hour in a 55°C water bath. 200 µL Protein Precipitation Solution (Promega Cat# A795A) was added, cells were vortexed for 20 s, and placed on ice for 5 min. After centrifugation for 10 min at 11,000Xg, the supernatant was collected, and 600 µL molecular grade isopropanol (Fisher Scientific Cat# BP2618500) was added and the tube was mixed by inverting. After pelleting by centrifugation for 5 min at 11,000Xg, the pellet was washed in 70% ethanol (Macherey Nagel) and resuspended in 25 µL TE Redissolving Buffer (Macherey Nagel Cat# 740797.1) and DNA concentration was measured on a NanoDrop.

Genomic PCR:

A region of 610bp encompassing exons 4 and 5 of the porcine CDHR2 genomic sequence and two regions of 667bp and 700bp encompassing exon 3 or exon 4, respectively, of the human CDHR2 sequence was generated by PCR following the Q5 High-Fidelity Polymerase (New England Biolabs Cat# M0491L) protocol with a genomic template of 200 ng from the clonal "KO" populations. An initial denaturation step of 3 min (98°C) was important for genomic PCR. The PCR products were run on a 1% agarose gel +EtBr (Bio-Rad Cat# 161-0433) and gel purified (Macherey-Nagel #740609.50). Samples were sent to Genewiz (Azenta Life Sciences) premixed with the same primers used for PCR for sequencing following Genewiz submission guidelines for a purified PCR product. The Synthego ICE CRISPR analysis tool was used to evaluate trace files from the KO clone sequencing results (Conant et al., 2022).

Immunofluorescent Staining

Frozen tissue section preparation:

The proximal segment (duodenum to jejunum) of the mouse intestinal tube was excised and flushed with cold 1X phosphate-buffered saline (PBS). One end of the tube was clamped with a hemostat and the tube was filled with room temperature 2% paraformaldehyde (PFA) (Electron Microscopy Sciences) with a syringe and metal cannula. The other end of the tube was clamped with a hemostat and the tissue was laid in a petri dish containing excess 2% PFA and incubated for 15 minutes at room temperature. Hemostats were removed and the tissue was cut lengthwise into one flat piece. Tissue was then sub dissected into ~2mm^2 pieces and fixed for an additional 30 minutes in a vial of 2% PFA at room temperature. After fixation, the tissue was washed 3 times with PBS and then placed, villi-side down, into a vial of cold 30% sucrose/1% sodium azide. The tissue was placed at 4°C, overnight until sections sank to the bottom of the tube. The next day, sections were passed through 3 separate blocks of optimal cutting temperature (OCT) compound (Electron Microscopy Sciences) to wash off the sucrose solution, oriented with villi parallel to the lab bench in a fresh block of OCT, and snap frozen in dry ice-cooled acetone. Samples were cut into 10 μm thin sections using a Leica CM1950 cryostat and mounted on plasma-cleaned #1.5H precision coverslips (Thorlabs). Coverslips were stored at -20°C until staining.

Frozen section immunofluorescence:

Coverslips were thawed to room temperature and rinsed twice with 1X PBS to remove OCT. Sections were permeabilized with 0.2% Triton X-100 (diluted in PBS) for 10 minutes at room temperature. Sections were then rinsed once with PBS at room temperature and blocked in 10% bovine serum albumin (BSA) for 2 hours at 37°C in a humidified chamber. After rinsing with PBS, primary antibody (diluted in 1% BSA) was applied overnight at 4°C in a humidified chamber. The

next day, sections were rinsed with 1X PBS 4 times and secondary antibody (diluted in 1% BSA) was applied for 2 hours at room temperature in a dark, humidified chamber. Sections were rinsed 4 times with 1X PBS and coverslips were mounted onto glass slides with ProLong Gold. The following antibodies and dilutions were used for EGFP-CDHR2 mouse frozen section staining: anti-GFP (chicken Aves #GFP-1020), 1:200; anti-CDHR5 (rabbit, Sigma #HPA009173), 1:250; anti-ZO-1 clone R40.76 (rat, EMD Millipore Sigma #MABT11), 1:100; Alexa Fluor goat anti-chicken 488 (Invitrogen #A-11039), 1:1000; Alexa Fluor F(ab')2 fragment goat anti-rabbit 568 (Invitrogen #A21069), 1:1000; Alexa Fluor goat anti-rat 647 (Invitrogen #A21247), 1:200; and Alexa Fluor Plus 405 Phalloidin (Invitrogen #A30104), 1:200 for actin staining. The secondary antibodies, not including phalloidin, were spun down for 10 minutes at 4°C and 21 x g prior to using.

Swiss roll and paraffin embedded tissue preparation:

The entire mouse small intestinal tube was excised and flushed with cold 1X PBS. Tissue was fixed in the tube using the hemostat technique described above with room temperature 2% PFA for 15 minutes. After removing the hemostats, the intestinal tube was slid onto a metal cannula and cut lengthwise, down the entire length, with scissors. The flayed tissue was then rolled out, villi side up, onto a strip of parafilm. A hemostat was clamped onto the proximal end (duodenum) of the intestine and rolled up into an intestinal Swiss roll. A 21g needle was placed through the roll and the hemostat was removed. The roll was then placed into 10% neutral buffered formalin at room temperature for 48 hours. After fixation, the needle was removed and the roll was placed, horizontally, into a large tissue cassette and placed back into the formalin. Cassettes were submitted to the Vanderbilt University Translational Pathology Shared Resource to be embedded

in paraffin wax and sliced onto glass slides, at 10 μm thickness. Slides were stored at room temperature until staining.

Paraffin embedded tissue staining:

Using a Tissue-TekII manual slide staining set, slides were deparaffinized in Histo-Clear II (national diagnostics) 2 times, 3 minutes each. Tissue was then rehydrated in a descending ethanol series [100%, 100%, 95%, 90%, 70%, 50%] 5 minutes each followed by washing in PBS 3 times, 3 minutes each. Slides were boiled in antigen retrieval buffer [10mM Tris, 0.5mM EGTA, pH 9.0] in coplin jars for 1 hour using a rice cooker and then cooled to room temperature. Slides were washed 3 times, 3 minutes each in PBS and then blocked in 10% NGS for 1 hour at room temperature. Primary antibody (diluted in 1% NGS) was added overnight at 4°C. The next day, slides were washed 3 times, 5 minutes each in PBS and secondary antibody (diluted in 1% NGS) was added for 1 hour at room temperature in the dark. Slides were then washed 3 times, 5 minutes each in PBS followed by dehydration with an ascending ethanol series [50%, 70%, 90%, 95%, 100%, 100%] 5 minutes each. A coverslip was mounted with ProLong Gold. The following antibodies and dilutions were used for paraffin section staining: anti-ZO-1 (rabbit, Invitrogen #61-7300), 1:50; anti-Villin (mouse, Santa Cruz #SC-66022), 1:50; or anti-Villin (rabbit, Santa Cruz # SC-28283) 1:50; anti-E-cadherin (mouse, BD Biosciences #610182), 1:100; anti-EpCAM (rabbit, Invitrogen #PA5-19832), 1:100; anti-MYH14/NM2C (rabbit, Proteintech #20716-1-AP), 1:100; anti-Claudin-7 (rabbit, Invitrogen #34-9100), 1:100; Alexa Fluor F(ab')2 fragment goat anti-rabbit 488 (Invitrogen #A11070), 1:1000; Alexa Fluor goat anti-mouse 568 (Invitrogen #A11019), 1:1000; Alexa Fluor F(ab')2 fragment goat anti-rabbit 568 (Invitrogen #A21069), 1:1000; Alexa Fluor F(ab')2 fragment goat anti-mouse 488 (Invitrogen #A11017), 1:1000. The secondary

antibodies were spun down for 10 minutes at 4°C and 21 x g prior to using. DRAQ5 was used to label nuclei (Molecular Probes #62251); 1:500.

Fixed cell immunofluorescence:

Prior to fixation and staining, CL4 and CACO-2_{BBE} cells were grown to *n* days post-confluent (DPC) on acid-washed 22x22 mm #1.5H coverslips (Globe Scientific) in a 6-well plate to a time point with apical polarity representative of their native tissue, 3 DPC and 12 DPC, respectively. First, cells were rinsed in warm 1X PBS and fixed in 4% PFA for 15 minutes at 37°C. Cells were then washed three times, 5 minutes each, with 1X PBS and permeabilized with 0.1% Triton X-100 for 10 minutes at room temperature. 5% BSA was added for 1 hour at 37°C as blocking solution. After rinsing with 1X PBS, primary antibody (diluted in 1% BSA) was added for 1 hour at 37°C. Labeling with primary antibody was followed by washing 4 times, 5 minutes each, with 1X PBS. Secondary antibody (diluted in 1% BSA) was then applied for 1 hour at room temperature in the dark. After incubation in secondary antibody, cells were washed 4 times, 5 minutes each with 1X PBS and coverslips were mounted on glass slides with ProLong Gold. The following antibodies and dilutions were used for cell staining: anti-PCLKC (CDHR2) (mouse, Abnova #H00054825-M01), 1:25; anti-CDHR5 (Rabbit, Sigma #HPA009173), 1:250; anti-ZO-1 clone R40.76 in CL4 (rat, EMD Millipore Sigma #MABT11), 1:100; anti-ZO-1 in CACO-2_{BBE} (rabbit, Invitrogen #61-7300), 1:50; anti-E-cadherin (mouse, BD Biosciences #610182), 1:100; anti-EpCAM (rabbit, Invitrogen #PA5-19832), 1:100; anti-MYH14/NM2C (rabbit, Proteintech #20716-1-AP), 1:100; anti-Claudin-7 (rabbit, Invitrogen #34-9100), 1:100; anti-Beta-Catenin (rabbit, Invitrogen #71-2700), 1:100; Alexa Fluor F(ab')2 fragment goat anti-rabbit 488 (Invitrogen #A11070), 1:1000; Alexa Fluor goat anti-mouse 568 (Invitrogen #A11019), 1:1000; Alexa Fluor F(ab')2 fragment

goat anti-mouse 488 (Invitrogen #A11017) and goat anti-rabbit 568 (Invitrogen #A21069), 1:1000; Alexa Fluor goat anti-rat 647 (Invitrogen #A21247), 1:200; and Alexa Fluor Plus 405 Phalloidin (Invitrogen # A30104) or Alexa Fluor 647 Phalloidin (Invitrogen # A22287), 1:200 for actin staining. The secondary antibodies, not including phalloidin, were spun down for 10 minutes at 4°C and 21 x g prior to using.

Cell Mixing Experiments

Fluorescently sorted CL4 cell populations were grown independently and under G418 antibiotic selective pressure to ~80% confluence, trypsinized, and resuspended in CL4 media to a density of ~850,000 cells/mL. 250 µL of each cell population were seeded in plasma-cleaned glass-bottom dishes or onto acid washed coverslips at a density of ~400,000 total cells at a mixing ratio of 1:1 (e.g. CDHR2-EGFP cells were mixed with CDHR5-mCherry cells). A similar mixing method was used for CRISPR Control and CDHR2 KO CL4 cells, at a mixing ration of 1:1. Immediately after seeding, cell populations were thoroughly mixed by pipette. Cells were grown to 3DPC for fixed cell staining or for 1 day for live cell imaging (FRAP).

Microscopy

Fixed sample microscopy:

Laser scanning confocal microscopy was performed on a Nikon A1 microscope equipped with 488 nm, 568 nm, and 647 nm LASERs. Mixed CL4 cell populations for linescan analysis were imaged using a Plan Apo 40x/1.3 NA oil immersion objective. CACO-2_{BBE} cells were imaged using an Apo TIRF 100x/1.49 NA TIRF oil immersion objective. Spinning disk confocal microscopy was used for CRISPR CDHR2 KO cell and CDHR2 KO mouse tissue imaging and intensity analysis using a Nikon Ti2 inverted light microscope with a Yokogawa CSU-W1 spinning disk head, a

Photometrics Prime 95B sCMOS camera, and four excitation LASERs (488, 568, 647, and 405 nm) and a 60X/1.49 NA TIRF oil immersion objective. Structured illumination microscopy (SIM) was used for imaging frozen tissue sections and fixed cells with a Nikon N-SIM equipped with 405, 488, 468, and 647 nm LASERs, an Andor DU-897 EMCCD camera, and a TIRF 100X/1.49 NA TIRF oil immersion objective. All SIM images were reconstructed using Nikon Elements software.

Live imaging microscopy:

Prior to live cell imaging, cells growing in 35mm glass bottom dishes were rinsed once with 1X DPBS (Corning #21-031-CV). FluoroBrite imaging media (Gibco #A18967-01) supplemented with 10% FBS and 1% L-glutamine was added to the dish. For CL4 cells expressing Halo-CDHR2, Janelia Fluor 635 dye (Janelia) was added to the FluoroBrite media at a concentration of 50 nM for 1 hour at 37°C immediately prior to imaging. Spinning disk confocal microscopy was performed using a Nikon Ti2 inverted light microscope with a Yokogawa CSU-X1 spinning disk head, a Photometrics Prime 95B or Hamamatsu Fusion BT sCMOS camera, and three excitation LASERs (488, 568 and 647 nm). A 100X/1.49 NA TIRF oil immersion objective was used for all acquisitions. A stage incubator (Tokai Hit) maintained cells in a humidified environment at 37°C with 5% CO_2.

Electron microscopy – CACO-2$_{BBE}$ and LLC-PK1-CL4 cells and tissue:

To prepare samples, cells were plated on glass coverslips washed once with warm SEM buffer (0.1M HEPES, pH 7.3) supplemented with 2 mM $CaCl_2$, then fixed with 2.5% glutaraldehyde and then 4% paraformaldehyde in SEM buffer supplemented with 2mM $CaCl_2$. Samples were washed in SEM buffer, then incubated in 1% tannic acid, washed with ddH_2O, incubated with 1% OsO4,

washed with ddH_2O, incubated with 1% uranyl acetate, then washed with ddH_2O. Samples were dehydrated in a graded ethanol series. Samples were then dried using critical point drying and mounted on aluminum stubs and coated with gold/palladium using a sputter coater. SEM imaging was performed using Quanta 250 Environmental-SEM operated in high vacuum mode with an accelerating voltage of 5–10 kV or imaged on a Zeiss Crossbeam 550 at 2keV. All reagents were purchased from Electron Microscopy Sciences. For more detailed methods, see (Meenderink et al., 2019). TEM of mouse intestine was performed as previously described (Pinette et al., 2019).

Electron microscopy – crypt-villus axis:

For SEM imaging of intestinal sections, immediately after euthanasia, ~5 mm murine duodenal sections were quickly fixed in a large volume (10 mL) of 2.5% glutaraldehyde and 4% paraformaldehyde in SEM buffer (described above). Sections were then washed in SEM buffer prior to embedding in Tissue-Tek OCT compound (Sakura Finetek #4583). To ensure stable support of the complex architecture within the explant lumens, samples were gently moved through 3 rounds of fresh OCT compound with gentle manipulation to ensure penetration of the OCT. Samples were then placed in cryomolds (with OCT) and frozen over a dry ice/ethanol slurry. Molds were stored at -80C once fully frozen. Frozen explants were subsequently sectioned on a Leica CM1950 crytostat at 50 μm/section and melted onto stainless steel AFM specimen discs (Electron Microscopy Sciences). Next, explant sections and disks were immersed in 1% OsO_4, washed in ddH_2O, then dehydrated through graded ethanol series. Of note, it was most common to experience detachment of the section from the AFM disk during the OsO_4 and dehydration steps. Detached sections were recovered and gently adhered to an aluminum SEM specimen stub via conductive adhesive tab. SEM imaging was performed on a Quanta 250 environmental SEM, as described above.

Fluorescence recovery after photobleaching (FRAP):

A square ROI was drawn in Nikon Elements at marginal and/or medial microvilli regions. A stimulating 405 nm LASER controlled by a Bruker mini-scanner set at 70% power and a dwell time of 40 us was targeted to each ROI after the first 3 frames of the movie acquisition. Two ND time acquisitions were used for imaging fluorescence recovery at intervals of 15 s for 3 minutes, followed by intervals of 30 s for 10 minutes.

Wound Healing:

CL4 cells were seeded at a total of 30,000 cells per well of an Ibidi 2-chamber insert (Ibidi #80209) adhered to a 35 mm plasma cleaned glass-bottom dish. Cells were grown for 2 days or until they had just reached the edge of the chamber. The chamber media was aspirated, and the insert was carefully removed with forceps. Cells were gently rinsed with warm DPBS and fresh media was added to the dish. Cells were left in the incubator overnight, ~12 hours, to recover. Before imaging, cells were rinsed and 1:1000 CellBrite Steady 650 membrane dye and 1:1000 kit enhancer (Biotium #30108) was added in Fluorobrite DMEM +10% FBS for 30 minutes at 37°C. Cells were then imaged using a 10X Plan Apo 0.45 NA objective on a X1 spinning disk confocal microscope equipped with a 647 nm excitation LASER for ~24 hours, or until the wound had fully closed.

CACO-2$_{BBE}$ cells were seeded at a total of 50,000 cells per well of a 24 well plate (Thermo Scientific #142475) and allowed to grow until they just reached 100% monolayer coverage. Each monolayer was scratched with a p10 pipette tip and imaged using a BioTek Cytation 5 plate reader in 1 hour intervals over a total of 20 hours.

Transepithelial Electrical Resistance

Transwells (Greiner Bio-one #662641) were primed with 100 µL of cell culture media in the top chamber and 600 µL in the bottom chamber and left at 37°C for 15 minutes prior to cell seeding. Control and CDHR2 KO clone CACO-2_{BBE} cells were counted, and 30,000 cells were seeded in each transwell with a total volume of 100 µL. A "blank" transwell was also maintained with media only for background TEER measurements. 24 hours post-seeding, the first TEER measurements were taken for the "0 DPC" time point. TEER was measured in ohms (Ω) using an EVOM3 epithelial voltohmeter device (World Precision Instruments) equipped with a calibrated electrode (World Precision Instruments #STX2-PLUS). Prior to each TEER measurement, existing media was exchanged for fresh media, and cells were incubated for 4 hours to ensure equal volume and equilibration in each well. The raw blank TEER value was subtracted from each monolayer TEER value and then multiplied by 0.33 cm^2, the area of the transwell, to obtain the reported TEER value in $\Omega \cdot cm^2$.

Drug Treatment

Blebbistatin:

A 10 mM stock solution was created by dissolving Blebbistatin (Blebb) in DMSO (Sigma Cat# D8418) according to manufacturer's guidelines (Selleck Chemicals Cat# S7099). Stable mCherry-ESPN CL4 cells were seeded on 35 mm glass bottom dishes and grown to 100% confluence. Immediately prior to live imaging, cells were rinsed once with 1X DPBS and 1mL of CL4 growth media was added to the dish. Cells were placed on the spinning disk confocal X1 microscope, described above, and live acquisition was started. After 5 min of baseline imaging, at 30 s intervals, 1mL of CL4 media containing 40 µM Blebb was added to the existing 1mL of media on the

microscope, a final concentration of 20 μM. Control DMSO treatments were similarly performed, using the same volume of DMSO as Blebb in the 1mL of added media. Cells were imaged for a total of 1.5 hr, at 30 s intervals, with Blebb or DMSO.

CACO-2_{BBE} *E. coli* Infection

Prior to infection, CACO cells were grown to 16 DPC on acid washed coverslips. A single colony of KC12+EspFu was grown in LB + antibiotics (kan+amp) in a shaking incubator at 37°C overnight. To pre-activate the bacteria, 250ul of overnight culture (LB+bacteria+antibiotics) was added into 5ml of serum free DMEM + F12 (1:1) and incubated for ~2.5-3 hrs at 37°C in a 5% CO_2 incubator without shaking. The starter culture was vortexed and OD 600 was read (optimal OD for infection 0.3-0.4) with a spectrophotometer. At 16 DPC, cells were washed once in PBS and 50 μL of pre-activated bacteria solution and 1.5-2 mL serum free DMEM + F12 (1:1) was added. Cells were incubated for 1 hour at 37°C and 5% CO_2. Media was changed after the first hour and cells were incubated for an additional 6 hours. Cells were washed once with warm PBS and fixed with 4% PFA for 15 minutes at 37°C. Cells were washed three times with PBS and stored overnight at 4°C for staining the next day.

Quantification And Statistical Analysis

Microvilli orientation measurements:

In Fiji, the first frames of three independent mCherry-ESPN CL4 cell movies were used for orientation measurements shown in Fig. 3-2B. A thin, rectangular ROI (height 12 pixels) was drawn across an entire cell to encompass both marginal and medial areas (sample ROI Fig 3-2A, dotted box). The ROI hyperstack was duplicated and 3D projected with rotation around the X axis. The marginal zone was defined as 10% of the ROI, at either end of the image (overlying cell

junctions) and the medial zone was the remaining central 80% of the ROI. Using the Angle tool, a line was drawn down the length of each microvillus (dotted lines, Fig. 3-2B) with the angle base parallel to the cell surface (solid lines Fig. 3-2B). Angle measurements were plotted in Prism in a column chart and mean marginal and medial angles were compared using a Welch's unpaired t-test.

Temporal color coding:

Time frames for every 3 minutes were selected (18 total frames). Using the Temporal-Color Code function in Fiji, the ESPN channel was coded (start frame 1, end frame 18) using the Spectrum LUT (Fig. 3-3B).

Microvilli tracking using EGFP-EPS8 puncta:

Denoised and deconvolved 3D movies were converted into max intensity projections in the Z plane. Next, a binary via the spot detection tool was applied to the FITC channel (EPS8 signal) with a diameter of 260 nm and a contrast value of 25 to threshold EPS8 puncta representing individual microvilli in the ROI (medial or marginal). Tracking parameters did not allow for the detection of new tracks after the first frame, allowed for a maximum of 3 gaps in a given track, and a standard deviation multiplier of 2. Using the tracking tool, binaries, representing EPS8 puncta, were tracked and any points lying outside of the ROI were deselected. Track data, time and X Y positions, were then exported to Excel and analyzed and plotted in Prism as radial X Y positions over time by subtracting each position in X or Y from the respective point position at time 0, making the first position (0,0). Three independent live cell imaging experiments were used for the analysis.

Mean squared displacement analysis:

Marginal and medial EPS8 puncta trajectories representing microvillar motion were analyzed using mean squared displacement (MSD) analysis as previously described (Meenderink et al., 2019). MSD curves were subsequently fit with two models (Qian et al., 1991; Sheetz et al., 1989): (1) an active motion model in the form $MSD(nDt) = 4Dt + V^2 * nDt^2$, where D is the diffusion coefficient and V is the velocity of active motion, and (2) a constrained diffusion model in the form of $MSD(nDt) = P[1-e^{(-4D*nDt/P)}]$, where P is the plateau of confinement and D is the diffusion coefficient. Non-linear curve fitting was performed using PRISM v.9 and sum-of-squares F-tests were used to select the best model for fitting.

Cell mixing linescans:

Using Fiji, a segmented line with a width of 6 was drawn across mixed cell interfaces to encapsulate signal at the mixed cell (marginal) interfaces. Lines with a minimum length of 20 μm and maximum length of 75 μm were used in analysis. Intensities were normalized from 0 to 1 in Prism with 0 being the lowest gray value in the linescan and 1 being the highest. The residual plots shown were calculated from the respective representative linescan by subtracting mCherry intensity from EGFP intensity at each length in X. 30 individual linescans from each cell mixing scenario were plotted on their own XY correlation plot in Prism. Combined Pearson's r values from the 30 individual correlations were plotted in Fig. 3-7K, and mean r values were compared in Prism using an Ordinary one-way ANOVA with multiple comparisons.

FRAP fraction recovery analysis:

A background ROI and reference ROI were used to account for photobleaching and background fluorescence in both channels. Fraction recovery over time was calculated from

$\frac{(Bleached\ ROI - Background)}{(Reference\ ROI - Background)}$. Recovery curves were fitted with a two-phase association equation in Prism and the immobile fraction was calculated from 1 minus the plateau. Images presented in FRAP figure montages were denoised and deconvolved in Nikon Elements for presentation clarity, however all analyzed measurements presented in the FRAP plots were taken from raw, unprocessed movies.

CDHR2 KO cell intensity measurements:

A total of 45 60X fields were used for each condition, control or KO, from stained coverslips. (For the KO, 15 60X fields were taken for each sequenced clone, for a compiled total of 45 KO fields.) Raw images were maximally projected in Z in FIJI and mean intensity of the entire field was measured for the CDHR2 and CDHR5 channels. The measured intensities were plotted in Prism and statistics were quantified with an unpaired t-test.

ESPN intensity measurements:

Blebbistatin Treatment: Movies from three independent control (DMSO) and blebbistatin treatments were maximally projected in Z in FIJI. Frames at time 0 hr (pre-Blebb or DMSO) and 1.5 hr (post-Blebb or DMSO) were isolated and used for intensity measurements. A segmented line with a width of 40 was drawn along the same cell-cell interfaces at both time points. Paired mean ESPN intensities (16-bit gray value) were plotted in Prism and the mean change in intensity (Δ) from 0 hr to 1.5 hr was quantified. A total of 20 pairs were used from each treatment analysis from 2 independent movies (4 movies total). A paired t-test was used for statistical testing of intensity differences.

24-hour ESPN movies: Movies were maximum intensity projected through Z using FIJI. A segmented line with a width of 40 was drawn along the *entire* intact marginal perimeter of the

same cells at 0 hr and 24 hr to measure mean marginal ESPN intensities. Medial intensities were measured by maximum intensity projected through Z using Nikon Elements. A Bezier ROI was drawn by hand to encompass the central, medial region of the same cells at 0 hr and 24 hr to measure mean medial ESPN intensities. Paired marginal and medial ESPN intensities (16-bit gray values) were plotted in Prism. Three separate live cell movies were used for the quantification as delineated by runs 1, 2, 3 (Fig 3-13D). The mean change in ESPN intensity (Δ) for each region from each movie at 0 hr and 24 hr were also potted (Fig. 3-13E) and subject to unpaired t-testing in Prism.

CL4 cell shape measurements:

60X fields of 3DPC Control and CDHR2 KO CL4 cells stained for ZO-1 were analyzed in Elements using a custom General Analsysis 3 (GA3) pipeline. This involved first maximally projecting each image in Z followed by tight border segmentation. The binary was then inverted to highlight individual cells in the field and any "partial" cells touching the borders were eliminated from the selection. Cell area (μm^2) and elongation were measured from the remaining binaries. Elongation is quantified by the software as a ratio of maximum feret length over minimum feret length. A value of greater than 1 indicates that the cell is stretched in one of its axes.

CACO cell junction straightness measurements:

Three randomly selected 60X fields were taken from each of three experimental staining replicates and maximally projected in FIJI. The ZO-1 channel was isolated and junctional segments (between two vertices) were cropped using the rectangle selection tool. The cropped segment was then binarized and dilated to segment the ZO-1 signal marking the cell junction. Next, the binary was

skeletonized and the 2D skeleton was analyzed. Branch length and Euclidian distance were exported from the measurements list to Excel. Junction straightness was calculated as the ratio of Euclidean distance over the branch length, with 1 being the most straight, as previously described in the literature (Sumi et al., 2018). A total of 62 straightness ratios were calculated and plotted in Prism as a column data table and graphed as a violin plot. An unpaired t-test was performed to statistically compare the mean straightness of junctions in Control vs KO cells.

Wound healing velocity measurements:

Cell migration movies were maximally projected in FIJI and divided in half with a duplicated ROI. For the Control side, 20 randomly placed horizontal lines were drawn along the entire vertical axis of the leading edge of the cell monolayer to the opposite end of the ROI (the wound "midline"). The length, in μm, was recorded in Excel along with the time, minutes, it took to reach the midline and velocity was calculated from μm/min. For the KO side, which exhibited far less movement towards the wound midline, 20 randomly placed horizontal lines were drawn from the monolayer edge to the furthest point of migration. Both length of the line and time in the movie were recorded and velocity was calculated from μm/min. Each velocity measurement was plotted in FIJI in a column data sheet. An unpaired t-test was performed to test significance of the change in mean velocities between Control and KO cells.

CHAPTER III

ADHESION-BASED CAPTURE STABILIZES NASCENT MICROVILLI AT EPITHELIAL CELL JUNCTIONS

This chapter is adapted from Adhesion-based capture stabilizes nascent microvilli at epithelial cell junctions published in Developmental Cell (Cencer et al., 2023) and has been reproduced with the permission of the publisher and my co-authors Silverman JB, Meenderink LM, Krystofiak ES, Millis BA, and Tyska MJ.

Summary

To maximize solute transport, epithelial cells build an apical "brush border", where thousands of microvilli are linked to their neighbors by protocadherin-containing intermicrovillar adhesion complexes (IMACs). Previous studies established that the IMAC is needed to build a mature brush border, but how this complex contributes to the accumulation of new microvilli during differentiation remains unclear. We found that, early in differentiation, mouse, human, and porcine epithelial cells exhibit a marginal accumulation of microvilli, which span junctions and interact with protrusions on neighboring cells using IMAC protocadherins. These *transjunctional* IMACs are highly stable and reinforced by tension across junctions. Finally, long-term live imaging showed that accumulation of microvilli at cell margins consistently leads accumulation in medial regions. Thus, nascent microvilli are stabilized by a marginal capture mechanism that depends on the formation of transjunctional IMACs. These results may offer insight into how apical specializations are assembled in diverse epithelial systems.

Introduction

Organ function depends on specialized cell types that have evolved morphologies to enable specific physiological tasks. Transporting epithelial cells like those found in the intestine and kidney proximal tubule, offer interesting examples of this phenomenon. As important sites of solute uptake, maximizing apical surface area is critical for these tissues. To meet this challenge, individual epithelial cells extend 1000s of bristle-like protrusions called microvilli, which collectively form the 'brush border' (Coudrier et al., 1988; Sauvanet et al., 2015). A single microvillus is a cylinder-shaped, micron-scale membrane protrusion supported by a core actin bundle consisting of 20-40 actin filaments (Mooseker and Tilney, 1975; Ohta et al., 2012). By scaffolding apical membrane in this way, microvilli amplify surface area available for solute transport and optimize solute uptake potential (Delacour et al., 2016; Helander and Fandriks, 2014; Wessely et al., 2014). Microvilli first appear on the cell surface early in epithelial maturation; differentiating cells, like those found within intestinal stem cell-containing crypts, exhibit few, poorly organized microvilli (Fath et al., 1990). However, differentiated, fully functional enterocytes, found on the villus or within the kidney tubule, present a well-organized and densely packed brush border (Mooseker and Tilney, 1975; Rice et al., 2013; Specian and Neutra, 1981).

Previous studies established that tight microvillar packing is driven by a protocadherin-based intermicrovillar adhesion complex (IMAC), which physically links the distal tips of neighboring microvilli (Crawley et al., 2014b; Crawley et al., 2016; Pinette et al., 2019; Weck et al., 2016). In the enterocyte, these adhesive interactions give rise to a hexagonal packing pattern when viewed *en face*, which represents maximum surface occupancy. Previous work also identified protocadherins CDHR2 and CDHR5 as the primary adhesive elements in these links, which form *trans* heterophilic adhesion complexes that are well suited for bridging the ~50 nm

gap between neighboring microvilli (Crawley et al., 2014b; McConnell et al., 2011). CDHR2 and CDHR5 ectodomains contain multiple extracellular cadherin (EC) repeat motifs arranged in tandem, which are anchored to the membrane via a single spanning transmembrane domain (Gray et al., 2021). Both protocadherins also contain cytoplasmic tails at their C-termini, which enable direct interactions with cytoplasmic IMAC binding partners including the actin-based motor, myosin-7B (MYO7B), and the scaffolding proteins, ankyrin repeat and sterile alpha motif domain containing 4B (ANKS4B) and usher syndrome 1C (USH1C) (Crawley et al., 2016; Li et al., 2016; Li et al., 2017; Weck et al., 2016). Recently, calmodulin-like protein 4 (CALML4) was also identified as a binding partner of MYO7B, making it another IMAC component (Choi et al., 2020). KD studies of MYO7B indicate that this motor is required for the localization of CDHR2/CDHR5 adhesion complexes to the distal tips of microvilli (Crawley et al., 2016; Weck et al., 2016). In the CACO-2_{BBE} intestinal epithelial cell culture model, disrupting the function of the IMAC via calcium chelators or KD of any single complex component leads to striking defects in microvillar growth and packing organization during differentiation (Choi et al., 2020; Crawley et al., 2014b; Crawley et al., 2016; Weck et al., 2016). Furthermore, CDHR2 KO from intestinal and kidney epithelia in a villin-Cre driven knockout (KO) mouse, causes shortening and loss of brush border microvilli, a consequential decrease in the apical enrichment of key solute transporters, and reduced animal growth rate (Pinette et al., 2019).

How new microvilli assemble and incorporate into a highly ordered brush border during differentiation remains unclear. Ultrastructural studies of native tissue and time-lapse imaging of epithelial cell culture models indicate that microvilli do not grow synchronously, but instead appear stochastically on the apical surface throughout differentiation (Crawley et al., 2014b; Fath et al., 1990; Gaeta et al., 2021a). One critical factor that promotes microvillar growth is the barbed

end binder, epidermal growth factor receptor pathway substrate 8 (EPS8) (Croce et al., 2004; Gaeta et al., 2021a). Studies in multiple epithelial and non-epithelial systems have established that EPS8 is a highly specific marker of the distal ends of all forms of actin bundle supported protrusions (Croce et al., 2004; Disanza et al., 2006; Manor et al., 2011; Postema et al., 2018). Loss of this factor leads to shorter protrusions and increased length variability (Tocchetti et al., 2010; Zampini et al., 2011). Strikingly, on the apical surface of differentiating epithelial cells, EPS8 arrives in diffraction-limited puncta at the membrane minutes before the subsequent growth of a core actin bundle and assembly of a microvillus at these sites (Gaeta et al., 2021a). Even once a core bundle begins to elongate, EPS8 puncta remain persistently associated with the distal end of the nascent structure. Following their initial growth, nascent microvilli are highly motile and translocate across the apical surface via a mechanism powered by treadmilling of the underlying core actin bundle (Meenderink et al., 2019), an activity that is also regulated by EPS8 (Meenderink et al., 2019). Remarkably, if the distal tip of a newly formed microvillus loses its EPS8 punctum, that structure rapidly collapses, suggesting that EPS8 serves as a microvillus survival factor (Gaeta et al., 2021a). These data point to a previously unrecognized dynamic microvillus lifecycle, consisting of distinct phases of structural stability and instability. For microvilli to eventually accumulate in large numbers on the apical surface, this cycle must ultimately tilt in favor of stability. How dynamic, nascent microvilli are stabilized on the apical surface so that they eventually accumulate in large numbers remains unknown.

Here we report our discovery of an adhesion-based mechanism that epithelial cells use to stabilize and in turn, drive the accumulation of microvilli during differentiation. Because microvillar growth takes place as differentiating enterocytes move through the crypt-villus transition (Fath et al., 1990), we reasoned that we could gain insight on mechanisms of microvilli

accumulation by careful inspection of apical morphology in this region. Using this approach, we discovered that crypt microvilli initially accumulate at cell margins, implying the existence of a mechanism for anchoring nascent protrusions at these sites. We observed similar marginal accumulation of microvilli on the surface of differentiating intestinal and kidney epithelial cell lines. In all models examined, microvilli extending from one cell span intercellular space to make physical contact with microvilli on a neighboring cell. Using super-resolution microscopy, mechanistic studies in epithelial cell culture models, and live imaging, we determined that these points of physical contact represent *transjunctional* IMACs containing both CDHR2 and CDHR5, which are highly stable complexes that capture nascent microvilli and constrain their motion. Consistent with this point, long-term live imaging revealed that microvilli accumulation at cell margins outpaces accumulation in medial regions of the surface early in differentiation. Thus, microvilli extending from neighboring epithelial cells participate in cell-cell contacts that promote apical surface maturation. The adhesion-based capture mechanism reported here might also extend our understanding of apical morphogenesis in other epithelial cell types that build elaborate surface specializations.

Results

Differentiating epithelial cells exhibit a marginal enrichment of microvilli

To begin to understand how microvilli are stabilized and accumulate in large numbers during differentiation, we first examined the distribution of nascent protrusions early in the maturation process. To this end, we used scanning electron microscopy (SEM) to survey the apical surface of the crypt cells in fractured samples of mouse small intestine. Within the crypt, where immature enterocytes are actively assembling a brush border (**Fig. 3-1A, zoom**), we noted a striking enrichment of microvilli at cell margins (**Fig. 3-1B, zoom 1 and 2 blue outlines**). In

contrast, medial regions of the apical surface presented only a few, sparse microvilli (**Fig. 3-1B, zoom 1**). Thus, *in vivo*, microvilli appear to accumulate at the edges of cells during the early stages of brush border assembly.

To determine if the marginal accumulation of microvilli observed on the surface of differentiating crypt cells *in vivo* could be recapitulated *in vitro*, we first turned to the CACO-2_{BBE} line. CACO-2_{BBE} cells are a human intestinal epithelial culture model that builds a well-organized brush border over the course of several weeks post-confluency (Peterson and Mooseker, 1992). SEM imaging of CACO-2_{BBE} cells early in the differentiation time-course (8 days-post confluence) revealed a concentration of microvilli at cell margins similar to that observed in native crypts (**Fig 3-1C**). Moreover, protrusions in these regions appeared to span cell junctions and make physical contact with microvilli on neighboring cells (**Fig. 3-1C, zoom blue arrows)**. As an additional point of comparison, we used SEM to examine sub-confluent, partially differentiated "islands", of porcine kidney proximal tubule LLC-PK1 clone 4 (CL4) cells (Gaeta et al., 2021b; Nielsen et al., 1998), which also exhibited a marginal accumulation of microvilli (**Fig. 3-1D, zoom blue outline**), even at the earliest stages of cell surface organization (i.e. subconfluence). Based on these *in vivo* and *in vitro* observations, we conclude the differentiating apical surface is characterized by two distinct populations of microvilli, marginal and medial **(Fig. 3-1E)**, with the marginal region demonstrating higher protrusion density at these early time points.

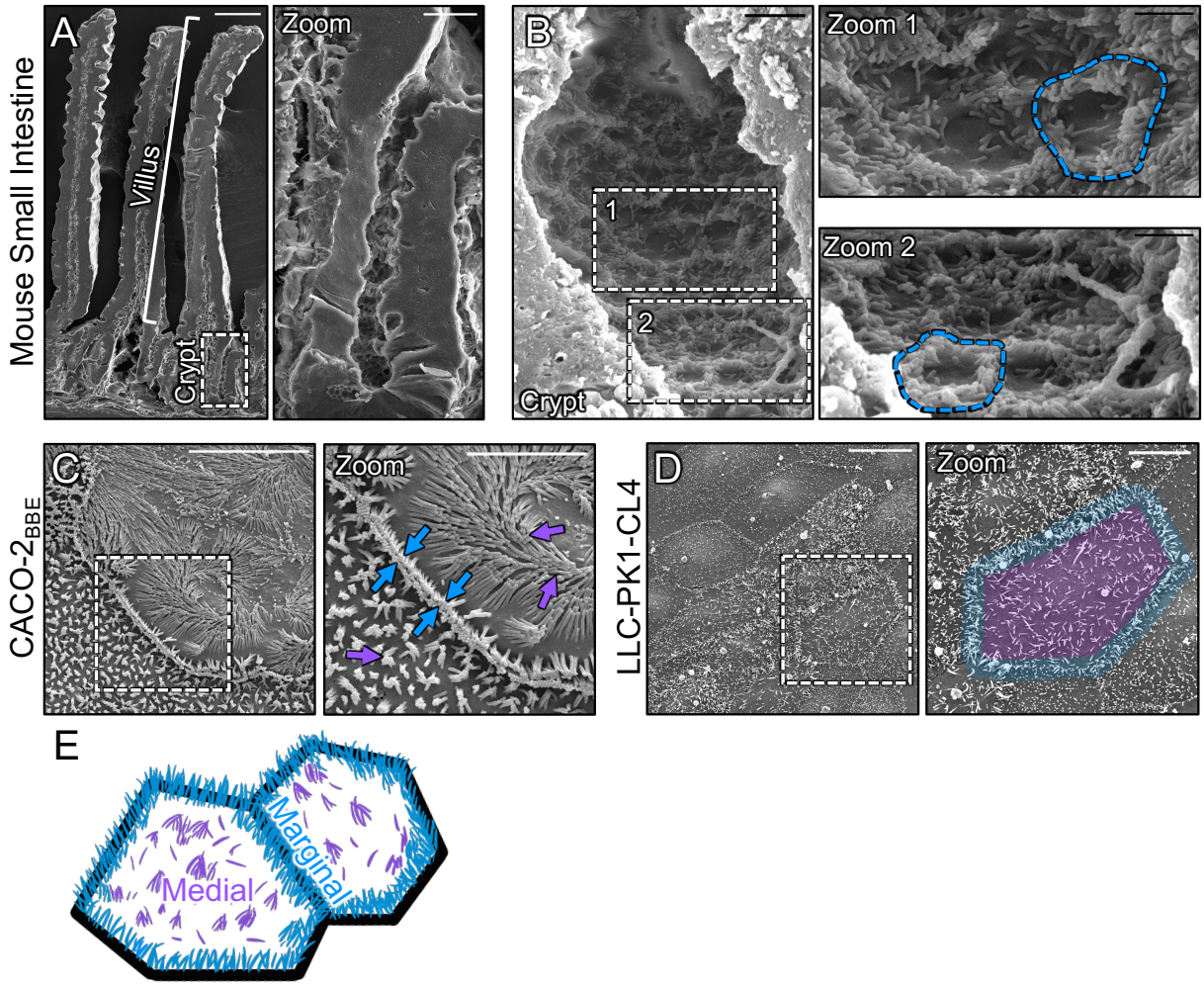

Figure 3-1. Microvilli of differentiating transporting epithelial cells concentrate at cell margins. (**A**) Scanning electron micrograph (SEM) of native mouse small intestine crypt-villus axis. (**A, zoom**) Zoom of the dashed box in A showing the crypt and transit amplifying zone. **(B**) High-magnification view of the crypt base with (**B, zooms 1 and 2**) showing an enrichment of microvilli at the margins of crypt cells (dashed blue outline). (**C**) SEM of 8 days post-confluence polarized CACO-2_{BBE} cells. Dashed box represents zoom area. Arrows denote medial (purple) and marginal microvilli (blue). (**D**) SEM of sub-confluent porcine kidney proximal tubule LLC-PK1-CL4 (CL4) cells. Dashed box represents zoom area. Pseudo coloring represents medial area (purple) and marginal microvillar area (blue). (**E**) Schematic of the two distinct organizations of microvilli found on differentiating transporting epithelial cells, medial (purple) and marginal (blue). Scale bars: 50 µm (A), 10 µm (A, zoom), 2 µm (B), 1 µm (B, zooms), 10 µm (C), 5 µm (C, zoom), 20 µm (D), 10 µm (D, zoom).

Microvilli adopt a vertical orientation upon arriving at cell margins

In the ultrastructural studies above, we noted that marginal microvilli appeared more vertically oriented relative to microvilli extending from medial parts of the cell surface. Here we use 'vertical' to describe an orientation that is parallel to the long (apicobasal) axis of the cell and perpendicular to the plane of the apical surface. To confirm this observation under hydrated conditions, we performed volume imaging of live sub-confluent CL4 cells expressing mCherry-Espin (ESPN), which serves as a highly specific marker of microvillar core actin bundles (Bartles et al., 1998; Gaeta et al., 2021a; Loomis et al., 2003; Meenderink et al., 2019) (**Fig. 3-2A**). Lateral views of reconstructed volumes enabled us to visualize individual microvilli and obtain measurements of their orientation relative to the plane of the apical surface. This analysis revealed that the marginal and medial microvilli demonstrate significant differences in their angle of protrusion, with marginal microvilli exhibiting a more vertical orientation (marginal, 77.3° ± 12.4° vs. medial, 46.5° ± 19.3, **Fig. 3-2B**).

Previous studies established that nascent microvilli are highly dynamic, growing, collapsing, and adopting a range of angles while undergoing active movement across the medial cell surface (Gaeta et al., 2021a; Meenderink et al., 2019). With this in mind, we next sought to determine if microvilli grow in a vertical orientation at marginal sites or instead, grow medially and then adopt a vertical orientation upon arriving at the cell edge. To this end, we performed multi-hour time-lapse volume imaging to record microvillar motion and orientation in 3D. To help us interpret these complex datasets, we depth-coded volumes with a multi-color look-up table (LUT) so that image planes located further from the apical surface were rendered with warmer colors. While the dense accumulation of microvilli at cell margins impaired our ability to resolve individual growth events at these sites, we did observe individual protrusions and small adherent

clusters of microvilli migrating while maintaining a small angle relative to the medial apical surface, as previously described (Gaeta et al., 2021a; Meenderink et al., 2019). Following these microvilli over 2 hrs revealed that upon reaching the cell margin, they become more vertically orientated as indicated by the distal tips acquiring a warmer color coding (**Figs. 3-2C,D**). Although these data do not allow us to rule out the possibility that microvilli grow *de novo* in a vertical orientation in the marginal zone, they do indicate that medial microvilli can transition into the marginal zone and adopt a vertical orientation when doing so.

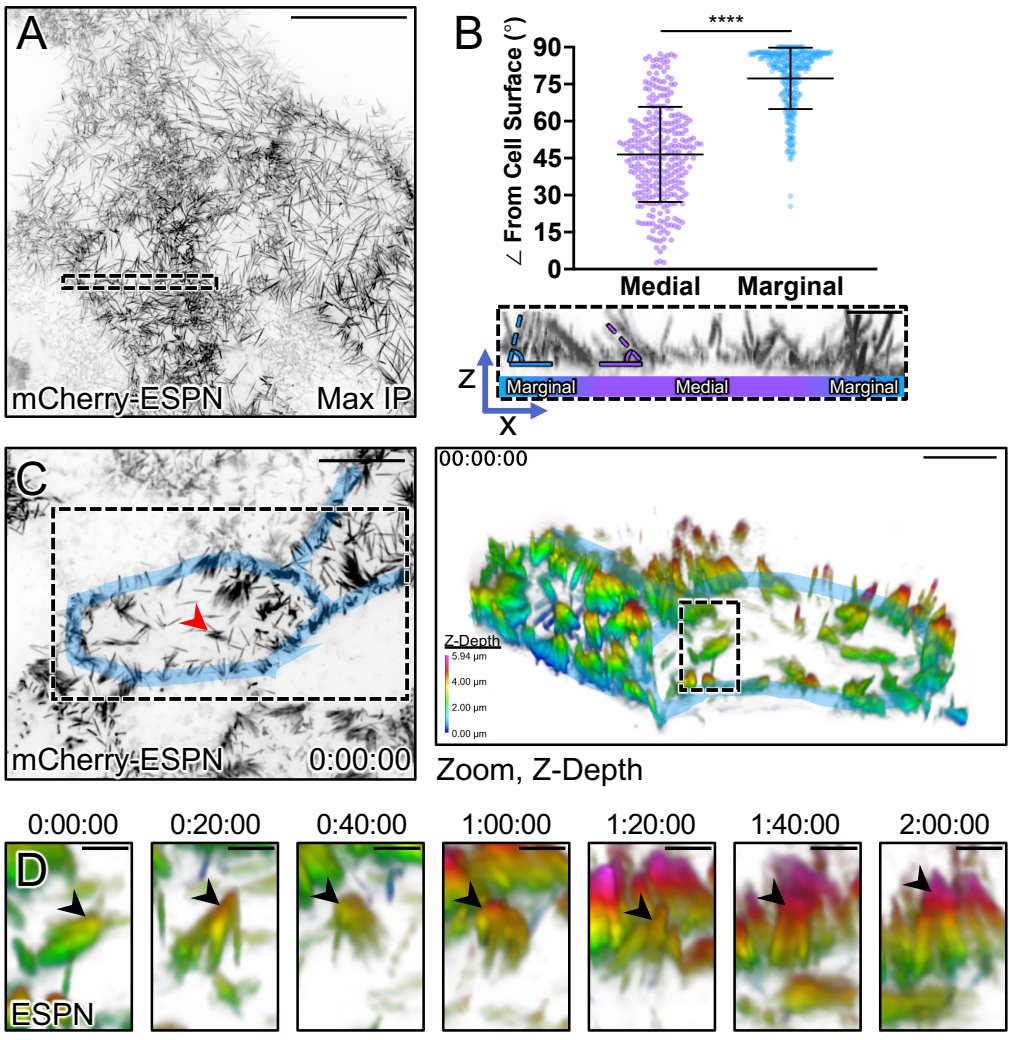

Figure 3-2. Microvilli adopt a vertical orientation upon reaching cell margins. (**A**) Maximum intensity projection (MaxIP) of live CL4 cells expressing mCherry-ESPN. (**B**) Orientation measurements of the angle (dashed outlines) of microvilli to the cell surface of medial microvilli (purple) compared to marginal microvilli (blue). Sample ROI of Z-projection under plot is taken from the dashed box in (A). (**C**) t = 0 MaxIP image of live mCherry-ESPN CL4 cells. Two neighboring cell margins are highlighted in blue, while the red arrowhead points to the microvilli cluster followed in (D). Right panel shows a 3D tilted volume of the dashed box in (C), coded in Z for cell depth (bottom left key). Cell margins are highlighted in blue. (**D**) Montage over 2 hours following the cluster marked with the red arrowhead/dashed box in (C). Arrowheads mark the distal ends of microvilli that transition to a vertical orientation upon reaching the marginal cell area, as shown by a change in Z-depth coding. Each point on the graph represents one angle taken from 17 cells; total of $n = 295$ medial and $n = 309$ marginal angles. Error bars represent mean ± SD. **** $p \leq 0.0001$ Welch's unpaired t-test. Mean medial angle is 46.5° ± 19.3° and mean marginal angle is 77.3° ± 12.4°. Scale bars: 20 µm (A), 1 µm (B), 10 µm (C, left), 5 µm (C, right), 1.5 µm (D).

Marginal microvilli are less motile than medial microvilli

Vertically orientated microvilli are a defining feature of mature brush borders on the surface of villus enterocytes (Mooseker and Tilney, 1975). Based on this point, the vertically oriented microvilli found in the marginal zone may represent more mature, and potentially, more stable protrusions. To test this concept, we expressed EGFP-EPS8 to specifically mark the distal tips of microvilli(Gaeta et al., 2021a; Higgs, 2004) in CL4 cells also expressing mCherry-ESPN (**Fig. 3-3A, zooms**). We then performed live volume imaging with the goal of using the punctate and stoichiometric EPS8 signal (one punctum per microvillus) as a marker for tracking microvillar dynamics over time. Temporal color coding of the ESPN channel over the course of 25 minutes revealed that medial microvilli are highly dynamic and demonstrate extensive movement as previously reported (Meenderink et al., 2019) (**Fig. 3-3B, zoom 1**). In contrast, marginal microvilli dwelled for long periods near the edge of the cell, as indicated by the white band of color (merged colors of time points 0-25 min) in the projection (**Fig. 3-3B, zoom 2**). Next, we tracked individual EGFP-EPS8 puncta and generated rose plots of the resulting trajectories to examine the extent of motion demonstrated by individual microvilli. This analysis revealed that medial microvilli produce long trajectories consistent with directed motion, sampling an area of up to 6 μm^2 during the time-lapse (**Figs. 3-3C,D**). By comparison, the trajectories of marginal microvilli were highly confined, with individual protrusions traveling less than 2 μm^2 during the same period (**Figs. 3-3F,G**). Mean squared displacement (MSD) analysis of trajectory data also indicated that medial protrusions demonstrate active motion as previously reported (Meenderink et al., 2019) (**Fig. 3-3E**), whereas marginal microvilli exhibit constrained diffusion with a sub-micron confinement radius (**Fig. 3-3H**). Together, these data suggest the existence of a mechanism for restricting the motion of microvilli at cell margins.

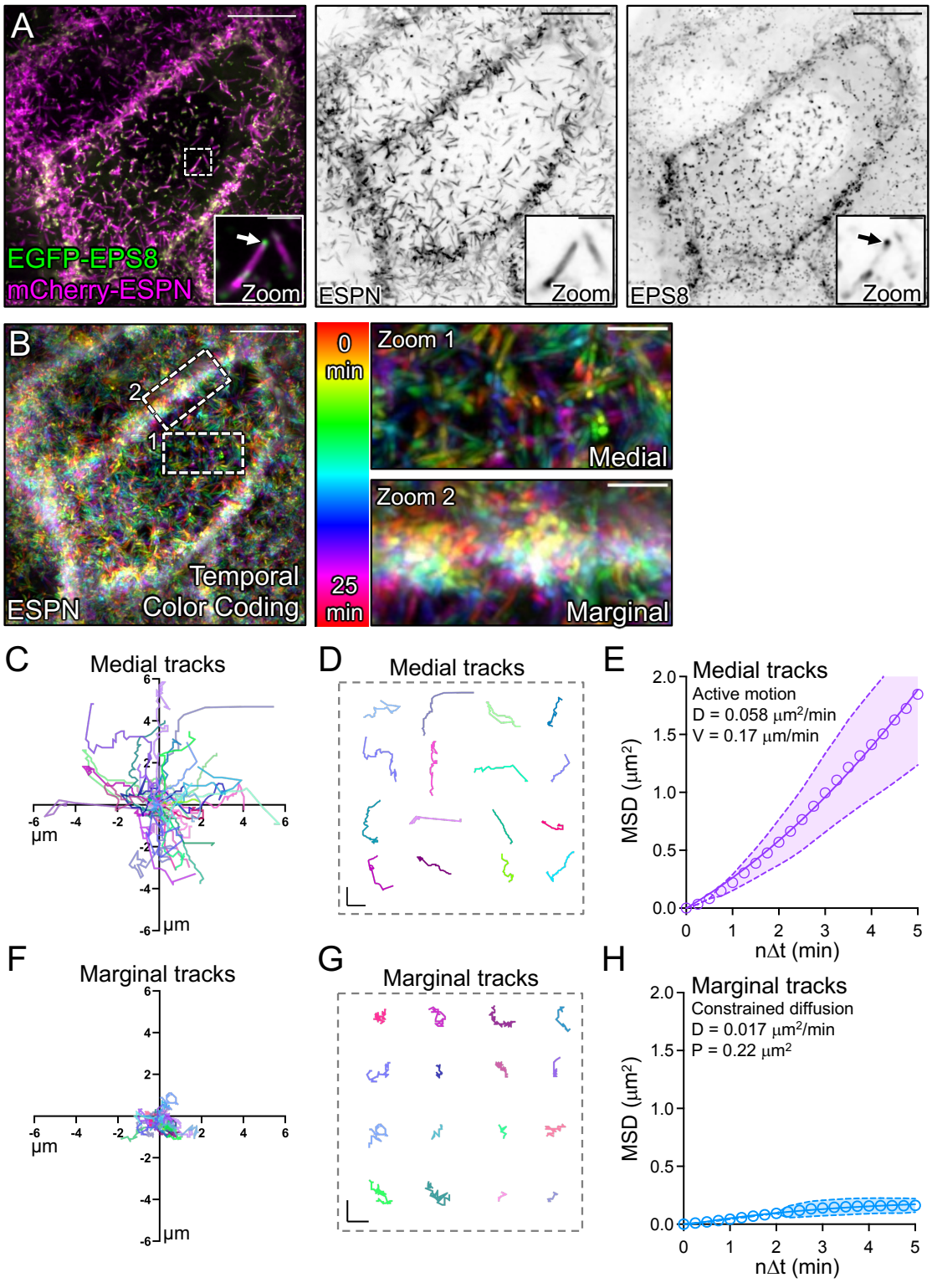
A
EGFP-EPS8
mCherry-ESPN
Zoom
ESPN
Zoom
EPS8
Zoom
B
2
1
ESPN
Temporal
Color Coding
0
min
25
min
Zoom 1
Medial
Zoom 2
Marginal
C
Medial tracks
µm
µm
D
Medial tracks
E
Medial tracks
Active motion
D = 0.058 µm²/min
V = 0.17 µm/min
MSD (µm²)
nΔt (min)
F
Marginal tracks
µm
µm
G
Marginal tracks
H
Marginal tracks
Constrained diffusion
D = 0.017 µm²/min
P = 0.22 µm²
MSD (µm²)
nΔt (min)

Figure 3-3. Tip tracking analysis reveals that marginal microvilli are constrained in their movement. (**A, left panel**) Live CL4 cells co-expressing EGFP-EPS8 and mCherry-ESPN. Dashed box represents zoom area with arrow marking EPS8 at the tip of a single microvillus. (**A, right panels**) Single inverted channel MaxIP images showing mCherry-ESPN and EGFP-EPS8 alone. (**B**) Temporal color-coding over 25 minutes (see vertical color key). (**B, zooms**) of (**1**) medial and (**2**) marginal ROIs taken from the dashed boxes in (B). (**C**) Rose plot of *n = 53* XY tracks (μm units) of medial microvilli over 25 minutes. (**D**) Representative medial microvilli tracks taken from (C). (**E**) Mean square displacement (MSD) of 50 medial microvilli imaged for 5 minutes over 15 second intervals; magenta open circles represent mean MSD values, magenta color band indicates the 95% CI, and the solid magenta line indicates a best fit of the data to an active motion model with D = 0.058 μm^2/min and V = 0.17 μm/min. (**F**) Rose plot of *n = 28* XY tracks of marginal microvilli taken from 3 independent live cell imaging experiments over 25 minutes. (**G**) Representative marginal microvilli tracks taken from (F). (**H**) MSD analysis of *n = 88* marginal microvilli; blue open circles represent the mean MSD values, blue color band indicates the 95% CI, and the solid blue line indicates a best fit to a constrained diffusion model with D of 0.017 μm^2/min and a plateau of confinement at 0.22 μm^2. Scale bars: 10 μm (A), 1.5 μm (A, zooms), 10 μm (B), 2.5 μm (B, zooms), 1 μm (D, G).

Microvilli from neighboring cells are linked by transjunctional adhesion complexes containing CDHR2 and/or CDHR5

Our ultrastructural data suggested that marginal accumulations of microvilli might include protrusions from both cells of a neighboring pair (**Fig. 3-1C, zoom**). This led us to consider the possibility that microvilli extending from one cell may span the junctional space and physically contact microvilli from an adjacent cell; such interactions might in turn explain the upright orientation, reduced motility, and accumulation of microvilli at these sites. One potential mechanism for mediating such interactions involves the intermicrovillar adhesion complex (IMAC), which includes the protocadherins CDHR2 and CDHR5 as core components (Crawley et al., 2014b). Previous studies established that CDHR2 and CDHR5 target to the distal tips of microvilli and interact with each other to form a Ca^{2+}-dependent heterophilic extracellular adhesion complex that spans the ~50 nm between adjacent protrusions (Crawley et al., 2014b; Fath et al., 1990; Rice et al., 2013; Specian and Neutra, 1981). The resulting link promotes the tight packing of neighboring microvilli and contributes to minimizing length variability throughout the larger structure of the brush border (Pinette et al., 2019). Notably, these previous studies on IMAC function focused solely on *medial* microvilli, so the possibility that this complex might also link microvilli from neighboring cells remains unexplored.

To test this idea, we used an immunostaining approach and super-resolution structured illumination microscopy (SIM) to examine the localization of CDHR2, CDHR5, and F-actin relative to ZO-1, a critical component of tight junctions (Stevenson et al., 1986). For these studies, we first examined native small intestinal tissues isolated from a new mouse model expressing CDHR2 tagged with EGFP at the endogenous locus (**Fig. 3-4**). SIM images revealed that both IMAC protocadherins are highly enriched at the tips of medial microvilli as previously reported

(**Fig. 3-5A**) (Crawley et al., 2014b). We also noted signal from CDHR2 and CDHR5 at the tips of microvilli at the margins of cells, with the adhesion protein signal spanning ZO-1 marked junctions (**Fig. 3-5B**). When viewing projected SIM volumes *en face*, we were unable to discern the position of the tight junctions based solely on the phalloidin, CDHR2, or CDHR5 signals, suggesting that the IMAC components form a continuous network that spans beyond the surface of a single cell (**Fig. 3-5C**). Similarly, on the surface of mature enterocytes viewed with electron microscopy, brush border microvilli are so tightly packed they appear form a continuous array that extends across the surface of multiple cells (**Fig. 3-6A-B**). However, the crowded nature of microvilli in these mature brush borders confounded our attempts to isolate and visualize interactions between the tips of individual protrusions at the margins of neighboring cells.

To work around the limitation imposed by microvillar crowding in native tissue, we used SIM to examine the apical surface of cultured CACO-2_{BBE} cells at 12 days post-confluence (DPC), a time point *before* brush border assembly is complete, when microvillar packing density is low. Careful examination of phalloidin-stained CACO-2_{BBE} monolayers revealed a striking enrichment and alignment of microvilli at the margins of cells (**Fig. 3-5D,E**), consistent with the SEM images described above. Immunofluorescence staining of these 12 DPC cultures revealed that marginally aligned microvilli do in fact span the cell junction marked by ZO-1 and exhibit enrichment of both protocadherins at their distal tips (**Fig. 3-5D,E, white arrows**). We observed similar structures and staining on the surface of CL4 monolayers at 3 DPC, a stage in differentiation when microvilli are still sparse but begin to form clusters and demonstrate marginal alignment (**Fig. 3-5F**). In this case, super-resolution lateral views clearly showed that individual microvilli from neighboring cells span the ZO-1-labeled tight junction and make contact via their distal tips, which are marked by both CDHR2 and CDHR5 (**Fig. 3-5G, zooms**). In combination, these results indicate that marginal

microvilli on neighboring cells are physically linked via *transjunctional* IMACs that contain CDHR2 and CDHR5.

A **Annotated sequence of Cdhr2-eGFP ssDNA donor (944 nt, sense strand):**

Key: **Cdhr2 Exon**, LINKER, eGFP, *3'UTR*, flanking genomic DNA

GCCCCTGACTGCAGTGCTCTCAGGAAGGTCGGCAGGTGCGAGCGAACAGCAGAAAAAG
AATCTGTCCTTCACCAACCCTGGCCTGGACACCACAGATCTGagcggcggaggtagcggaggtggc
agcATGGTGAGCAAGGGCGAGGAGCTGTTCACCGGGGTGGTGCCCATCCTGGTCGAGCTG
GACGGCGACGTAAACGGCCACAAGTTCAGCGTGTCCGGCGAGGGCGAGGGCGATGCCAC
CTACGGCAAGCTGACCCTGAAGTTCATCTGCACCACCGGCAAGCTGCCCGTGCCCTGGCC
CACCCTCGTGACCACCCTGACCTACGGCGTGCAGTGCTTCAGCCGCTACCCCGACCACAT
GAAGCAGCACGACTTCTTCAAGTCCGCCATGCCCGAAGGCTACGTCCAGGAGCGCACCAT
CTTCTTCAAGGACGACGGCAACTACAAGACCCGCGCCGAGGTGAAGTTCGAGGGCGACA
CCCTGGTGAACCGCATCGAGCTGAAGGGCATCGACTTCAAGGAGGACGGCAACATCCTG
GGGCACAAGCTGGAGTACAACTACAACAGCCACAACGTCTATATCATGGCCGACAAGCAG
AAGAACGGCATCAAGGTGAACTTCAAGATCCGCCACAACATCGAGGACGGCAGCGTGCAG
CTCGCCGACCACTACCAGCAGAACACCCCCATCGGCGACGGCCCCGTGCTGCTGCCCGA
CAACCACTACCTGAGCACCCAGTCCGCCCTGAGCAAAGACCCCAACGAGAAGCGCGATCA
CATGGTCCTGCTGGAGTTCGTGACCGCCGCCGGGATCACTCTCGGCATGGACGAGCTGTA
CAAGTGA*CGGAGCCTGTCATTCTTCGAGCTCAAACCGTACTGTCTGCCCTCCCCTAAAATA*
*TAATATATGGCCTTGCTTGTCAATCATA*gacaagagttgggga

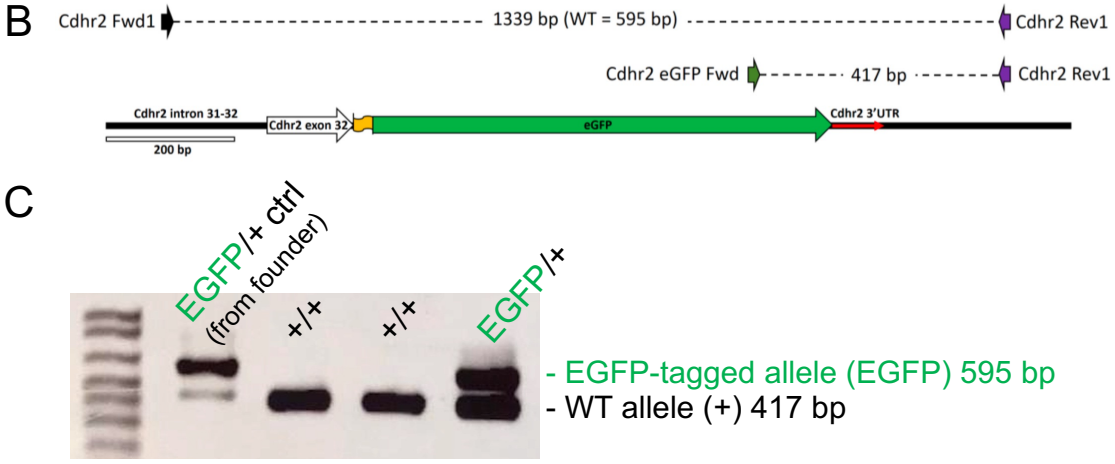

Figure 3-4. Strategy and validation of the CDHR2-EGFP knock-in mouse model. (**A**) Endogenous tagging strategy used to insert EGFP (green text) at the 3' end of mouse *CDHR2* allele (black text) in C57Bl/6N mice**.** (**B**) PCR strategy to screen for the presence of EGFP-tagged *CDHR2*. (**C**) Representative PCR outcomes showing bands for control (*CDHR2*$^{+/+}$) and heterozygous (*CDHR2*$^{EGFP/+}$) CDHR2-EGFP mice.

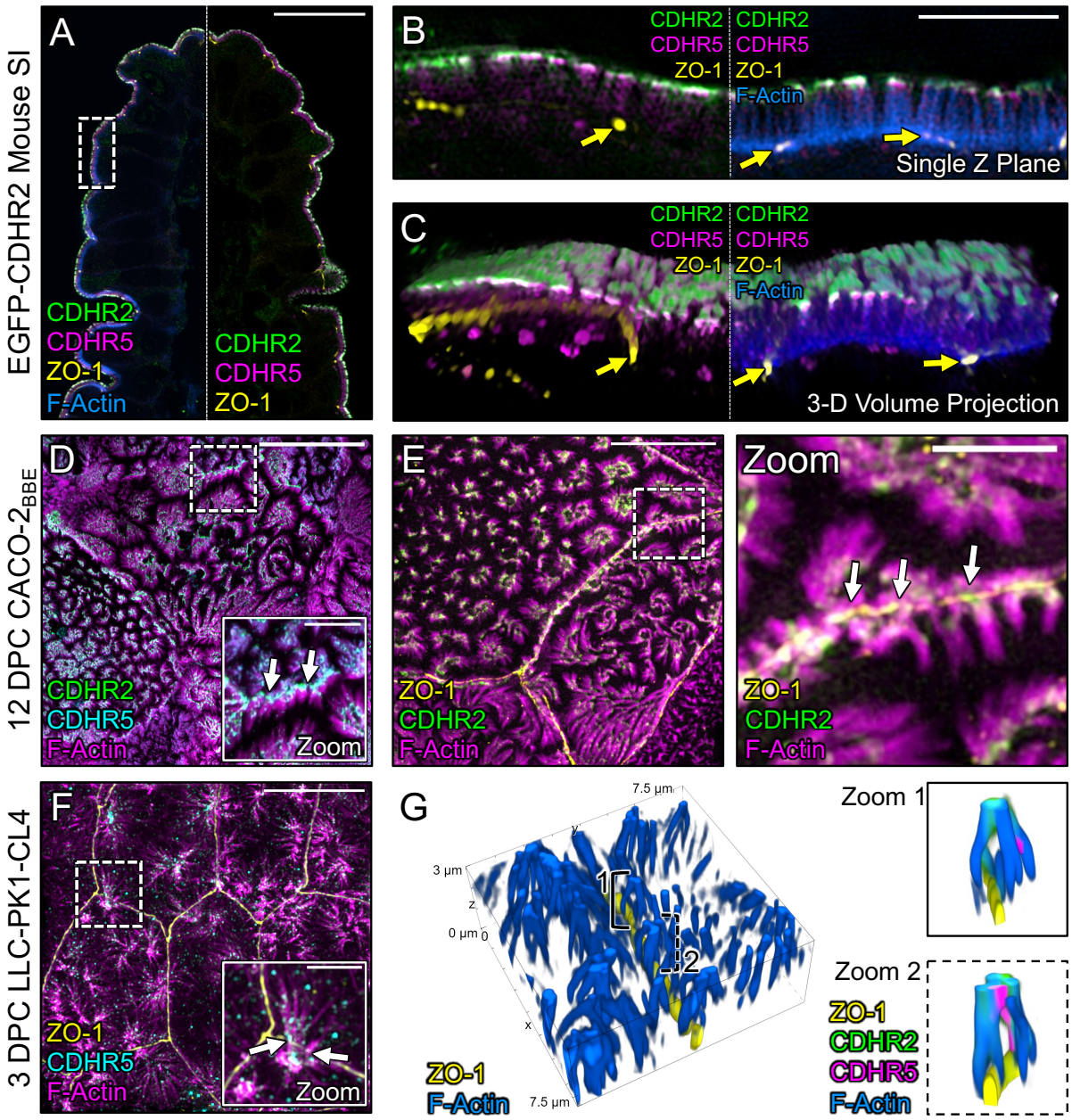
EGFP-CDHR2 Mouse SI
12 DPC CACO-2BBE
3 DPC LLC-PK1-CL4
A
CDHR2
CDHR5
ZO-1
F-Actin
CDHR2
CDHR5
ZO-1
B
CDHR2
CDHR5
ZO-1
CDHR2
CDHR5
ZO-1
F-Actin
Single Z Plane
C
CDHR2
CDHR5
ZO-1
CDHR2
CDHR5
ZO-1
F-Actin
3-D Volume Projection
D
CDHR2
CDHR5
F-Actin
Zoom
E
ZO-1
CDHR2
F-Actin
Zoom
ZO-1
CDHR2
F-Actin
F
ZO-1
CDHR5
F-Actin
Zoom
G
7.5 µm
y
3 µm
z
0 µm
0
1
2
x
ZO-1
F-Actin
7.5 µm
Zoom 1
Zoom 2
ZO-1
CDHR2
CDHR5
F-Actin

Figure 3-5. Marginal microvilli are linked via transjunctional CDHR2/CDHR5 adhesion complexes that extend across neighboring cell junctions. (**A**) Single Z-plane confocal image of CDHR2-EGFP mouse small intestine stained for ZO-1 (yellow), EGFP (green), CDHR5 (magenta), and F-actin (blue). (**B**) Single plane SIM image of the stained villus section; approximated area marked by the dashed box in (A). (**C**) 3D volume projection of the section in (B). Yellow arrows in both images mark ZO-1 labeled tight junctions. (**D**) MaxIP laser-scanning confocal image of 12 DPC CACO-2_{BBE} cells stained for CDHR2 (green), CDHR5 (cyan), and F-actin (magenta). Dashed box represents zoom area. White arrows point to tip localized CDHR2/CDHR5 adhesion complexes at cell margins. (**E**) MaxIP SIM image of 12 DPC CACO-2_{BBE} cells stained for ZO-1 (yellow), CDHR2 (green), and F-actin (magenta). Dashed box represents zoom area. White arrows point to CDHR2/CDHR5 marked complexes at the junction of neighboring cells. (**F**) MaxIP SIM image of 3 DPC CL4 cells stained for ZO-1 (yellow), CDHR5 (cyan), and F-actin (magenta). (**G**) 3D tilted volume projection of 3 DPC CL4 cells stained for ZO-1 (yellow), CDHR2 (green), CDHR5 (magenta), and F-actin (blue). Brackets highlight instances of marginal microvilli on adjacent cells linked via CDHR2/CDHR5 transjunctional adhesion complexes (**zoom 1 and 2**). Scale bars: 20 μm (A), 5 μm (B), 5 μm (D), 2.5 μm (D, zoom), 10 μm (E), 2.5 μm (E, zoom), 10 μm (F), 2.5 μm (F, zoom).

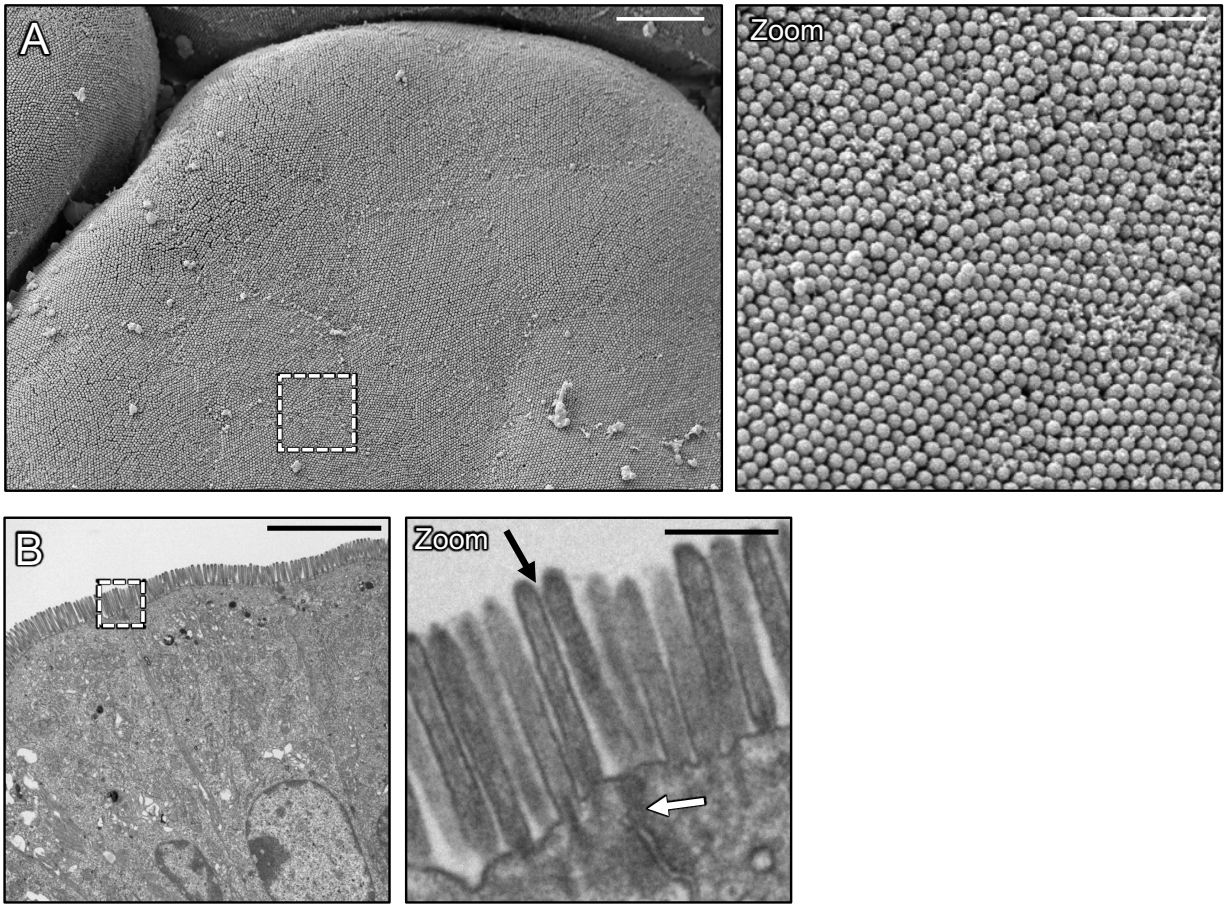

Figure 3-6. Mature villus enterocyte cells exhibit continuous packing of microvilli across cell junctions. (**A**) SEM of mouse small intestine showing an *en face* view of microvilli on neighboring enterocytes. The dashed box represents a zoom of a single enterocyte cell and its neighbors. (**B**) Transmission electron micrograph (TEM) of mouse small intestine showing a lateral view of microvilli. Dashed box represents the zoom of a cell-cell junction (white arrow) with neighboring cell microvilli appearing continuous across the interface (black arrow). Scale bars: 4 µm (A), 1 µm (A, zoom), 5 µm (B), 500 nm (B, zoom).

Heterophilic adhesion between CDHR2 and CDHR5 promotes robust association between microvilli from neighboring cells

Although IMAC protocadherin adhesion properties differ across species (Gray et al., 2021), previous biochemical studies established that in humans, heterophilic complexes of CDHR2 and CDHR5 exhibit strong adhesion, CDHR2 demonstrates weak homophilic adhesion, and CDHR5 demonstrates no homophilic adhesion (Crawley et al., 2014b). To further study the nature of transjunctional IMACs, we developed a cell mixing approach that enabled us to drive the formation of adhesion complexes consisting of different complements of CDHR2 and/or CDHR5 (**Fig. 3-7A**). For these experiments, we first transfected CL4 cells with either EGFP or mCherry-tagged constructs of *H. sapiens* CDHR2 and CDHR5. Stable selection and subsequent fluorescence-activated cell sorting (FACS) yielded robust populations of fluorescent protocadherin expressing cells (**Fig. 3-8A**). Strikingly, mixed monolayers composed of cells expressing CDHR2-EGFP or CDHR5-mCherry demonstrated robust alignment of protocadherin signals at mixed cell-cell contacts (**Fig. 3-7B**). Linescan analysis also revealed that CDHR2 and CDHR5 intensities were well correlated (mean r = 0.70) along these interfaces (**Fig. 3-7C,D,K**). These data are consistent with the formation of heterophilic adhesion complexes between microvilli of neighboring cells. In mixed monolayers composed of cells expressing CDHR2-EGFP or CDHR2-mCherry (**Fig. 3-7E**), mixed cell-cell contacts lacked the strong alignment of signals that we observed in the heterophilic case, and protocadherin intensities were poorly correlated (mean r = 0.07 (**Fig. 3-7F,G,K**). Mixed monolayers composed of cells expressing CDHR5-EGFP or CDHR5-mCherry also demonstrated a lack of signal alignment and poor intensity correlation along cell junctions (mean r = -0.19) (**Fig. 3-7H-K**). High-resolution imaging of the interfaces formed under each of these three conditions revealed that only heterophilic mixtures of cells

expressing CDHR2-EGFP or CDHR5-mCherry aligned their microvilli at cell-cell contacts (**Fig. 3-8B-D, white arrows**). Based on these data, we conclude that heterophilic transjunctional IMACs containing CDHR2 and CDHR5 can drive robust interactions between microvilli extending from neighboring cell margins.

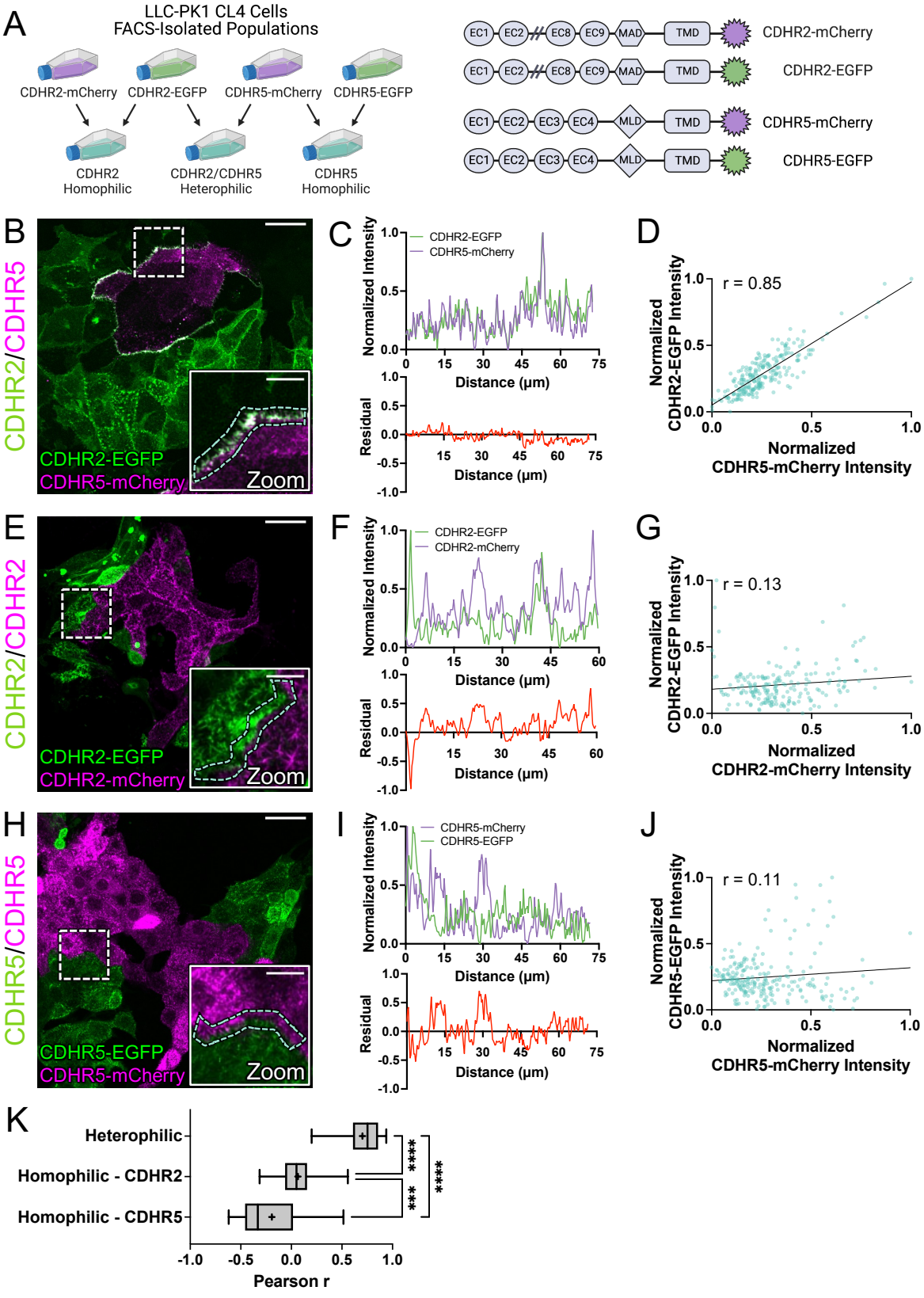
A
LLC-PK1 CL4 Cells
FACS-Isolated Populations
CDHR2-mCherry
CDHR2-EGFP
CDHR5-mCherry
CDHR5-EGFP
CDHR2 Homophilic
CDHR2/CDHR5 Heterophilic
CDHR5 Homophilic
EC1 EC2 EC8 EC9 MAD TMD CDHR2-mCherry
EC1 EC2 EC8 EC9 MAD TMD CDHR2-EGFP
EC1 EC2 EC3 EC4 MLD TMD CDHR5-mCherry
EC1 EC2 EC3 EC4 MLD TMD CDHR5-EGFP
B
CDHR2/CDHR5
CDHR2-EGFP
CDHR5-mCherry
Zoom
C
CDHR2-EGFP
CDHR5-mCherry
Normalized Intensity
Residual
Distance (μm)
D
r = 0.85
Normalized CDHR2-EGFP Intensity
Normalized CDHR5-mCherry Intensity
E
CDHR2/CDHR2
CDHR2-EGFP
CDHR2-mCherry
Zoom
F
CDHR2-EGFP
CDHR2-mCherry
Normalized Intensity
Residual
Distance (μm)
G
r = 0.13
Normalized CDHR2-EGFP Intensity
Normalized CDHR2-mCherry Intensity
H
CDHR5/CDHR5
CDHR5-EGFP
CDHR5-mCherry
Zoom
I
CDHR5-mCherry
CDHR5-EGFP
Normalized Intensity
Residual
Distance (μm)
J
r = 0.11
Normalized CDHR5-EGFP Intensity
Normalized CDHR5-mCherry Intensity
K
Heterophilic
Homophilic - CDHR2
Homophilic - CDHR5
****
***
****
Pearson r

Figure 3-7. Cell mixing experiments reveal robust heterophilic adhesion complexes between marginal microvilli. (**A, left**) Schematic depicting cell mixing method for the C-terminally tagged cadherin overexpression constructs (**A, right**). (**B**) MaxIP laser scanning confocal image of mixed heterophilic CDHR2-EGFP and CDHR5-mCherry CL4 cell populations. Dashed box represents zoom area and cyan dashed outline represents sample linescan. (**C**, **top**) Normalized fluorescence intensity plot taken from a representative linescan along the mixed cell interface. (**C, bottom**) Plotted difference (residual) of mCherry signal from EGFP signal from the top linescan plot. (**D**) Pearson's r correlation plot from the linescan in (C); r = 0.85. (**E**) MaxIP of mixed homophilic CDHR2-EGFP and CDHR2-mCherry CL4 cells. (**F-G**) Representative linescan and respective Pearson's r correlation; r = 0.13. (**H**) MaxIP of mixed homophilic CDHR5-EGFP and CDHR5-mCherry CL4 cells. (**I-J**) Representative linescan and respective Pearson's r correlation; r = 0.11. (**K**) Combined Pearson's r values from *n = 30* individual linescans of each cell mixing scenario from 3 independent fixation and staining experiments (10 linescans per experiment). Mean Pearson's r values are denoted by a "+" for each scenario where heterophilic r = 0.70, homophilic CDHR2 r = 0.07, and homophilic CDHR5 r = -0.19. Ordinary one-way ANOVA with multiple comparisons; **** $p \leq 0.0001$ and *** $p \leq 0.001$. Scale bars: 30 μm (B, E, H), 10 μm (zoom insets).

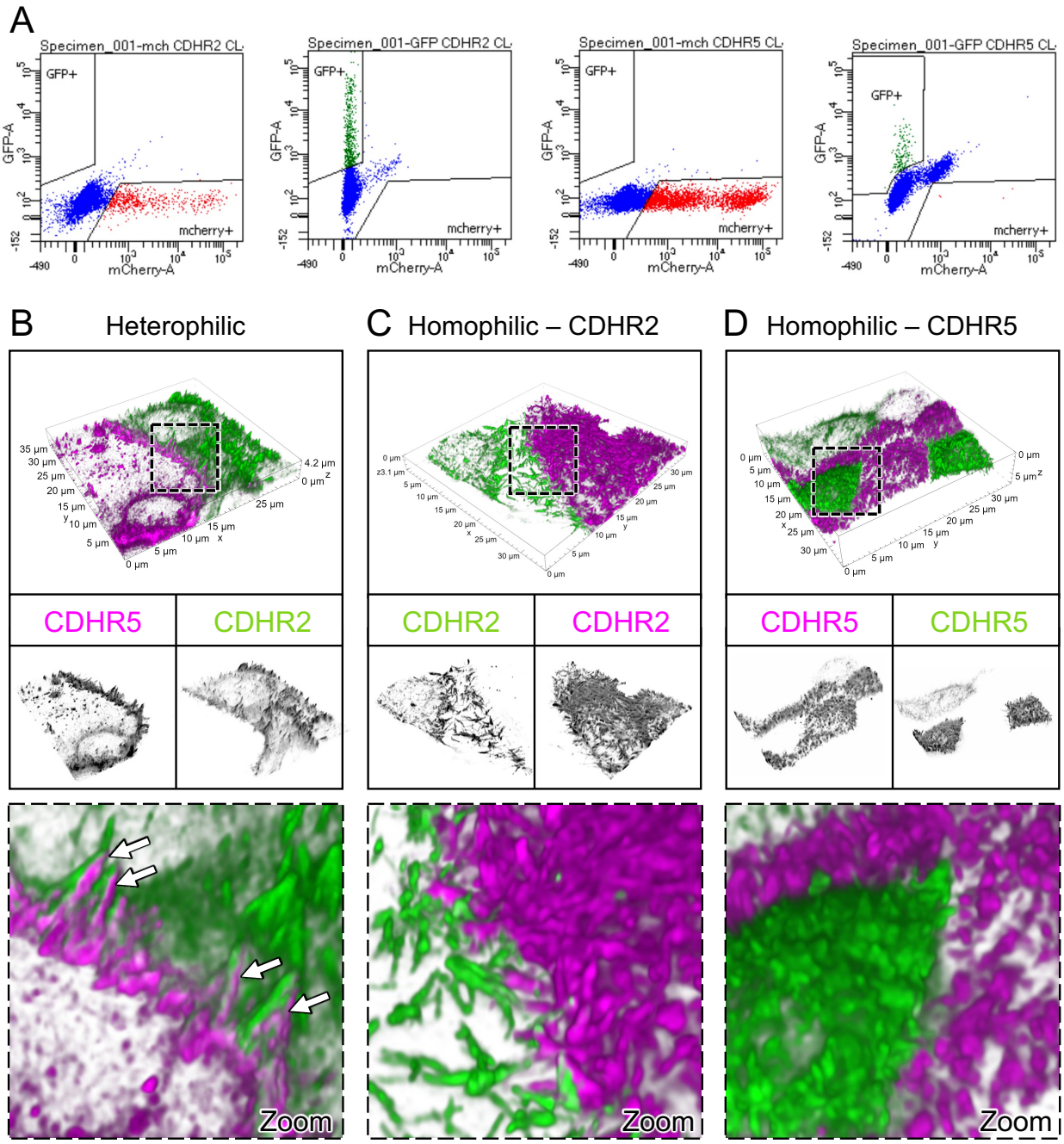

Figure 3-8. High-resolution imaging of adhesion complex interfaces in mixed CL4 cell populations. (A) FACS profiles of the four stable CL4 cell lines expressing C-terminal mCherry or EGFP tagged CDHR2 or CDHR5 as marked on the top axis of the graph. 3D Volume SIM images of mixed **(B)** heterophilic; CDHR5-mCherry and CDHR2-EGFP, **(C)** homophilic; CDHR2-EGFP and mCherry-CDHR5, and **(D)** homophilic; CDHR5-mCherry and CDHR5-EGFP CL4 cells. Dashed boxes outlined in B-D represent zooms shown in bottom panel, respectfully. White arrows in zoom under (B) point to instances of robust microvilli alignment at cell margins, which are absent in the homophilic mixing scenarios. Scaled as marked.

The cell mixing experiments described above indicate the heterophilic complexes of CDHR2 and CDHR5 are sufficient to drive microvilli alignment and accumulation at cell margins. We next asked if the endogenous IMAC protocadherins are required for transjunctional clustering of microvilli under normal conditions. To this end, we used CRISPR/Cas9 to generate CDHR2 KO in the CL4 line. Several KO lines were clonally selected and subsequently validated with genomic sequencing and antibody staining (**Fig. 3-9**). We then created mixed monolayers containing control and CDHR2 KO CL4 cells (**Fig. 3-10A**) and performed immunofluorescent staining to examine microvillar clustering; staining for endogenous CDHR2 enabled us to distinguish between control and CDHR2 KO cells in these samples. As expected, we noted robust accumulation of microvilli across control/control cell junctions (**Fig. 3-10B, left panel**). However, junctions formed between neighboring CDHR2 KO cells demonstrated little to no accumulation of microvilli; medial regions of the apical surface were also devoid of microvillar clusters (**Fig. 3-10B, right panel**). These data extend previous loss-of-function studies (Crawley et al., 2014b; Pinette et al., 2019) by revealing that CHDR2 is required for the formation of transjunctional IMACs, which are needed for the marginal accumulation of microvilli observed under normal conditions. Also consistent with previous studies (Crawley et al., 2016; Pinette et al., 2019), CDHR2 KO cells demonstrated reduced CDHR5, most likely because this protocadherin becomes destabilized in the absence of its heterophilic binding partner. However, the remaining low level of CDHR5 was sufficient to support limited clustering of microvilli at junctions formed with control cells, presumably by complexing with CDHR2-presenting microvilli in those cells (**Fig. 3-10B, middle panel**).

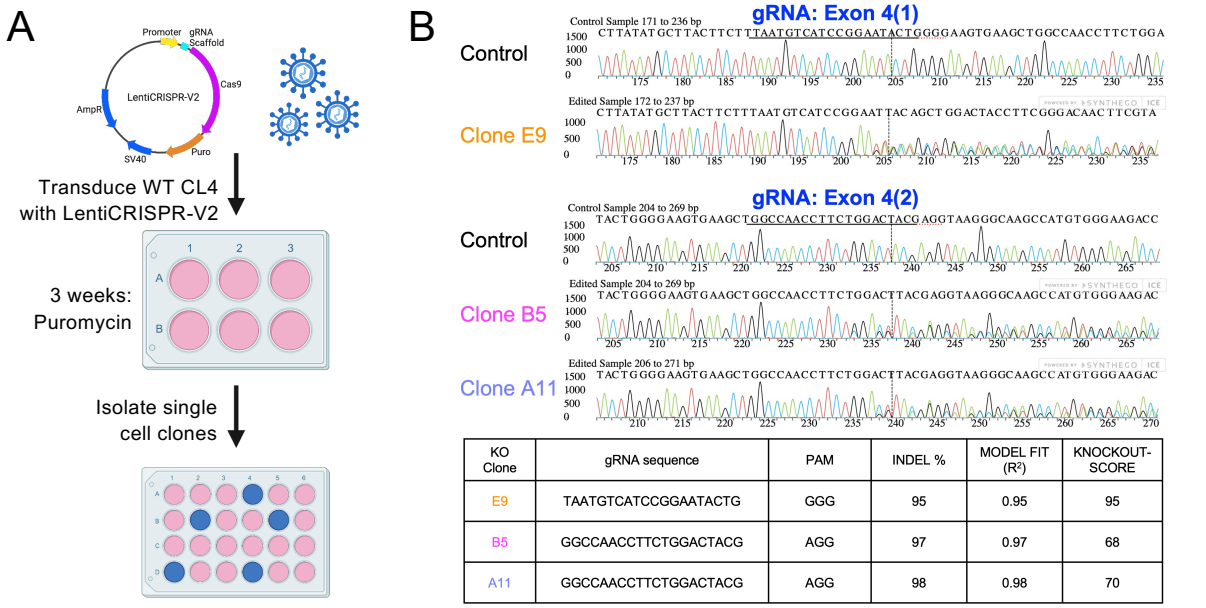

KO Clone	gRNA sequence	PAM	INDEL %	MODEL FIT (R^2)	KNOCKOUT-SCORE
E9	TAATGTCATCCGGAATACTG	GGG	95	0.95	95
B5	GGCCAACCTTCTGGACTACG	AGG	97	0.97	68
A11	GGCCAACCTTCTGGACTACG	AGG	98	0.98	70

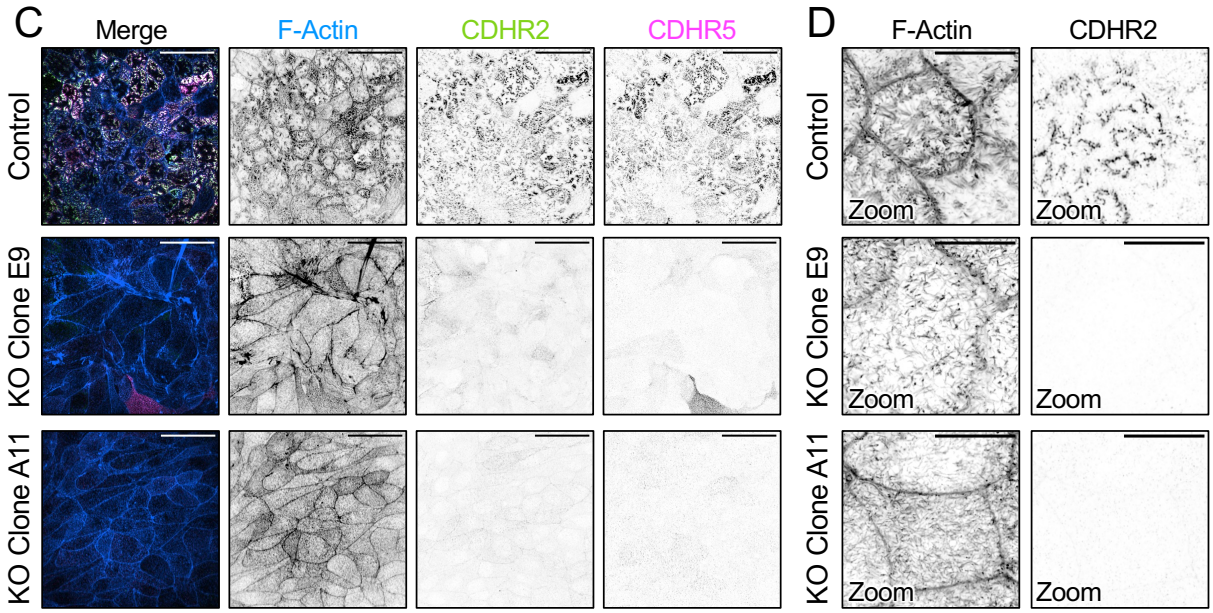

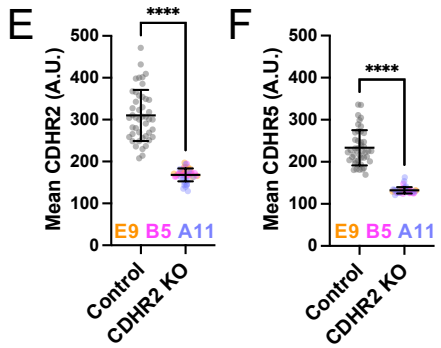

Figure 3-9. Generation and validation of CDHR2 KO CL4 cells. (**A**) Schematic depicting the lentiCRISPRv2 system. The plasmid contains a guide RNA (gRNA) scaffold, Cas9 enzyme, and puromycin selection marker. gRNA sequences (**B, table**) targeting Exon 4 of the CL4 porcine CDHR2 genomic region were cloned into the lentiCRISPRv2 plasmid. An empty lentiCRISPRv2 plasmid, with no added gRNA but still containing Cas9 machinery, was used as the "Control". WT CL4 cells were transduced with CRISPR virus containing either of the two gRNA sequences and selected with puromycin. Single clones of selected cells were isolated and expanded into clonal "KO" populations. (**B**) Genomic DNA was extracted from the clones and PCR was used to generate a region spanning exons 4 and 5 of CDHR2. Trace files of each clone and the control cells were analyzed with the Synthego Inference of CRISPR Edits (ICE) tool (Conant et al., 2022). (**C**) W1 spinning disc confocal MaxIP images of Control, CDHR2 KO Clone "E9", and Clone "A11" stained for F-Actin (blue), CDHR2 (green), and CDHR5 (magenta). (**D**) Zooms from laser scanning confocal images of the same samples shown in (C) at a higher magnification showing the lack of microvillar clustering in KO clones. (**E**) Mean CDHR2 intensities of Control vs. CDHR2 KO clones. (**F**) Mean CDHR5 intensities of Control vs. CDHR2 KO clones. $n = 45$ total 60X imaged control fields and $n = 15$ 60X fields of each KO clone, total of $n = 45$ KO fields. Unpaired t-test; **** $p \leq 0.0001$. Error bars represent mean ± SD. Scale bars: 40 µm (C), 10 µm (D).

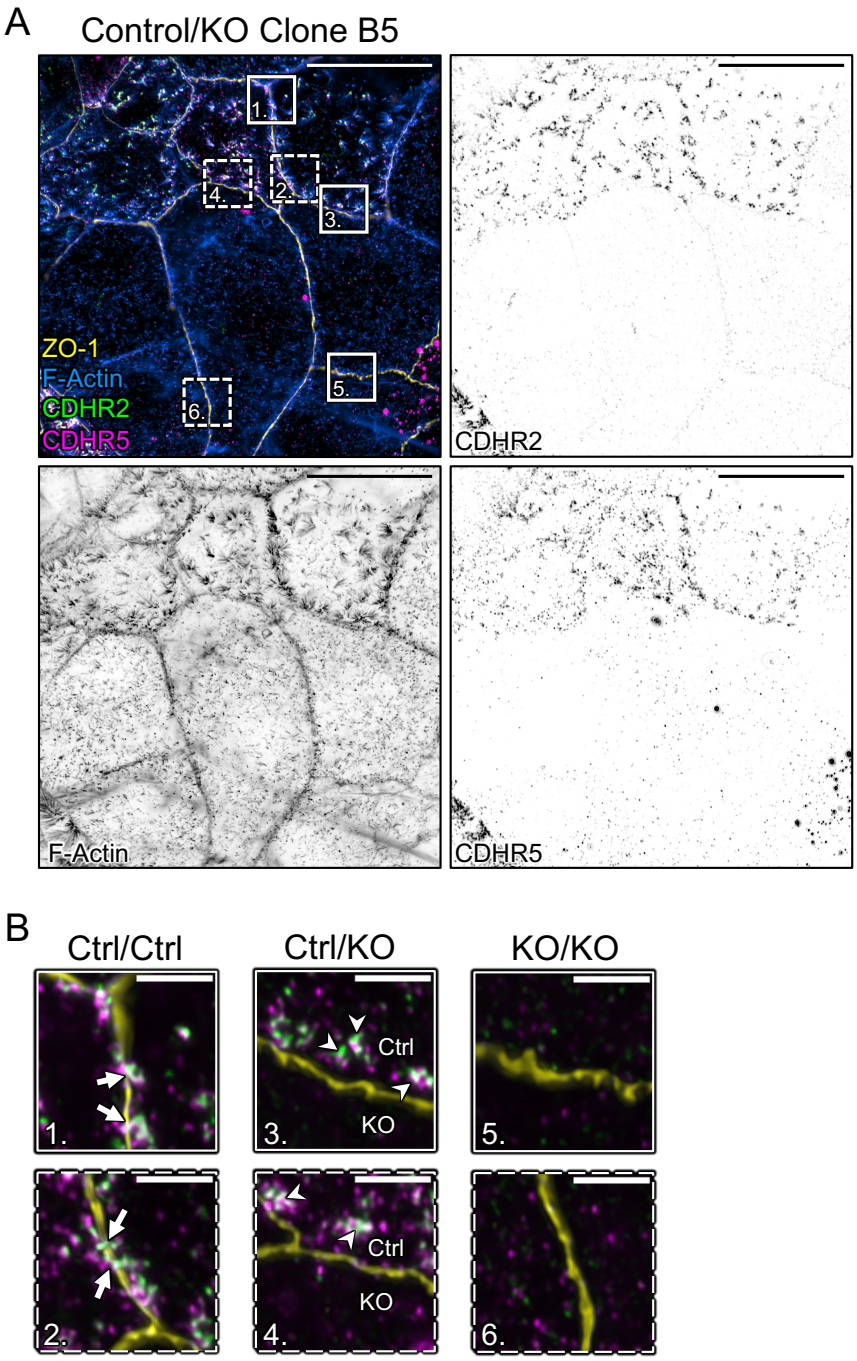

Figure 3-10. CDHR2 is required for transjunctional clustering of microvilli. (**A**) Laser scanning confocal MaxIP image of mixed cells stained for ZO-1 (yellow), CDHR2 (green), CDHR5 (magenta), and F-actin (blue). The solid and dashed boxes represent zooms, as numbered. (**B**) Control/Control (Ctrl/Ctrl) cell interfaces show clear clustering across ZO-1 marked junctions (zooms 1 and 2, white arrows) while Ctrl/KO interfaces demonstrate limited transjunctional clustering (zooms 3 and 4). Ctrl cells at Ctrl/KO interfaces still exhibit clustering (white arrowheads). KO/KO interfaces demonstrate little to no clustering at cell margins (zooms 5 and 6). Scale bars: 20 µm (A), 3 µm (B).

Protocadherins in transjunctional IMACs exhibit limited turnover

Under normal conditions, epithelial cells express both CDHR2 and CDHR5, which target to the tips of all microvilli across the apical surface. Thus, heterophilic complexes are expected to form between the distal tips of microvilli in both the medial and marginal regions. However, the strong alignment of microvilli at cell-cell contacts in the heterophilic case outlined above led us to predict that transjunctional IMACs may be more stable relative to complexes that form medially. If true, this would offer a mechanistic explanation for the reduced motility of marginal microvilli, and in turn, the accumulation of microvilli at these sites. To determine if transjunctional IMACs are in fact longer lived than medial complexes, we performed fluorescence recovery after photobleaching (FRAP) analysis with CL4 monolayers formed using the cell mixing approach outlined above (**Fig. 3-7A**). Strikingly, photobleached ROIs positioned over junctional interfaces between heterophilic CDHR2-EGFP and CDHR5-mCherry expressing cells demonstrated extremely low signal recovery for both protocadherins (immobile fractions, 0.71 and 0.85, respectively; **Figs. 3-11A,B**). In contrast, FRAP analysis of medially positioned ROIs on individual cells expressing both CDHR2-HALO and CDHR5-EGFP, revealed much lower immobile fractions for both protocadherins (0.47 and 0.56, respectively; **Figs. 3-11C,D**). These results suggest that transjunctional IMACs formed between marginal microvilli are much longer lived relative to complexes formed between the tips of medial microvilli. We also examined recovery in photobleached ROIs positioned over junctional interfaces formed between homophilic CDHR2-EGFP and CDHR2-mCherry expressing cells (**Figs. 3-11E,F**), as well as interfaces formed between homophilic CDHR5-EGFP and CDHR5-mCherry expressing cells (**Figs. 3-11G,H**). Both homophilic scenarios exhibited higher levels of turnover and even lower immobile fractions. Together, these FRAP studies indicate that transjunctional IMACs composed of CDHR2

and CDHR5 are extremely stable, and the reduced turnover kinetics offer an explanation for the constrained motility and accumulation of microvilli observed at cell margins.

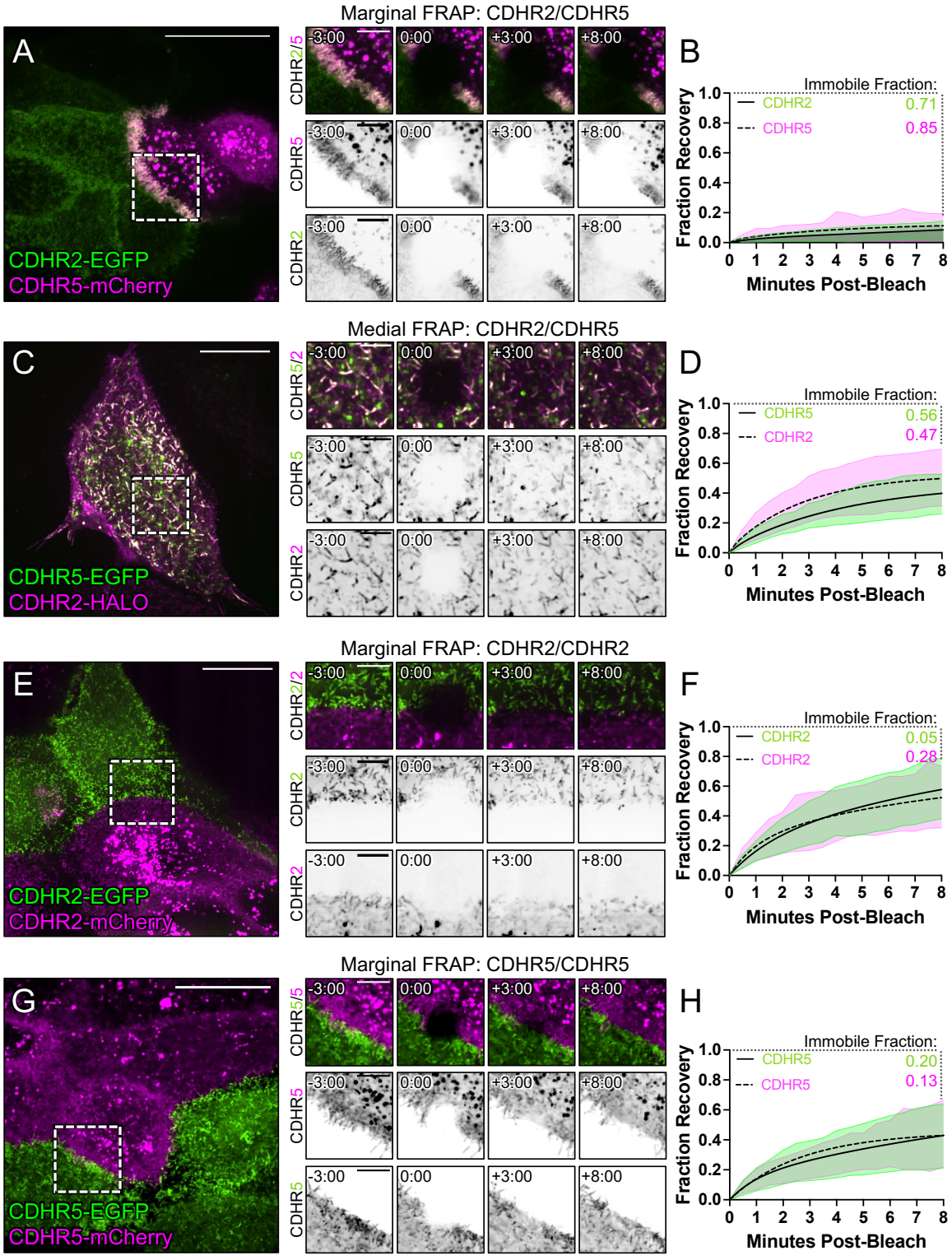

Figure 3-11. FRAP analysis suggests that heterophilic, transjunctional adhesion complexes are stable. Mixed CL4 cells forming (**A**) marginal heterophilic, (**C**) medial heterophilic, (**E**) marginal homophilic CDHR2, and (**G**) marginal homophilic CDHR5 adhesion complex interfaces. Dashed boxes outline the photobleached ROI shown in the recovery montages on right. (**B, D, F, H**) Fluorescence recovery is plotted over the course of 8 minutes with the immobile fractions as written for each protein channel. Immobile fractions were calculated from a two-phase association curve by subtracting the predicted plateau from 1 (100% fluorescence recovery). All plots represent 3 independent FRAP experiments of $n \geq 20$ ROIs from multiple cells. Scale bars: 20 μm (A, C, E, G), 5 μm (montages).

Myosin-2 dependent contractility stabilizes transjunctional clustering of microvilli

Why transjunctional IMACs exhibit longer lifetimes than medial IMACs remains unclear, but one possibility that is mechanical tension, which is high across cell junctions (Charras and Yap, 2018), but low elsewhere on the apical surface, plays a role in specifically stabilizing these transjunctional complexes. Indeed, previous biophysical studies revealed catch bond-like behavior in cadherin family proteins, where the application of tensile force increases the lifetime of the adhesive complex (Rakshit et al., 2012). Transjunctional tensile force has also been shown to promote the accumulation of junctional components, including E-cadherin, and driving the maturation of these contacts (Hoffman and Yap, 2015; Pinheiro and Bellaïche, 2018). To determine if tension applied across cell junctions promotes the adhesive clustering and accumulation of microvilli at these sites, we inhibited non-muscle myosin-2, which accumulates in sub-apical networks and generates these large-scale forces (Turner et al., 1997). For this experiment, we treated mCherry-ESPN expressing monolayers with blebbistatin and monitored marginal microvilli over 90 min using confocal microscopy. In alignment with previous studies that implicated myosin-2 in limiting microvillar core bundle length (Chinowsky et al., 2020; Meenderink et al., 2019), microvilli throughout the field elongated in response to blebbistatin compared to DMSO (**Fig. 3-12A-B and C-D**). However, myosin-2 inhibition also markedly reduced the alignment and accumulation of microvilli at cell margins (**Fig. 3-12C,F**). These findings are consistent with the idea that mechanical tension applied across cell junctions plays a role, either directly or indirectly, in elongating the lifetime of transjunctional IMACs.

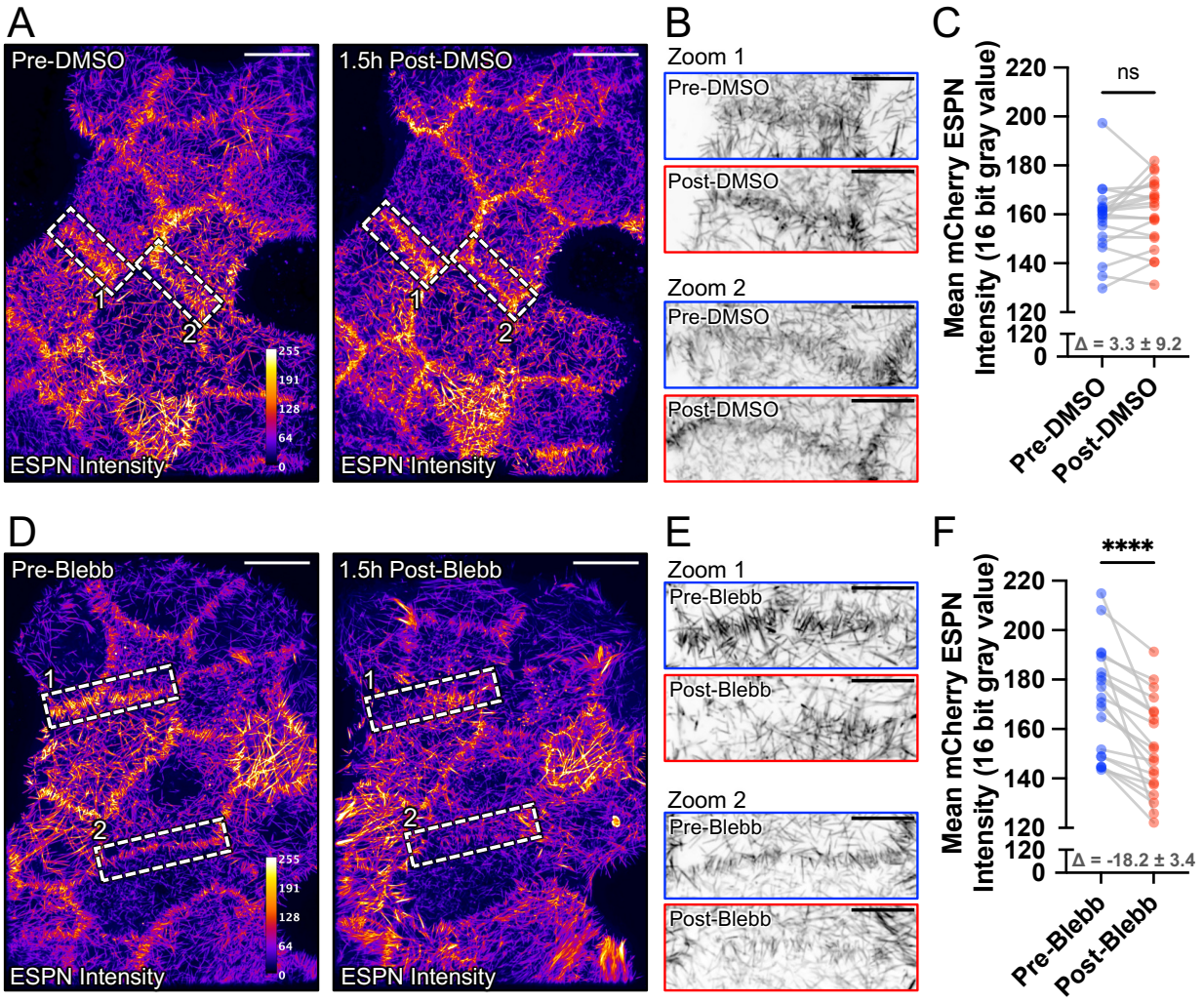

Figure 3-12. Myosin-2-dependent contractility stabilizes transjunctional clustering of microvilli. (**A**) Fire LUT intensity profile of the mCherry-ESPN channel Pre- and 1.5 hr Post-DMSO control treatment. (**B**) Zooms from the dashed boxes on (A) as marked showing inverted ESPN channel Pre- and 1.5 hr Post-DMSO. (**C**) Mean mCherry-ESPN intensities (16-bit gray values) of paired cell-cell interfaces Pre- and 1.5 hr Post-DMSO treatment; mean signal Δ = 3.3 ± 9.2. (**D**) Fire LUT intensity profile of the mCherry-ESPN channel Pre- and 1.5 hr Post-blebbistatin (20 µM) addition. (**E**) Zooms from the dashed boxes on (D) as marked showing inverted ESPN channel Pre- and 1.5 hr Post-blebbistatin. (**F**) Mean mCherry-ESPN intensities (16-bit gray values) of paired cell-cell interfaces Pre- and 1.5 hr Post-blebbistatin treatment; error bars represent mean ± SD; mean signal Δ = -18.2 ± 3.4. *n = 20* pairs of linescans drawn along cell-cell interfaces for each treatment; paired t-test non-significant (ns) and **** $p \leq 0.0001$. Scale bars: 20 µm (A,D), 10 µm (B,E).

Microvilli accumulation at cell margins precedes accumulation in the medial zone during differentiation

Based on the stabilizing nature of transjunctional IMACs, we predicted that during differentiation, cells might assemble the brush border by packing microvilli inward from cell margins. To test this idea, we performed extended time-lapse imaging of CL4 cells expressing mCherry-ESPN to stoichiometrically label microvillar core actin bundles (**Fig. 3-13A,B**) (Loomis et al., 2003). Comparing regional ESPN intensities on a per cell basis, we found that marginal ESPN intensity increased almost ~2-fold more than medial signal during 24 hrs of differentiation (**Fig. 3-13C**). These timelapse results are consistent with the idea that microvilli accumulate first at cell margins and then pack inwards from the edges of the cell over time as differentiation proceeds.

Discussion

Previous live imaging studies of epithelial cells at times points early in differentiation established that actively growing and newly formed microvilli are highly motile and unstable, undergoing rapid cycles of growth and collapse (Gaeta et al., 2021a; Meenderink et al., 2019). Those discoveries led us to question how dynamic, nascent microvilli are stabilized long-term to enable their timely accumulation in large numbers (i.e., thousands) by the end of differentiation. We approached this question by first examining the surface of the undifferentiated epithelial cells that line the interior of the intestinal crypt, where microvillar growth activity is high. Because the apical surface of cells in this region is not yet fully packed with protrusions, we were hoping to identify patterns in the distribution of nascent microvilli that might offer insight on underlying mechanisms of stability. Peering into the crypt is technically challenging given the tight confines of this invaginated compartment. Indeed, almost all previous ultrastructural studies of this region

have been limited to conventional transmission EM of ultrathin sections (Li et al., 2018; Trier, 1963), which are difficult to interpret in the absence of 3D context. We worked around this obstacle using a combination of tissue fracturing and scanning EM, which allowed us to visualize the apical surface of immature intestinal epithelial cells within the crypt. Inspection of these images revealed that microvilli preferentially accumulate near the cell periphery at this point in differentiation. Cell culture models from the intestine (CACO-2_{BBE}) and kidney (CL4) also demonstrated robust marginal accumulation of microvilli early in their maturation time course, suggesting that such patterning is not a function of the unique cellular packing geometry found in the crypt, nor is it tissue specific.

Accumulation at cell edges suggests that the marginal zone represents (i) a site of robust microvilli growth, (ii) a site of stabilization for nascent microvilli, or (iii) some combination of the two. Given the actin-rich junctional belt that surrounds the cell at the level of the terminal web (Wu et al., 2014), it seems reasonable to expect that microvilli may grow more readily in this location. Although previous live imaging studies of CL4 cells characterized the properties of individual microvillar growth events (Gaeta et al., 2021a), those observations were limited to the medial regions of the cell where protrusion density is typically low; visualization of growth events in the marginal zone was confounded by the crowding of pre-existing microvilli in this region. While our data do not allow us to rule out the possibility that growth preferentially occurs at cell margins relative to medial regions, we were able to capture clear examples of clustered microvilli moving at a low angle relative to the cell surface, toward the edge of the cell and incorporating into the marginal population. Interestingly, these protrusions adopt the more vertical orientation of marginal microvilli upon reaching the cell edge. Because such upright orientation is a defining feature of microvilli in mature brush borders, the marginal population likely represents stabilized

protrusions that persist into later stages of differentiation. Although we currently lack a method for tracking and measuring the lifetimes of individual microvilli over the course of days, our short-term tracking measurements using the tip marker, EPS8, confirm that marginal microvilli are less motile relative to medial microvilli, which is consistent with a physical capture mechanism near the cell edge.

Earlier work established that medial microvilli on the surface of mature villus enterocytes employ the protocadherins CDHR2 and CDHR5 to form intermicrovillar adhesion complexes (IMACs) that link the distal tips of neighboring microvilli (Crawley et al., 2014b; McConnell et al., 2011). Here we sought to test the possibility that IMACs form across cell junctions, between the protrusions that extend from neighboring cells. If so, this would offer a mechanistic explanation for the upright orientation and constrained motility that microvilli demonstrate at these sites, and potentially the long-term stabilization that enables microvillar accumulation on the apical surface in large numbers. Previous work in CACO-2_{BBE} cells, native mouse intestinal tissue, and X-ray crystallography all indicate that the interacting ectodomains of CDHR2 and CDHR5 are structurally capable of spanning gaps up to 63 nm wide (Crawley et al., 2014b; Gray et al., 2021), suggesting that they could easily reach across the ~15 nm tight junction between neighboring cells (Vanslembrouck et al., 2022). Indeed, in the current study, super-resolution imaging revealed that CDHR2 and CDHR5 span the intercellular space to form *transjunctional IMACs* that physically link marginal microvilli that extend from neighboring cells.

Does the formation of transjunctional IMACs explain the accumulation of microvilli at cell edges early in differentiation? Our mixed monolayer experiments with CL4 cells lacking CDHR2 or overexpressing tagged forms of CDHR2 and CDHR5, indicate that IMAC protocadherins are necessary and sufficient for the marginal accumulation of microvilli. Further, if transjunctional

IMACs are more stable and exhibit longer lifetimes relative to IMACs that form medially, this would certainly offer a mechanistic underpinning for the increase in microvilli density at these sites. To test this hypothesis, we used the cell mixing approach to induce the formation of both homophilic and heterophilic transjunctional IMACs, to enable further characterization of their properties. FRAP analysis of the turnover dynamics of these complexes revealed that heterophilic (CDHR2/CDHR5) transjunctional IMACs are much longer lived relative to homophilic (CDHR2/CDHR2) complexes. These results from live epithelial cells echo previous *in vitro* data suggesting that homophilic (CDHR2/CDHR2) complexes are much weaker than heterophilic (CDHR2/CDHR5) complexes (Crawley et al., 2014b). Interestingly, when we examined the dynamics of heterophilic complexes formed between microvilli in the medial population, we noted that these also turned over at a much higher rate relative to transjunctional heterophilic (CDHR2/CDHR5) complexes. Thus, the differential stability of transjunctional vs. medial IMACs indicated by our FRAP studies offers a mechanistic rationale for the accumulation of microvilli at cell margins.

Why are transjunctional IMACs more stable than those formed elsewhere on the apical surface? One possibility is that tensile forces, which are expected to be much higher across cell junctions relative to more medial regions of the cell surface (Charras and Yap, 2018), exert a stabilizing effect on transjunctional CDHR2/CDHR5 adhesion. Indeed, transjunctional tension is known to drive the accumulation of junctional components including E-cadherin (Kale et al., 2018) and F-actin (Leerberg et al., 2014). Consistent with these ideas, we found that an inhibitor of myosin-2 contractility, blebbistatin, significantly reduced the accumulation of marginal microvilli in CL4 monolayers. A potential mechanism to explain such mechano-sensitivity in IMAC protocadherins is found in the biophysical literature on non-covalent bonds. When a tensile

mechanical force is applied across a non-covalent bond formed between two proteins, the lifetime of that bond will be impacted in a way that depends on the structural nature of the bonding interface (Sokurenko et al., 2008; Thomas, 2006). “Slip bonds” react to increased loading with a dramatic shortening of bond lifetime, whereas “catch bonds” respond by increasing bond lifetime; “ideal bonds” exhibit minimal response to mechanical loading (Rakshit et al., 2012; Sokurenko et al., 2008; Thomas, 2008). Direct physical measurements provide strong evidence for catch bond behavior in structurally diverse proteins, ranging from myosin motor domains to cell surface molecules such as integrins (Guo and Guilford, 2006; Kong et al., 2009). Cadherins have been studied extensively in this regard and their bonding properties are complex. In the case of E-cadherin, adhesive interactions can exhibit slip *or* catch behavior depending on the conformation of the adhesive interface. In the canonical strand swapped conformation, E-cadherin exhibits slip bond behavior; while X-dimers of E-cadherin, which interact using a distinct extended structural interface demonstrate robust catch bond behavior (Rakshit et al., 2012). In light of those findings, we speculate that IMACs might also exhibit catch bond properties. By bridging across cell junctions, transjunctional IMACs may be subject to higher tensile loads and exhibit increased adhesive lifetimes relative to IMACs that form elsewhere on the apical surface. Although rigorous testing of this concept awaits future biophysical studies, it is important to note that, based on the recently solved structures of mouse and human CDHR2 and CDHR5 ectodomains (Gray et al., 2021), any catch bond behavior in the IMAC would emerge from a mechanism that is distinct from E-cadherin.

Given the adhesive capture of microvilli by stable transjunctional IMACs and our observations of marginal microvilli enrichment early in differentiation, we speculated that microvilli may pack from the margins of the apical surface inward during brush border assembly.

To test this idea, we turned to multi-day time-lapse imaging of CL4 cells expressing mCherry-ESPN as a marker for microvilli. As expected, we noted that the marginal ESPN intensity was initially higher than in the medial region. After 24 hours of differentiation, the marginal region also demonstrated ~2-fold larger increase in signal relative to the medial zone, suggesting that microvillar packing density at the cell margin precedes packing of the interior apical surface (**Fig. 3-13D**). Moreover, intensity at the cell margin is consistently higher than medial signal, while both regions increase in intensity over the course of almost two days of imaging.

While previous work established that the IMAC is critical for maintaining brush border structure on mature enterocytes (Pinette et al., 2019), the current study highlights a role for this complex in apical surface maturation, by driving interactions between microvilli of neighboring cells. In the intestinal tract and other transporting epithelial tissue, cell-cell contacts are essential for barrier function and the maintenance of physical compartmentalization. Interestingly, Crohn's disease patients exhibit a decrease in CDHR2 and CDHR5 mRNA expression (VanDussen et al., 2018) while also experiencing increased intestinal permeability (McGuckin et al., 2009). Transjunctional adhesion complexes may also form an additional layer of protection against colonizing pathogens. Infection by related pathogens Enteropathogenic and Enterohemorrhagic *Escherichia coli* (EPEC and EHEC) is characterized by effacement of brush border microvilli and F-actin pedestal formation (Velle and Campellone, 2017). CDHR2 has been identified as one of the initial EHEC targets during infection, which results in a significant decrease in CDHR2 expression (In et al., 2016). Past reports on EPEC infection also show bacterial localization over cell junctions (Pedersen et al., 2017; Velle and Campellone, 2017). Exploring roles for transjunctional IMACs in maintaining epithelial barrier function in intestinal disease and infection should be a central goal of future studies.

CHAPTER IV

LOSS OF APICAL INTERMICROVILLAR ADHESION IMPACTS BASOLATERAL JUNCTION COMPONENTS AND FUNCTION

This chapter will be edited, formatted, and submitted as a first-author research article for peer-review.

Introduction

Cellular junctions are an integral building block of epithelial tissues, forming physical connections with neighboring cells to provide structural support and highly selective paracellular diffusion. Transporting epithelia found in the small intestine and kidney proximal tubule are two examples of tissues that rely heavily on strong intercellular barriers to separate them from the external environment (Garcia-Castillo et al., 2017). Made up of a vertical stack of interacting proteins, the junction has been classically described to contain, from apical to basal, the tight junction, the adherens junction, desmosomes, gap junctions, and hemidesmosomes (Garcia et al., 2018). Within the tight junction, transmembrane proteins including junctional adhesion molecule (JAM), occludins, claudins and intracellular scaffolding zonula occludens proteins create an intricate strand-like structure (Van Itallie and Anderson, 2014). Coupled to this region are actin and non-muscle myosin 2, providing peripheral support to the tight junction (Baranwal et al., 2012; Hull and Staehelin, 1979; Liu and Cheney, 2012). While the proteins within this region have been well-established for decades, new roles and localizations of these components are still being discovered. For example, polarity proteins were recently localized along the length of apical actin-based microvilli in addition to the tight junction (Mangeol et al., 2022). Furthermore, non-muscle myosin-2c (NM2C), which was previously thought to localize strictly to the apical junction, also

exists in a medial, subapical array across the entire cell surface. As a myosin motor protein, NM2C generates tensile force at cell junctions, but also controls microvillar length by regulating actin filament pointed end disassembly (Chinowsky et al., 2020; Ebrahim et al., 2013).

Force is also key to supporting the more basolateral adherens junctions. This region contains, most notably, E-cadherin – a transmembrane adhesion protein that extends its extracellular domain to a neighboring cell, forming strong cell-cell contacts (Pinheiro and Bellaiche, 2018). An intestinal E-cadherin knockout (KO) mouse demonstrated that it also influences intestinal morphogenesis and barrier function (Bondow et al., 2012). β-catenin is another component of the adherens junction, binding to E-cadherin and forming a fundamental connection to the actin cytoskeleton (Tian et al., 2011; Valenta et al., 2012). Moreover, the interplay of β-catenin and E-cadherin controls epithelial cell contacts and loss of E-cadherin releases β-catenin from adherens junctions, activating the Wnt-signaling pathway and promoting downstream cell migration – an effect seen in cancer progression (Tian et al., 2011; Yap, 1998).

Recently, we identified another cadherin complex, but at the apical surface of transporting epithelial cells. Made up of protocadherins CDHR2 and CDHR5, this complex connects neighboring cell microvilli together across cellular junctions in a transjunctional intermicrovillar adhesion complex (IMAC). Additionally, this complex is required for microvilli clustering and brush border packing *in vitro* and *in vivo* (Cencer et al., 2023; Crawley et al., 2014b; Pinette et al., 2019). Fascinatingly, further investigation into CDHR2 KO mouse and cell culture models now suggests that basolateral junctions are impacted by transjunctional IMACs, hinting that the IMAC could serve as an additional layer to the classic junction model.

Here, we report that CDHR2 KO in kidney proximal tubule and intestinal cells and mouse small intestine leads to a loss of basolateral junction proteins claudin-7, ZO-1, E-cadherin, β-

catenin, and epithelial cell adhesion molecule (EpCAM). Furthermore, CDHR2 KO cell junctions exhibit a loss of straightness matched by a decrease in junctional and whole cell NM2C, most likely due to a tension deficit. Lastly, the functionality of CDHR2 KO cell junctions is impaired, as represented by decreased transepithelial electrical resistance and reduced wound healing. Overall, this suggests that apical transjunctional IMACs may play a role in basolateral junction stability, integrity, and function.

Results

Loss of CDHR2 disrupts microvillar clustering and cell morphology:

The formation of higher order microvilli clusters is a key step in the brush border differentiation process (Meenderink et al., 2019). Previous evidence implicated the apical cadherin protein CDHR2 to be important for microvillar clustering and organization (Crawley et al., 2014b; Pinette et al., 2019). More recently we discovered that CDHR2-based IMACs accumulate at the margins of differentiating LLC-PK1-CL4 (CL4) kidney proximal tubule cells. Notably, the deletion of CDHR2 in a CRISPR-driven KO CL4 model led to the loss of microvillar clustering and decreased marginal accumulation (Cencer et al., 2023). To further characterize the impact of CDHR2 KO in a system amenable to live imaging, we recapitulated this model in CACO-2_{BBE} (CACO) cells with a similar strategy, targeting the exon coding the first EC domain which is necessary for adhesion complex formation (**Fig. 4-1A**) (Crawley et al., 2014b; Gray et al., 2021). A comparable phenotype was observed, with a lack of microvilli clusters even at a time point later in differentiation, 12 days post confluency (DPC) (**Fig. 4-1B**). Like our observations with CDHR2 KO in CL4 cells, levels of CDHR5 were also decreased in CACO cells grown to 12 DPC (**Fig. 4-1C**), a consequence consistent with other IMAC knockdown or KO models (Choi et al., 2020; Crawley et al., 2016; Li et al., 2017; Pinette et al., 2019; Weck et al., 2016).

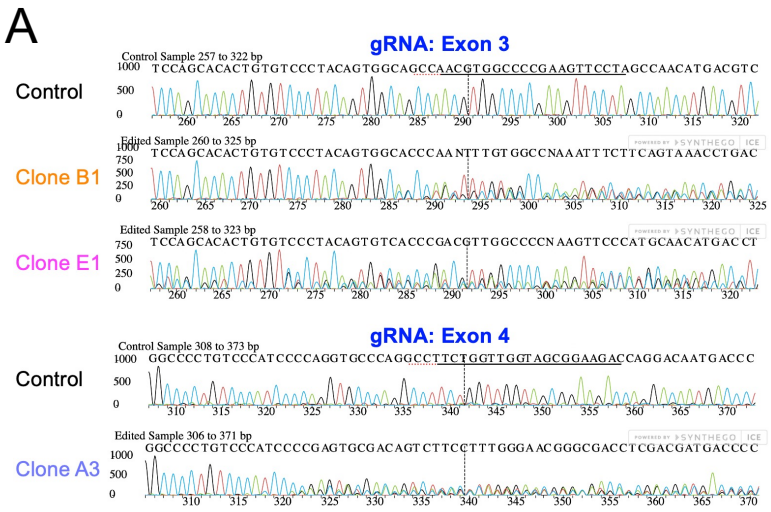

KO Clone	gRNA sequence	PAM	INDEL %	MODEL FIT (R^2)	KNOCKOUT-SCORE
B1	TAGGAACTTCGGGGCCACGT	TGG	91	0.91	31
E1	TAGGAACTTCGGGGCCACGT	TGG	85	0.85	85
A3	GTCTTCCGCTACCAACCAGA	AGG	93	0.93	93

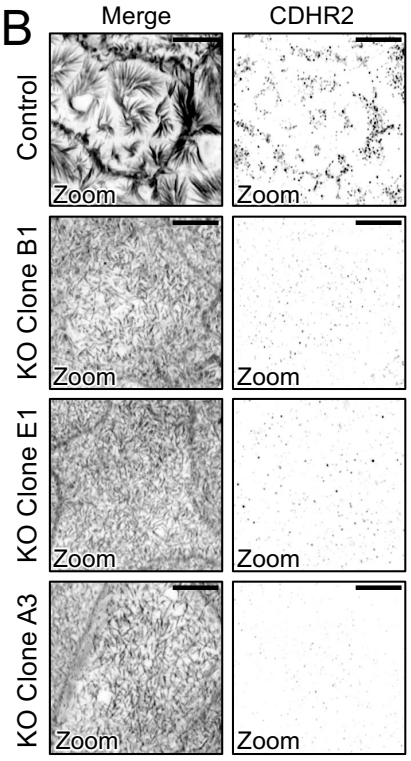

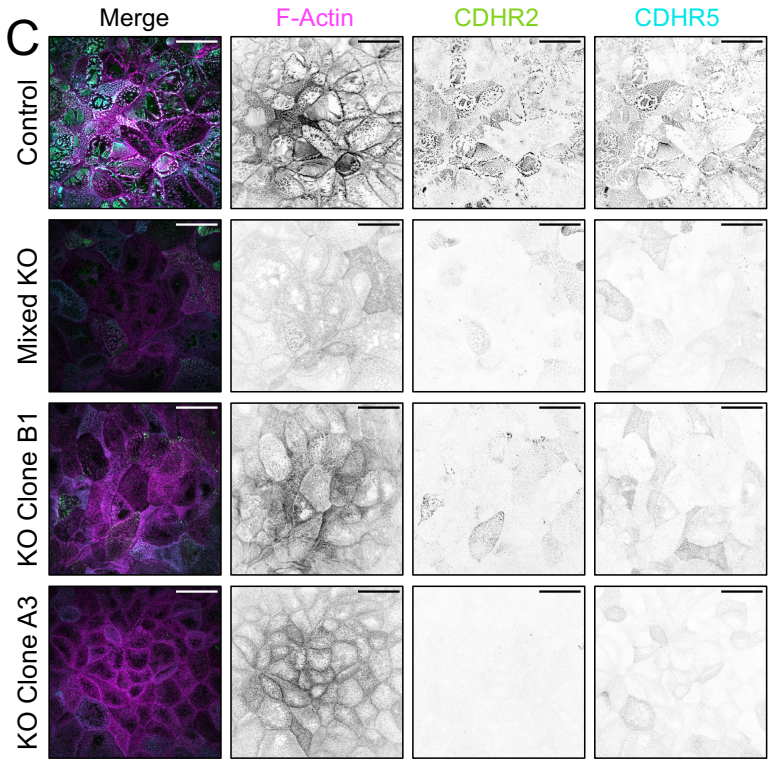

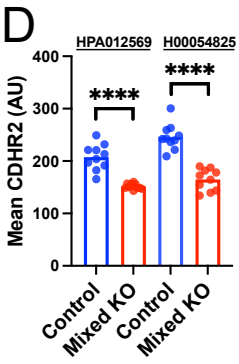

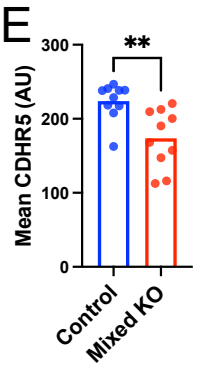

Figure 4-1. Generation and validation of CDHR2 KO CACO-2$_{BBE}$ cells. (**A**) Genomic DNA was extracted from selected KO clones and PCR was used to generate two regions spanning exons 3 and 4 of CDHR2. Trace files of each clone and the control cells were analyzed with the Synthego Inference of CRISPR Edits (ICE) tool (Conant et al., 2022). (**B**) Control, CDHR2 KO Clone "B1", "E1" and "A3" stained for F-Actin and CDHR2 showing lack of microvillar clustering in the KO. (**C**) Control, mixed KO (pre-clonal selection), and KO clones stained for F-Actin (magenta), CDHR2 (green), and CDHR5 (cyan). (**D**) Mean CDHR2 intensities of Control vs. CDHR2 KO clones from two different CDHR2 antibodies, as marked. (**E**) Mean CDHR5 intensities of Control vs. CDHR2 KO clones. *n = 30* total 60X imaged control fields and *n = 10* 60X fields of the mixed KO cells, total of *n = 30* KO fields. Unpaired t-test; **** $p \leq 0.0001$, **p = 0.0032. Error bars represent mean ± SD. Matched imaging parameters and LUTs. Scale bars: 5 μm (B), 40 μm (D).

Another discernible phenotype of CDHR2 KO CL4 and CACO cells was abnormal cell and junction morphology. CL4 cells had elongated cell shapes with larger areas, as measured, and a significant decrease in ZO-1 signal (**Fig. 4-2A-C and Fig. 4-3B-C)**. Importantly, both ZO-1 and CDHR5 signal were partially rescued upon exogenous stable expression of CDHR2-HALO protein in CL4 cells (**Fig. 4-3)**. Deformed cell junctions were also observed in CACO CDHR2 KO cells, but with dramatic ruffled appearances (**Fig. 4-2D, Zoom)**. Junctional straightness measurements, with 1 being a perfectly straight line, revealed that KO junctions were less structured, with a mean straightness of 0.70 ± 0.13 compared to control junctions of 0.93 ± 0.03 (**Fig. 4-2E**).

Ruffled junctions are believed to be a consequence of a loss of junction scaffolding to the actin cytoskeleton and have been observed in ZO-1 protein perturbation studies (Fanning et al., 2002; Lynn et al., 2020; Tokuda et al., 2014). Given that CDHR2 KO cells have a significant lack of ZO-1 signal (**Fig. 4-2H and 4-3C**), this may be one explanation for the cell shape deformities. Additionally, ruffles and increased cell area could also be a result of junctional tension defects, in which a loss of tension causes junctions to collapse and cells to spread (Diz-Munoz et al., 2013; Sumi et al., 2018). As a key component of intestinal epithelial cells, non-muscle myosin-2 (NM2) is a candidate for generating tension in our CACO-2$_{BBE}$ cell culture model (Chinowsky et al., 2020; Ebrahim et al., 2013). Indeed, staining for the isoform NM2C revealed that CDHR2 KO CACO

cells have a significant loss of signal (**Fig. 4-2F-G**), suggesting that a lack of force generation and tension in combination with decreased ZO-1 scaffolding to F-actin is contributing to ruffle formation. We hypothesize that these two ideas may be a united consequence of the loss of stabilizing transjunctional CDHR2/CDHR5 adhesion complex situated above the junctions.

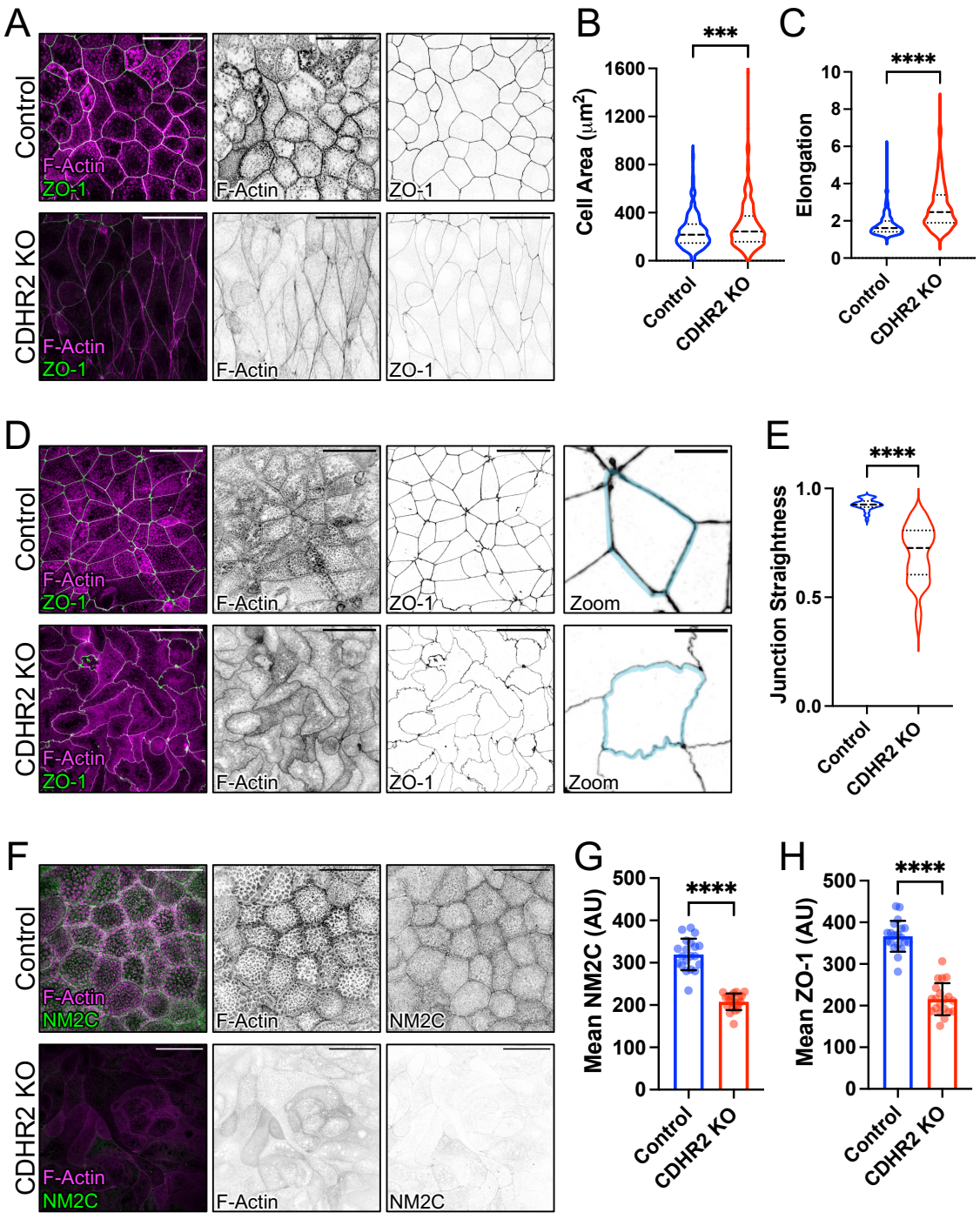

Figure 4-2. CDHR2 KO cells exhibit aberrant cell morphologies and decreased apical junction markers. (**A**) 3 DPC Control and CDHR2 KO CL4 cells stained for F-actin (magenta) and ZO-1 (green). (**B**) Measured cell area from n = 384 control cells and n = 259 KO cells. (**C**) Cell elongation measured as the ratio of max feret length to min feret length from the cells in (B). (**D**) 12 DPC Control and CDHR2 KO CACO cells stained for F-actin (magenta) and ZO-1 (green). Zooms show straight vs ruffled junctions in control and KO, respectfully. (**E**) Measured junction straightness (see methods) from n = 62 control and KO cell junctional segments where 1.0 is the most straight. (**F**) 21 DPC Control and CDHR2 KO CACO cells stained for F-actin (magenta) and NM2C (green). (**G**) Measured mean CACO NM2C and (**H**) ZO-1 intensities from n = 30 60X fields per condition. Unpaired t-tests; ***p = 0.003, ****p<0.005. Error bars represent mean ± SD. Matched imaging parameters and LUTs. Scale bars: 40 µm (A,D,F), 10 µm (D, Zooms).

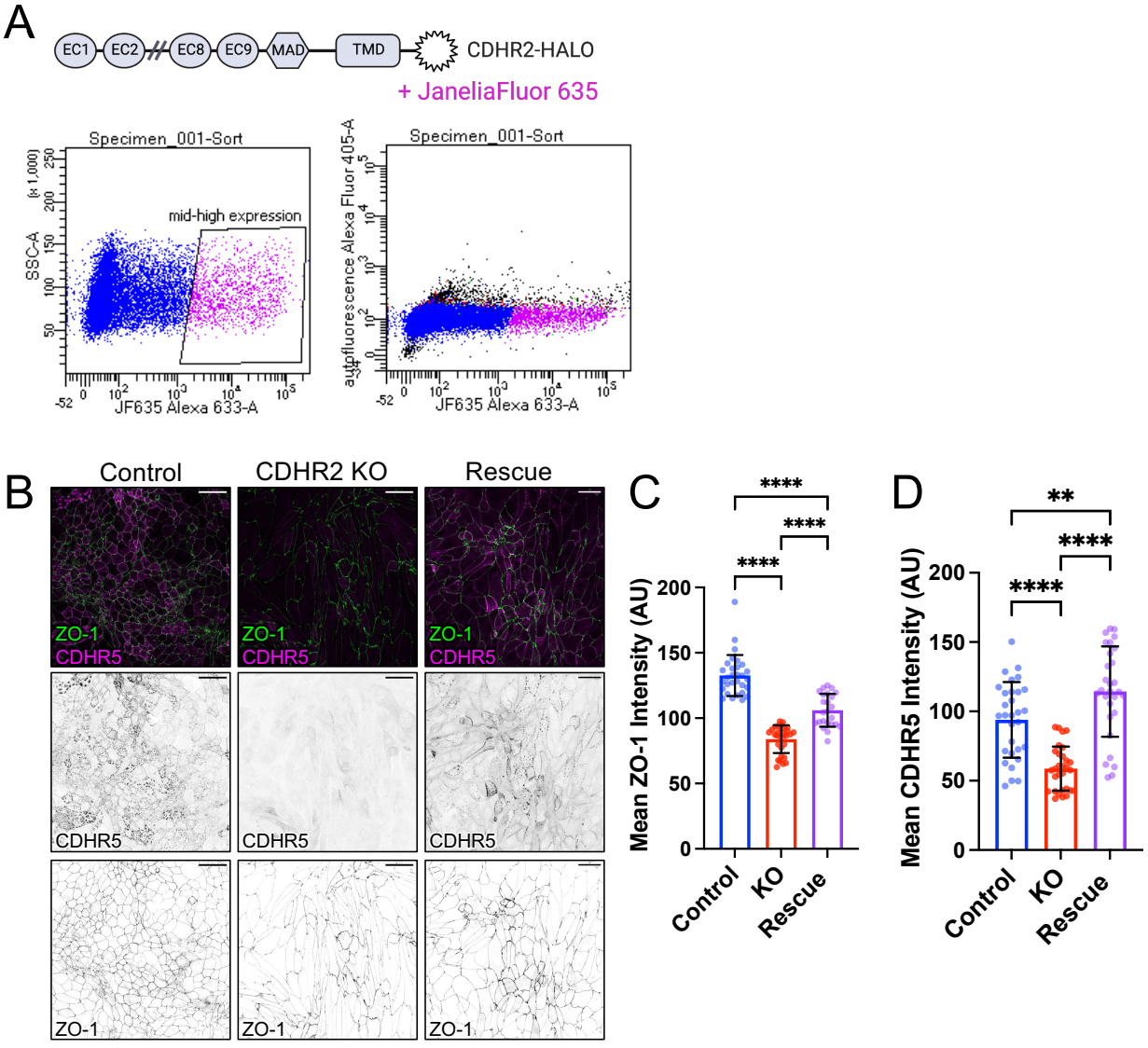

Figure 4-3. CDHR2-HALO expression rescues levels of CDHR5 and ZO-1 in CHDR2 KO CL4 cells. (**A**) Diagram of the C- tagged CDHR2-HALO construct. "Rescue" cells were transfected, stably selected for CDHR2-HALO and isolated via FACS using ligand JF635. (**B**) Scanning laser confocal MaxIPs of 3 DPC Control, CDHR2 KO, and CDHR2-HALO rescue CL4 cells stained for ZO-1 (green) and CDHR5 (magenta). (**C**) Mean CDHR5 and (**D**) mean ZO-1 intensities for the three cell conditions. *n = 30* imaged 40X fields per condition from 3 independent staining experiments. **p = 0.0095, ****p ≤ 0.0001 Ordinary one-way ANOVA with post-hoc multiple comparisons test. Error bars represent mean ± SD. Matched imaging parameters and LUTs. Scale bars: 40 μm.

Junction proteins are depleted in CDHR2 KO cells

While force transmission can be attributed to tight junctions, adherens junctions are considered the central regulators of tension sensing in epithelia (Pinheiro and Bellaïche, 2018). For example, E-cadherin cell-cell contacts are strengthened under tension because of extracellular domain conformational changes acting as catch bonds (Rakshit et al., 2012). Further studies on this phenomenon showed tension stabilizes the E-cadherin/β-catenin bond and interaction with F-actin (Buckley et al., 2014). Relatedly, we found a significant decrease of E-cadherin and β-catenin when staining the CDHR2 KO CACO cells (**Fig. 4-4 A-B, E-F**). Other basolateral junction proteins including claudin-7 and EpCAM were also depleted in CDHR2 KO CACO cells (**Fig. 4-4 C-D, G-H**). Moreover, CDHR2 KO CL4 cells also have decreased E-cadherin and EpCAM signal (**Fig. 4-5**).

As direct binding partners, claudin-7 and EpCAM contribute to tight junction barrier maintenance through damage-induced cleavage of EpCAM and release of claudin-7 (Higashi et al., 2023; Ladwein et al., 2005; Wu et al., 2013). Likewise, decreased EpCAM leads to downstream loss of claudin-7 due to its failure to recruit claudin to the tight junction (Lei et al., 2012). In the present study, however, we speculate that there is also a decrease in conventional junction components due to loss of transcellular apical adhesion complexes, leading to destabilization of the neighboring cell junctions that they span.

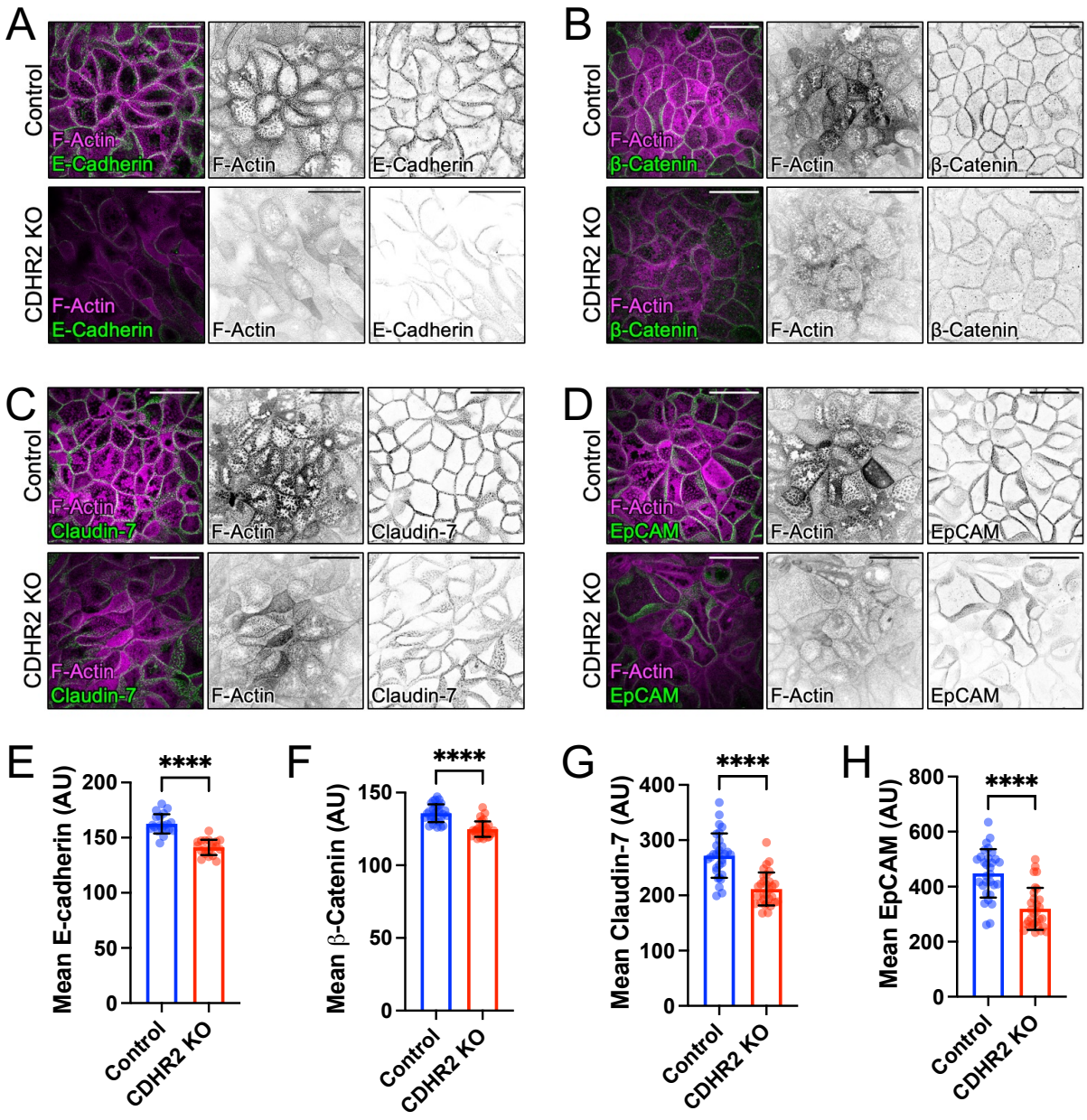

Figure 4-4. CDHR2 KO CACO cells have decreased junction protein signal.
12 DPC Control and CDHR2 KO CACO cells stained for (**A**) F-actin (magenta) and E-cadherin (green), (**B**) F-actin (magenta) and β-catenin (green), (**C**) F-actin (magenta) and Claudin-7 (green), (**D**) F-actin (magenta) and EpCAM (green). (**E-H**) Measured mean intensities from *n = 30* 60X fields per condition (Control and CDHR2 KO). Unpaired t-tests; ****p<0.005. Error bars represent mean ± SD. Matched imaging parameters and LUTs. Scale bars: 40 µm.

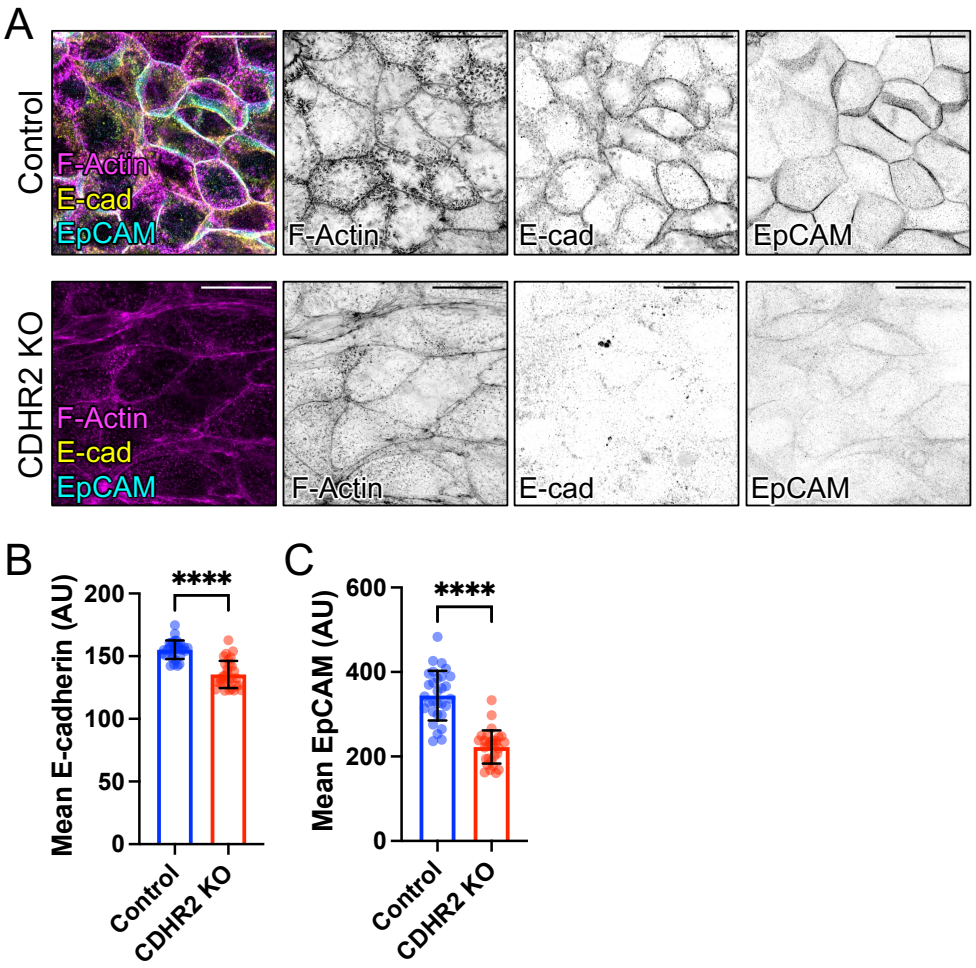

Figure 4-5. CDHR2 KO CL4 cells have decreased junction protein signal. (**A**) 3 DPC Control and CDHR2 KO CL4 cells stained for F-actin (magenta), E-cadherin (yellow), and EpCAM (cyan). (**B**) Measured mean E-cadherin and (**C**) EpCAM intensities from *n = 30* 60X fields per condition. Unpaired t-tests; ****p<0.005. Error bars represent mean ± SD. Matched imaging parameters and LUTs. Scale bars: 20 µm.

CDHR2 KO cells have decreased TEER and impaired wound healing function:

We next examined junction integrity and function in CDHR2 KO cells. Trans-epithelial electrical resistance (TEER) measurements are an established way to quantitatively represent tight junction barrier integrity (Srinivasan et al., 2015). Control and KO CACO cells were seeded on semipermeable Transwell filters and TEER was measured starting one day post-plating (**Fig. 4-6A**). Following TEER progression over the course of 22 days of differentiation revealed that

despite beginning with similar values, KO cells maintain a lower resistance number compared to Control cells with 22 DPC averages of 152.1 ± 12.2 Ω·cm^2 (KO clones) vs 342.6 ± 20.8 Ω·cm^2 (Control) (**Fig. 4-6A-B**). This control value falls within reported ranges in the literature for CACO-2 cell TEER, while the significantly lower KO value is indicative of disrupted junctions (Narai et al., 1997; Srinivasan et al., 2015).

As another readout for monolayer integrity, we first incited a wound through a scratch assay in CACO cell monolayers. Imaging over 20 hours revealed that CDHR2 KO CACO cells fail to close the wound and have lower velocity than Control cells (0.69 ± 0.17 μm/min and 0.37 ± 0.05 μm/min, respectfully) (**Fig. 4-6C-D**). Interestingly, an early study on CDHR2 showed that its expression in colon cancer cells increased cell motility, speeding up wound healing which supports our observed velocity defect in KO cells (Ose et al., 2009). We also examined the interplay of Control and KO CL4 cells by seeding them in separate chambers of a removeable Ibidi insert and labeling the membrane with the CellBrite Steady 650 membrane dye. Strikingly, Control cells exhibit progressive collective migration towards the gap while KO cells experience little movement with mean velocities of 0.31 ± 0.06 μm/min and 0.05 ± 0.03 μm/min, respectfully (**Fig. 4-6E-F**). KO cells, however, do show extensive movement within their own monolayer, suggesting that cell polarity may be disrupted in the absence of CDHR2. Newer research provides one explanation for this phenotype, showing that ZO-1 is required for coherent migration (Skamrahl et al., 2021). Furthermore, this study finds that cellular crowding in ZO1/2 KD cells leads to cellular jamming, creating two populations of cells: small cells with bulging apical membrane and large, stretched cells. We observed both populations in the CDHR2 KO CL4 cells with the membrane marker (**Fig. 4-6E**).

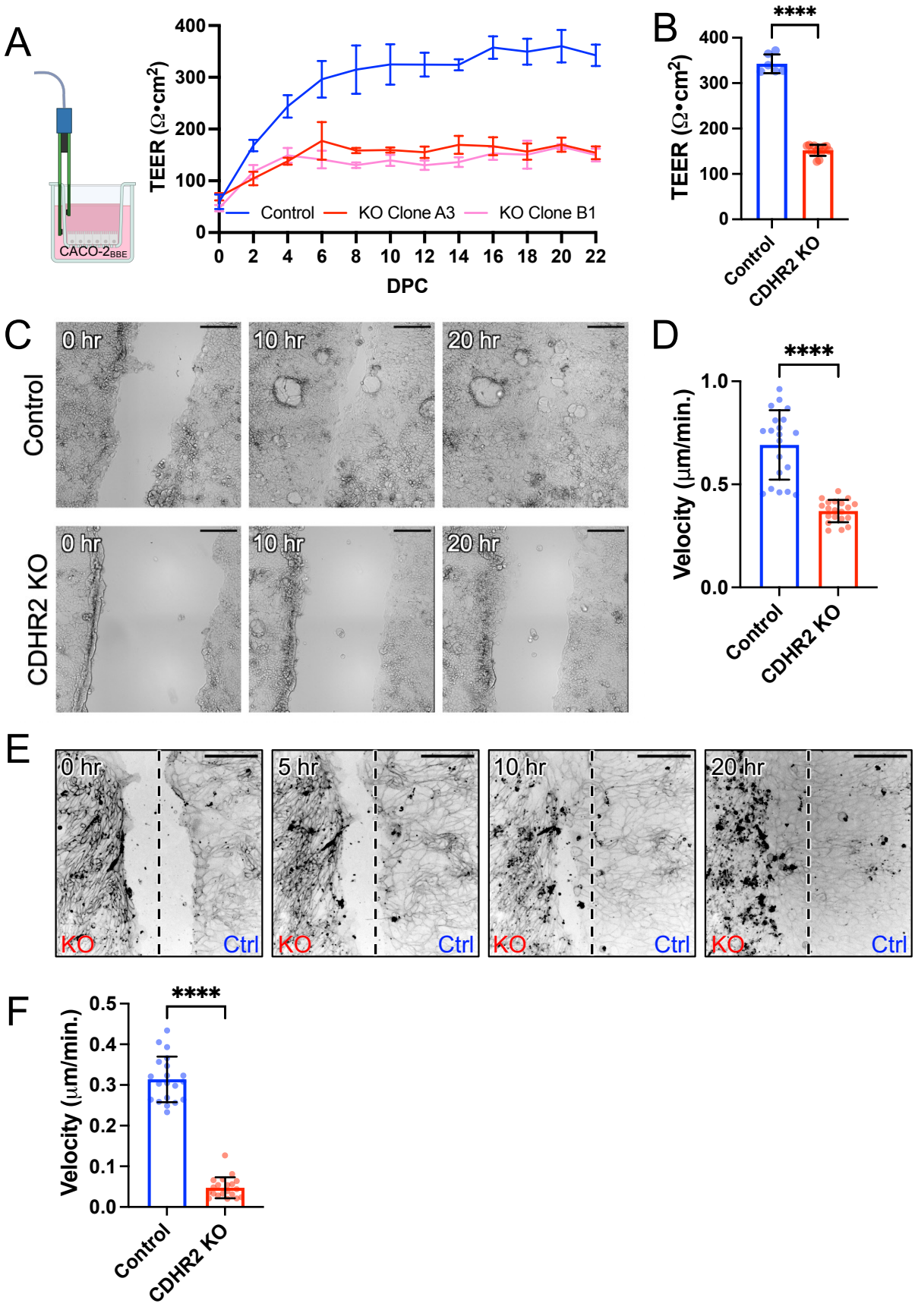
A
CACO-2BBE
TEER (Ω•cm²)
400
300
200
100
0
0 2 4 6 8 10 12 14 16 18 20 22
DPC
Control
KO Clone A3
KO Clone B1
B
****
TEER (Ω•cm²)
Control
CDHR2 KO
C
Control
CDHR2 KO
0 hr
10 hr
20 hr
D
****
Velocity (μm/min.)
1.0
0.5
0.0
Control
CDHR2 KO
E
0 hr
5 hr
10 hr
20 hr
KO
Ctrl
F
****
Velocity (μm/min.)
0.5
0.4
0.3
0.2
0.1
0.0
Control
CDHR2 KO

Figure 4-6. CDHR2 KO cells have impaired wound healing and decreased TEER. (**A**) CACO cells were seeded on Transwell inserts and transepithelial electrical resistance (TEER) measurements were measured every other day post-seeding to 22 DPC. (**B**) Mean TEER values from *n = 6* Control and *n = 12* (6 per KO clone) Transwells at 22 DPC: 342.6 ± 20.8 $\Omega \cdot cm^2$ (Control) vs 152.1 ± 12.2 $\Omega \cdot cm^2$ (KO clones). (**C**) Scratch assay monitoring wound recovery over 20 hours in Control vs CDHR2 KO CACO cells. (**D**) Velocities of *n = 20* Control and KO CL4 cell traces from the movies in (C) with mean velocities of 0.69 ± 0.17 μm/min (Control) and 0.37 ± 0.05 μm/min (KO). (**E**) Mixed Ibidi chamber cell migration assay with CDHR2 KO (left) and Control CL4 cells (right) +CellBrite650 membrane marker over 20 hours. (**F**) Velocities of *n = 20* Control and KO CL4 cell traces from the movie in (E) with mean velocities of 0.31 ± 0.06 μm/min (Control) and 0.05 ± 0.03 μm/min (KO). Unpaired t-tests; ****p<0.005. Error bars represent mean ± SD. Scale bars: 500 μm (C); 200 μm (E).

The CDHR2 KO mouse has impaired tight junction protein levels

Previous characterization of the intestinal (Villin-Cre) CDHR2 KO mouse focused on apical abnormalities and showed that villus and microvillus structure, IMAC proteins, and apical transporters were all altered in the absence of CDHR2-driven adhesion (Pinette et al., 2019). In revisiting this KO mouse model in the context of this study, we discovered that junctional proteins are also affected. Paraffin section staining of mouse duodenum demonstrates a marked loss of ZO-1 protein signal from tight junctions in addition to decreased villin intensity, a key actin bundling protein found within microvilli actin cores (**Fig. 4-7**) (Bretscher and Weber, 1979). Furthermore, preliminary staining of other junctional markers including E-cadherin, claudin-7, EpCAM, and NM2C indicates similar intensity deficits (**Fig. 4-8**). Overall, these *in vivo* results further support that loss of transjunctional adhesion leads to the disruption of basolateral junctions.

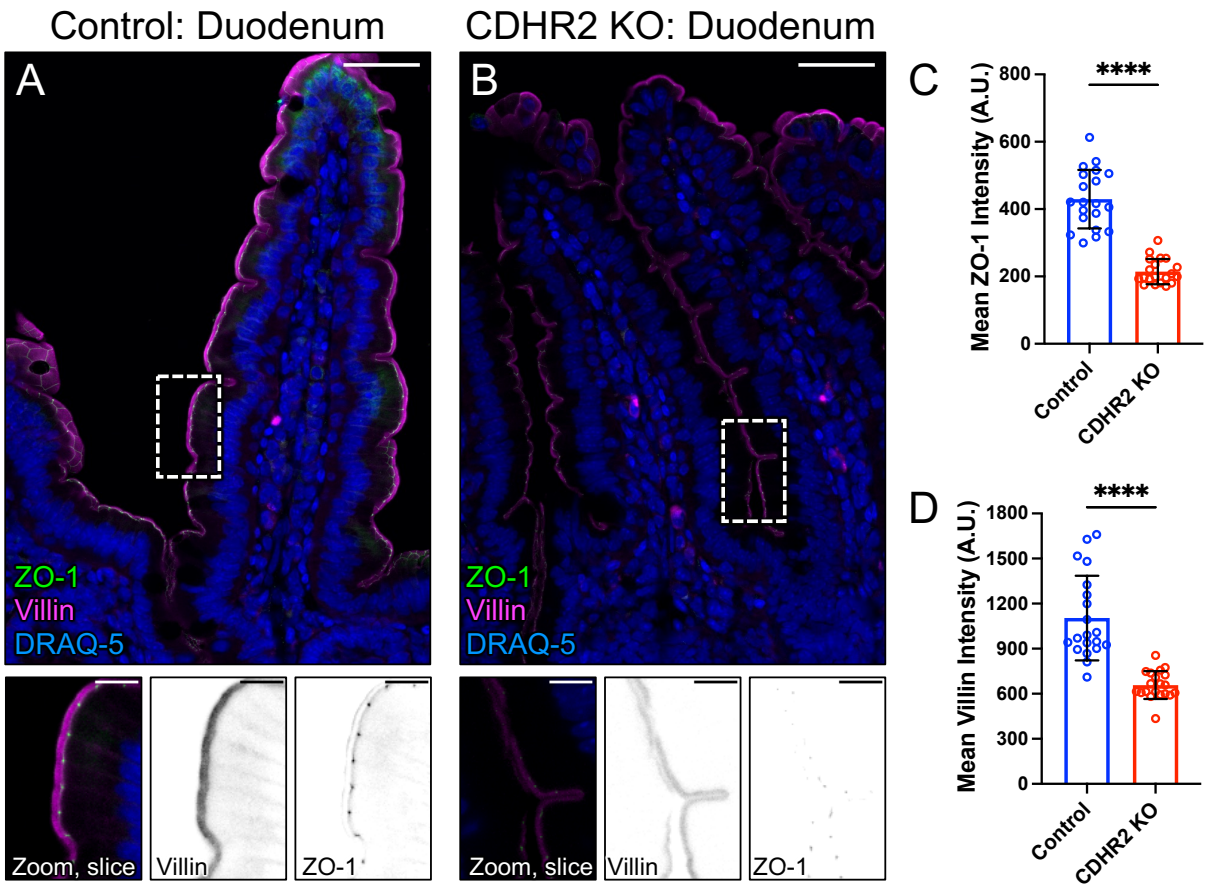

Figure 4-7. The CDHR2 KO mouse has decreased ZO-1 and villin signal. Mouse duodenum stained for ZO-1 (green), villin (magenta), and DRAQ-5 (blue) from (**A**) Control (Cre-) and (**B**) CDRH2 KO (Cre+) mice. The dashed boxes represent the zoom area shown below as a single Z-slice with merged and inverted channel images. (**C**) Thresholded mean ZO-1 intensity measurements and (**D**) thresholded mean villin intensity measurements from n= *2* Control and *n = 2* CDHR2 KO mice littermates, 20 measured villi per condition. **** $p \leq 0.0001$ unpaired t-test. Error bars represent mean ± SD. Matched imaging parameters and LUTs. Scale bars: 40 µm (A-B), 10 µm (Zooms).

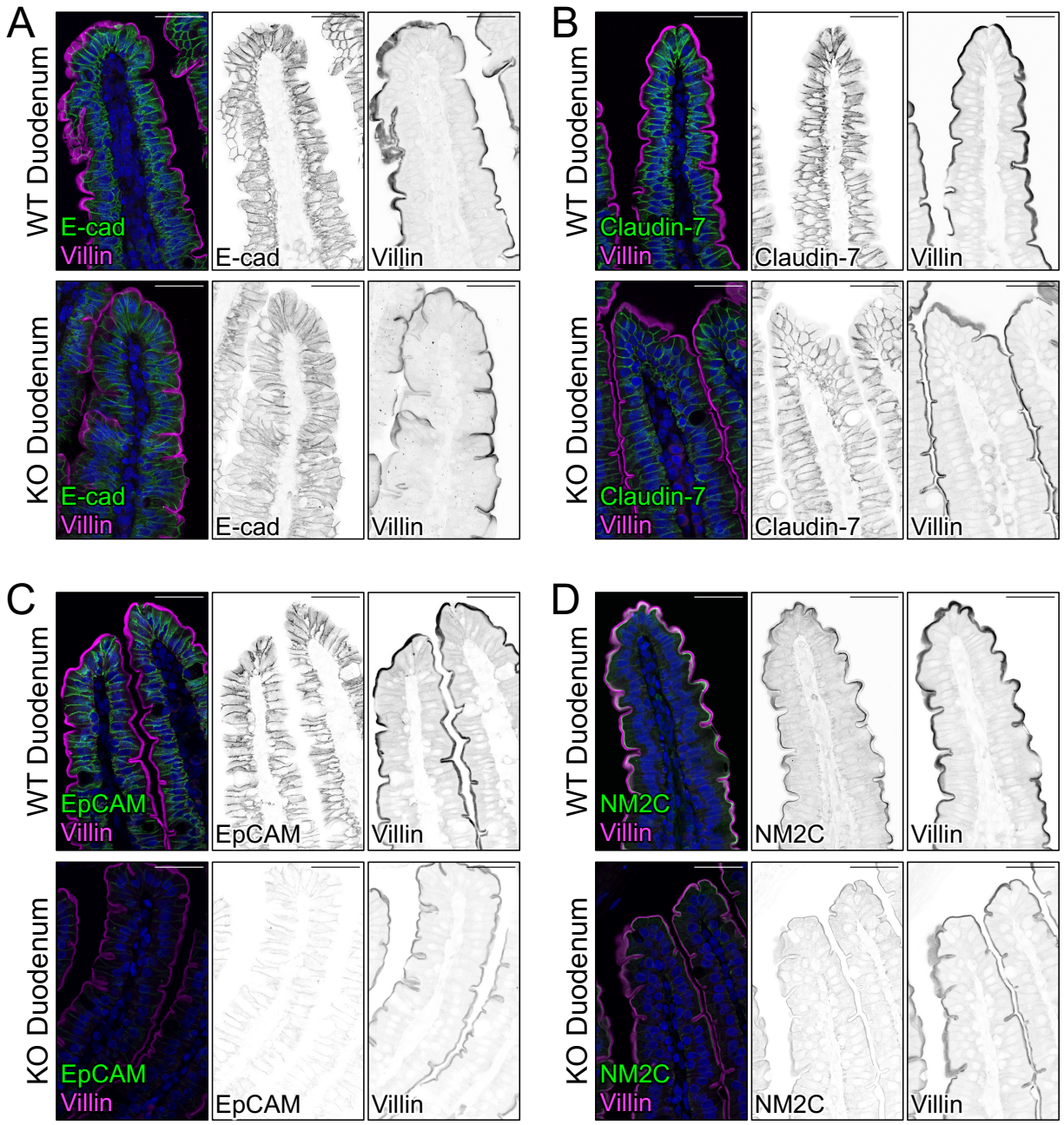

Figure 4-8. Preliminary staining of other junctional proteins in the CDHR2 KO mouse suggests abnormalities. Mouse WT and CDHR2 KO duodenum sections stained for villin (magenta) and the following junctional markers in green: (A) E-cadherin, (B) Claudin-7, (C) EpCAM, (D) NM2C. Matched imaging parameters and LUTs. Scale bars: 40 μm.

Discussion

Transporting epithelia found in the small intestine and kidney tubule rely on an apical brush border of microvilli and tight cell-cell contacts to optimize solute transport and interface with the external environment. The apical intermicrovillar adhesion complex (IMAC), built from protocadherins CDHR2 and CDHR5 and their interacting partners, is crucial for brush border organization (Choi et al., 2020; Crawley et al., 2014b; Crawley et al., 2016; Pinette et al., 2019; Weck et al., 2016). Recently, we identified a transjunctional IMAC connecting microvilli of neighboring cells, spanning across junctions (Cencer et al., 2023). This stable adhesion complex promotes the marginal accumulation of microvilli throughout brush border assembly. Given its localization above cell-cell junctions, we wondered whether the loss of the transjunctional IMAC could also influence junction assembly and function. Indeed, CDHR2 KO CACO-2_{BBE} and CDHR2 KO CL4 cells exhibit a drastic decrease in microvilli clusters, a phenotype associated with all other KD and KO IMAC member studies cited above. Excitingly, we also saw dramatic differences in cell shape and junction structure in both CDHR2 KO cell lines, which we attribute to a loss of membrane tension, coinciding with a significant decrease in NM2C signal. Further probing into junction composition revealed that tight junction proteins ZO-1 and claudin-7 as well as adherens junction proteins E-cadherin, β-catenin, and EpCAM were markedly reduced in signal in the absence of CDHR2.

Does the loss of transjunctional adhesion impact junction integrity and function? To answer this question, we performed TEER measurements over 22 days of epithelial differentiation in CDHR2 KO and Control CACO cells. We found a significant reduction in monolayer resistance of KO cells, implying that junctional integrity was compromised (Srinivasan et al., 2015; Yuan et al., 2020). Furthermore, wound healing assays found that epithelial sheet motility is impaired in

CDHR2 KO CACO cells as demonstrated by decrease in wound closure velocity. Interestingly, however, when mixing CDHR2 KO CL4 cells with Control CL4 cells, it was clear that KO cells are quite motile within their own monolayer, but still fail to close the wound. This is an interesting observation given the original literature on CDHR2, then referred to as protocadherin LKC, in its role as a tumor suppressor (Okazaki et al., 2002; Ose et al., 2009). Notably, a study that reintroduced CDHR2 into colon cancer cells found that it sped wound healing and promoted gap closure (Ose et al., 2009). The study implicated downstream β-catenin signaling as one reason for CDHR2's role in contact inhibition and tumor formation. Relatedly, our CDHR2 KO cells lose β-catenin signal, which has been shown to disrupt coordinated cell motion (Aman and Piotrowski, 2008). Given these connections to the original CDHR2 literature, our new observations offer a unifying theme between the role of apical CDHR2 adhesive complexes in brush border assembly and cell monolayer function. Future studies should focus on potential signaling pathways involved in these processes as well as the possible contribution of the transjunctional IMAC to barrier function in the face of disease.

CHAPTER V

Conclusions and Future Directions

Overall, the two main projects outlined in this thesis point to a mechanism in which apical adhesion complexes support assembly of brush border microvilli and basolateral junctions. The former story establishes a transjunctional adhesion complex situated at the tips of marginal microvilli, spanning neighboring cell junctions (Cencer et al., 2023). This heterophilic complex of protocadherins CDHR2 and CDHR5 exhibits low turnover in the marginal zone, but high turnover in the medial zone. This may be due in part to the formation of force-sensitive cadherin catch bonds between opposing marginal microvilli that strengthen upon increased tensile loads (Rakshit et al., 2012; Sokurenko et al., 2008; Thomas, 2008). Force for transjunctional complex stability may stem from subapical non-muscle myosin-2c, as its inhibition leads to a loss of marginal microvilli enrichment. Furthermore, breakage of heterophilic adhesion complexes through calcium perturbation or KO studies demonstrates that the complex is necessary for microvillar clustering and proper brush border formation (Cencer et al., 2023; Crawley et al., 2014b; Pinette et al., 2019). Interestingly, despite the now well-established role for transjunctional adhesion complexes in microvillar organization, the latter story of this thesis proposes a new function.

In addition to causing microvillar organization defects, CDHR2 KO in cell culture models and mouse intestine also affects cell junctions. This is apparent in immunostaining for markers including ZO-1 and claudin-7 (tight junctions), as well as E-cadherin, β-catenin, and EpCAM (adherens junctions). Further mechanistic experiments revealed that CDHR2 KO CACO and CL4 cells have impaired wound healing and fail to collectively migrate. This phenotype is intriguing considering the classic CDHR2 literature implicating it as a tumor suppressor (Okazaki et al., 2002; Ose et al., 2009). CDHR5 was also first noted to impact cancer cell metastasis, suggesting

that CDHR2/CDHR5 transjunctional complexes may stabilize the cell junctions they bridge (Ding et al., 2020; Losi et al., 2019; Losi et al., 2011). These two chapters focused on the roles of apical cadherin complexes in brush border and junction assembly, yet open several interesting avenues for future studies, as follows:

Do stable adhesion complexes impact actin turnover in microvilli?

The third chapter of this thesis revealed that marginal microvilli are highly stable structures and exhibit constrained motion. Actin turns over in nascent microvilli and actin treadmilling is the driving force behind microvillar motility (Meenderink et al., 2019). However, it remains unknown whether treadmilling still occurs in the stationary microvilli found at cell margins or in mature brush borders. To examine this question, I created a stable CL4 cell line expressing mNeonGreen-β-Actin and performed FRAP at different points in brush border differentiation. Sub confluent cells, mimicking nascent cells with few microvilli, exhibited active actin turnover, with signal recovery plateauing within 2 minutes. Medial microvilli in this context had a slightly higher immobile fraction than marginal microvilli (**Fig. 5-1A-B**). Moreover, the same CL4 cells grown to 4 DPC, a time point in which cell surfaces are fully packed with microvilli, also recovered β-Actin signal, albeit, at what appears a slower rate with signal recovery plateauing at 15+ minutes (**Fig. 5-1C-D**). Overall, these preliminary studies suggest that even mature, stagnant microvilli undergo core bundle actin turnover. This implies that actin treadmilling is still a characteristic of mature actin protrusions, despite their decreased motility. There is evidence in the literature of mature protrusions undergoing actin turnover, such as in stereocilia hair cell bundles, though these structures turnover slowly and only at their distal tip regions (Roy and Perrin, 2018; Rzadzinska et al., 2004; Zhang et al., 2012).

One potential explanation for mature microvilli still undergoing actin turnover is to maintain pushing forces on the overlying membrane (Kovar and Pollard, 2004). If this is true, one would predict that treating mature cell monolayers with a drug to inhibit actin polymerization, such as cytochalasin D, would cause microvilli to collapse against the opposing force of the membrane. Notably, microvilli and stereocilia treated with cytochalasin D do dramatically shorten over drug exposure (Meenderink et al., 2019; Rzadzinska et al., 2004). While there is little published data concerning the treatment of mature brush borders with cytochalasin, treatment of nascent cells showed that the medial microvilli typically orientated at an angle to the apical surface stand up vertically upon inhibition of actin polymerization and treadmilling [see Video S4 of (Meenderink et al., 2019)] (Madara et al., 1986). This counterintuitive result suggests that treadmilling of mature microvillar core bundles has a different purpose rather than counteracting membrane forces. However, it will be necessary to repeat such inhibition experiments in mature cell monolayers to confirm whether this idea is true. If so, another prospective role for maintaining actin turnover in mature structures could be to repair damaged microvilli, an event documented in early *in vivo* studies that has yet to be revisited (Venkatachalam et al., 1978; Weinman et al., 1989).

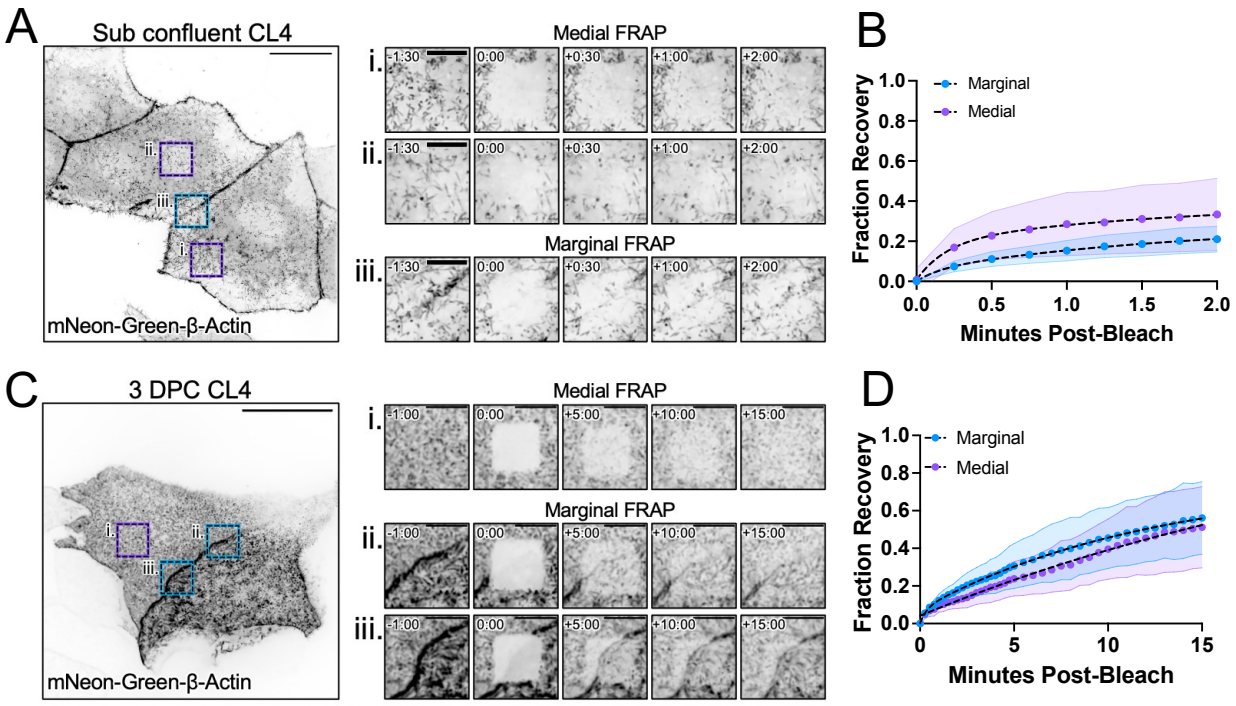

Figure 5-1. Marginal and medial microvilli undergo actin turnover in both nascent and mature brush borders. (**A**) Sub confluent CL4 cells stably expressing mNeon-Green-β-Actin with two medial (**Ai., ii**.) ROIs and one marginal (**Aiii.**) ROI photobleached and monitored over time for signal recovery. (**B**) Fraction recovery from *n = 46* marginal ROIs and *n = 47* medial ROIs. (**C**) 3 DPC mNeon-Green-β-Actin CL4 cells with fully packed brush borders photobleached at one medial (**Bi.**) and two marginal (**Bii., iii.**) ROIs and monitored for signal recovery. (**D**) Fraction recovery from *n = 14* marginal ROIs and *n = 17* medial ROIs. Scale bars: 20 µm and 5 µm (montage zooms).

Do junction proteins interact with microvilli?

The fourth chapter of this thesis outlined a new role for transjunctional adhesion complexes in supporting the basolateral junctions that they span. While the loss of CDHR2 in our perturbation studies suggests that it is primarily the loss of this complex that leads to destabilization of junctions, there may be more to the story. In a BioID2 screen to identify new microvillar interacting proteins using the tip-targeting protein EPS8 as bait, known microvillar tip-enriched proteins were identified including IRSP53 and IRTKS (Gaeta and Tyska, 2023). This method, however,

identified a new protein, KIAA1671, present at the start of protrusion growth and eventually enriched at the base of microvilli. It was determined that because EPS8 is exists at all stages of protrusion growth, it could theoretically interact with base-localized proteins, including KIAA1671. Interestingly, tight junction proteins ZO-1 and ZO-2 were highly enriched in the screened EPS8 interactome, with high spectral counts after mass spectrometry analysis (**Fig. 5-2A**). I investigated this further and found that CL4 cells expressing EGFP-ZO-1 and mCherry-Espin indeed have microvilli-associated ZO-1 puncta at the base and along the length of the actin bundle (**Fig. 5-2B, arrows**). Furthermore, I found instances of protrusions growing out of ZO-1 puncta with ZO-1 remaining at the base of microvilli on a timescale of minutes, much like the behavior seen with KIAA1671 (**Fig. 5-2C, arrows**) (Gaeta et al., 2021a). While has been difficult to image individual protrusion growth events at the margins of cells given their crowded nature, one could speculate that ZO-1 and the circumferential actin belt may serve as a center of microvillar initiation. It is likely that this microvilli-associated population of ZO-1 has been overlooked due to its difference in signal to the more prominent junction population, to which imaging parameters and LUTs are typically scaled. Ironically, a study characterizing the intestinal ZO-1 KO mouse could not fully rationalize the disruption to apical microvilli structure due to the absence of ZO-1 in microvilli (Odenwald et al., 2018). However, they do hint at a soluble intracellular ZO-1 pool, that has been noted but not yet characterized, as a potential explanation (Shen et al., 2008). Given this prediction and my preliminary data, it is possible that ZO-1 at the base of microvilli may help maintain their structure, similar to how NM2C – also existing in a junctional and subapical pool – anchors core bundle rootlets in the terminal web (Chinowsky et al., 2020).

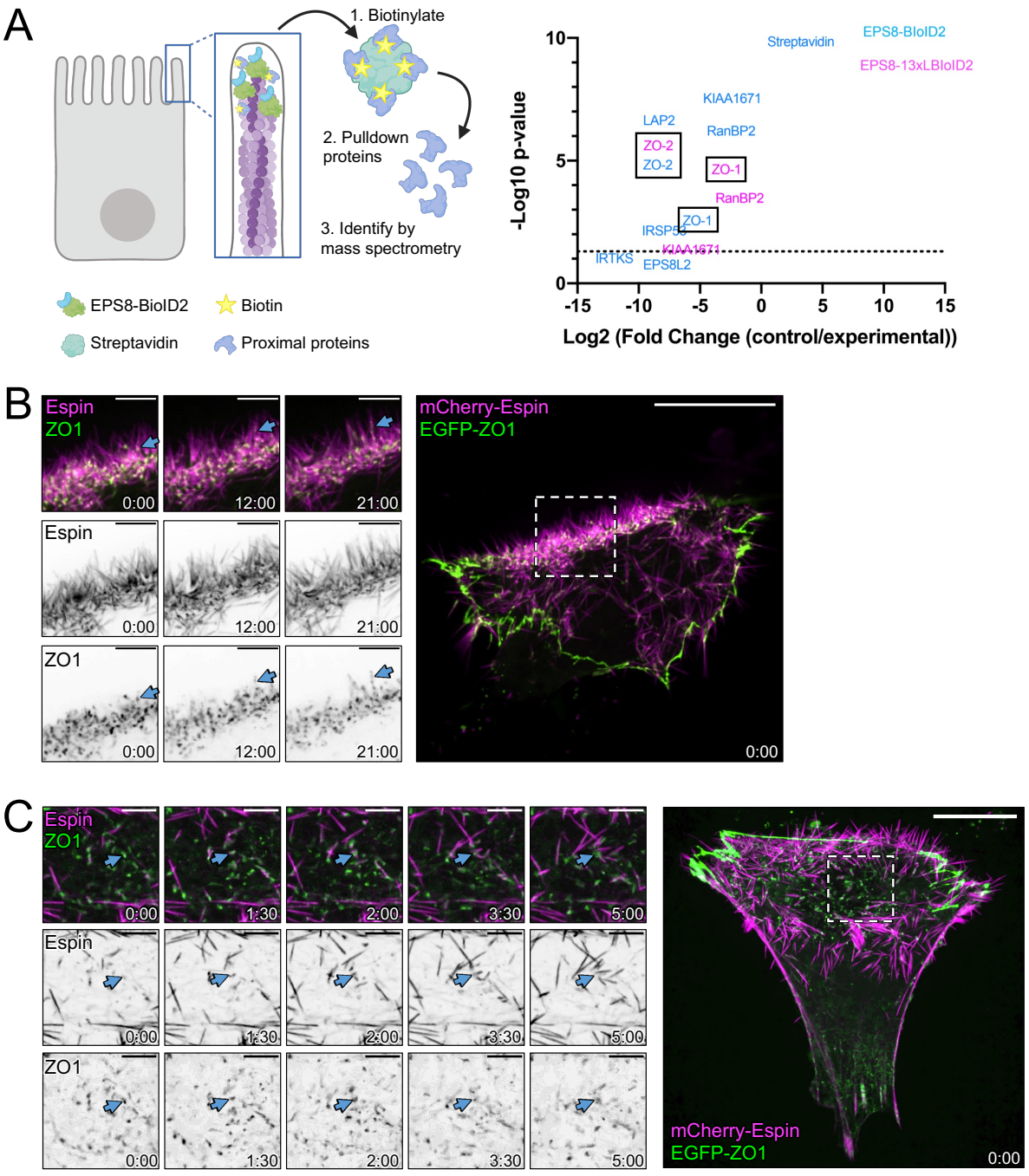

Figure 5-2. ZO-1 can be detected at the base of microvilli and at sites of microvillar growth. (**A**) Schematic for the BioID2-EPS8 interactome screen as described in (Gaeta and Tyska, 2023). Plot represents spectral counts from a protein pulldown of myc-BioID2 control construct vs EPS8-EPS8-BioID2 and EPS8-13XLinker-BioID2 constructs. Higher y-axis value coincides with higher spectral counts. (**B**) CL4 cell expressing mCherry-Espin (magenta) and EGFP-ZO1 (green). Blue arrows point to puncta of ZO-1 moving along the length of espin microvilli bundles. (**C**) CL4 cell expressing mCherry-Espin (magenta) and EGFP-ZO1 (green). Blue arrows point to a punctum of ZO-1 from which three espin bundles emerge. Scale bars: 20 µm and 5 µm (montage zooms).

The next question that arises is how ZO-1 interacts with microvilli on a molecular level. The domain structure of ZO-1 is well-defined, containing three PDZ domains, a SH3 domain, and guanylate kinase (GuK) domain in its N-terminal half. The C-terminus is home to a poly-proline rich region that interacts with F-actin (Fanning et al., 1998). Further investigation found a 220AA actin binding region (ABR) necessary for ZO-1's association with F-actin (Fanning et al., 2002). While it is possible that ZO-1 binds to microvilli core bundles via its ABR, the ZO-1 KO mouse study uncovered that the ABR alone is not sufficient to restore microvilli organization, suggesting that there may be a different mode of interaction (Odenwald et al., 2018). An alternative mode of ZO-1 interaction with microvilli may be through the IMAC. It is known that the PDZ2 domain of USH1C interacts with the C-terminal PDZ binding motif (PBM) of CDHR2, but not CDHR5 (Li et al., 2016; Li et al., 2017; Yan et al., 2022). Canonical PDZ domains share characteristic folds including five β-strands and two α-helices determined through PDZ structural alignments (Amacher et al., 2020). ZO-1 PDZ3 has ~73% sequence similarity and ~53% shared identity with PDZ2 of USH1C and can be closely overlayed with CDHR2's PBM (**Fig. 5-3A-C**). Moreover, high-magnification imaging of the tagged EGFP-CDHR2 mouse duodenum stained for ZO-1 revealed faint puncta of endogenous CDHR2 colocalized with ZO-1 at tight junctions (**Fig. 5-3D, arrows**). This was especially apparent in cutting through the *en face* whole mount section to the tight junction level (**Fig. 5-3E**). This is not the first instance of classically denoted "junctional" proteins being found at the apical surface. While polarity proteins are classically thought to localize subapically or at junctions, a recent study using super-resolution imaging uncovered the polarity proteins PAR6α, aPKC, PALS1, and PATJ within or at the base of intestinal microvilli (Mangeol et al., 2022). Additionally, Nectin-3, which functions as a cell-cell adhesion molecule at adherens junctions, was unexpectedly found in the brush border of mouse intestine (Childress et al., 2023).

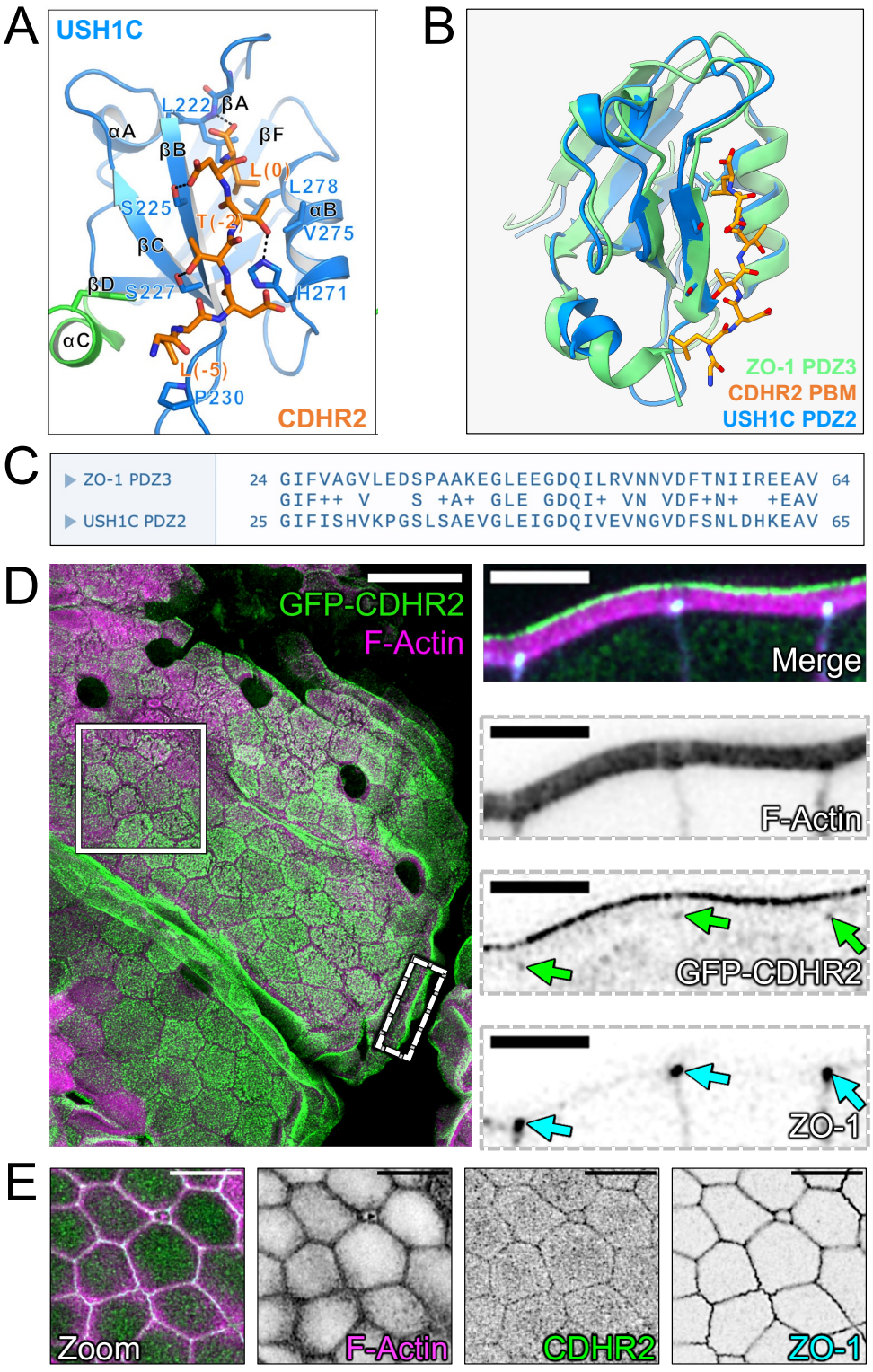
A
USH1C
αA
βA
βB
βF
L222
L(0)
L278
S225
T(-2)
αB
V275
βC
βD
S227
H271
αC
L(-5)
P230
CDHR2
B
ZO-1 PDZ3
CDHR2 PBM
USH1C PDZ2
C
ZO-1 PDZ3
USH1C PDZ2
24 GIFVAGVLEDSPAAKEGLEEGDQILRVNNVDFTNIIREEAV 64
GIF++ V S +A+ GLE GDQI+ VN VDF+N+ +EAV
25 GIFISHVKPGSLSAEVGLEIGDQIVEVNGVDFSNLDHKEAV 65
D
GFP-CDHR2
F-Actin
Merge
F-Actin
GFP-CDHR2
ZO-1
E
Zoom
F-Actin
CDHR2
ZO-1

Figure 5-3. Proposed PDZ-mediated interaction of CDHR2 and ZO-1. (**A**) Known structural binding interface between CDHR2 PBM and USH1C PDZ2 (Yan et al., 2022); Creative Commons Attribution License. (**B**) Structural alignment of USH1C PDZ2 bound to CDHR2 PBM (PDB: 7X2E) with ZO-1 PDZ3 (PDB: 3TSV) reveals homologous folds. ChimeraX developed by (Pettersen et al., 2021). (**C**) Smith-Waterman local alignment in SnapGene of ZO-1 PDZ3 and USH1C PDZ2. (**D**) Whole mount EGFP-CDHR2 mouse duodenum tissue stained for F-actin (magenta) with endogenous CDHR2 labeling (green). (Right) Zoom of a single Z-slice of the dashed box marked on the left panel. Arrows point to puncta of CDHR2 (green) colocalizing with ZO-1 (cyan) at tight junctions. (**E**) *En face* single Z slice of the solid box in (D) showing endogenous CDHR2 in junctions. Scale bars: 20 μm (D), 5 μm (D, Zooms), and 10 μm (E).

Does loss of CDHR2-stabilized microvilli impact bacterial infection?

As previously discussed, the brush border serves a dual purpose – optimizing surface area for solute transport and preventing pathogen entrance (Louvard et al., 1992; Shifrin et al., 2012). There are bacteria species, however, that use the brush border to their advantage, remodeling F-actin to promote attachment and motility (Shifrin et al., 2014; Stevens et al., 2006). As one of these pathogens, *Escherichia coli* (*E. coli*) infects the intestine with two different strains, enteropathogenic and enterohemorrhagic *E. coli* – EPEC and EHEC, respectfully. Each of these strains secrete unique bacterial effectors into the host cell via a type III secretion system that recruit host proteins involved in actin reorganization. This includes N-WASP which promotes Arp2/3 branched actin nucleation, creating actin-rich "pedestals" that serve as intimate bacterial attachment points (Campellone, 2010). Pedestals can also facilitate cell-to-cell spread, passing bacteria over neighboring cell margins (Velle and Campellone, 2017). Given the enrichment and stabilization of marginal microvilli via transjunctional CDHR2/CDHR5 adhesion complexes, it is conceivable that these marginal connections may influence bacteria spread and colonization (Cencer et al., 2023). Relatedly, one study examining EHEC infection in human colonoids found that CDHR2 is one of the first targets of infection (In et al., 2016). Specifically, the EHEC serine protease EspP reduces CDHR2 levels in infected colonoids. Furthermore, purified recombinant EspP is still sufficient to decrease CDHR2 expression. Interestingly, EHEC infection also affects

tight junction integrity, causing a reduction in TEER. This study concluded that this could be due to change in claudin distribution, which was noted in a mouse EHEC infection model (Roxas et al., 2010). Given that CDHR2 is a primary target of EHEC infection, I wondered whether CDHR2 KO CACO-2_{BBE} cells would be susceptible to bacteria attachment. Using an engineered EPEC strain, KC12+$EspF_U$, that is modified to mimic EHEC pedestal formation and infection, 16 DPC Control and CDHR2 KO CACO cells were infected and stained for CDHR2, ZO-1, F-actin, and DAPI to mark bacteria (Velle and Campellone, 2017). Interestingly, CDHR2 KO cells appeared to be more susceptible to infection, with a significantly higher number of bacteria/μm^2 (**Fig. 5-4**). This is most likely because CDHR2 KO cells already have a disrupted brush border, making initial bacterial attachment easier. Alternatively, the same number of bacteria could attach in both Control and KO cells, but the lack of a protective brush border in KO cells could speed initial attachment, allowing the bacteria more time to divide and grow in number. Additional experiments in live cells would be required to parse out these two ideas and roles of the IMAC in infection.

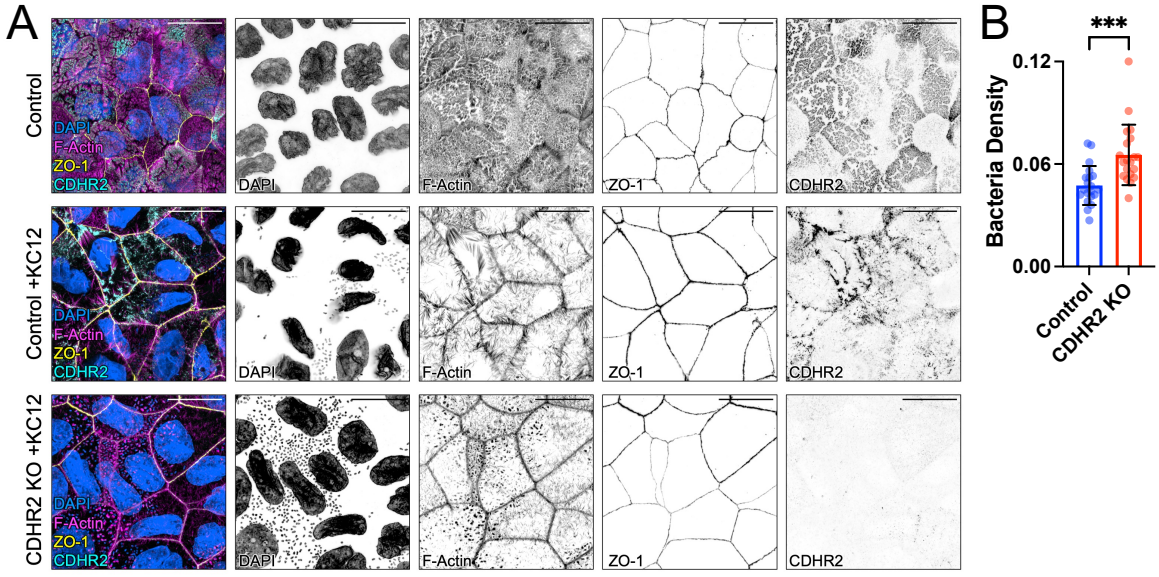

Figure 5-4. CDHR2 KO leads to increased *E. coli* attachment. (**A**) 16 DPC CACO non-infected Control, Control +KC12 EPEC strain, CDHR2 KO +KC12 EPEC strain stained for DAPI (blue), F-actin (magenta), ZO-1 (yellow), and CDHR2 (cyan). (**B**) Bacteria density quantified as number of bacteria per μm^2. Unpaired t-test; ***p = 0.005. Error bars represent mean ± SD. Scale bars: 10 µm.

REFERENCES

Ahmed, S., W.I. Goh, and W. Bu. 2010. I-BAR domains, IRSp53 and filopodium formation. *Semin Cell Dev Biol*. 21:350-356.

Algrain, M., O. Turunen, A. Vaheri, D. Louvard, and M. Arpin. 1993. Ezrin contains cytoskeleton and membrane binding domains accounting for its proposed role as a membrane-cytoskeletal linker. *J Cell Biol*. 120:129-139.

Amacher, J.F., L. Brooks, T.H. Hampton, and D.R. Madden. 2020. Specificity in PDZ-peptide interaction networks: Computational analysis and review. *J Struct Biol X*. 4:100022.

Aman, A., and T. Piotrowski. 2008. Wnt/beta-catenin and Fgf signaling control collective cell migration by restricting chemokine receptor expression. *Dev Cell*. 15:749-761.

Amsler, K., and J.S. Cook. 1985. Linear relationship of phlorizin-binding capacity and hexose uptake during differentiation in a clone of LLC-PK1 cells. *J Cell Physiol*. 122:254-258.

Atilgan, E., D. Wirtz, and S.X. Sun. 2006. Mechanics and dynamics of actin-driven thin membrane protrusions. *Biophys J*. 90:65-76.

Baranwal, S., N.G. Naydenov, G. Harris, V. Dugina, K.G. Morgan, C. Chaponnier, and A.I. Ivanov. 2012. Nonredundant roles of cytoplasmic beta- and gamma-actin isoforms in regulation of epithelial apical junctions. *Mol Biol Cell*. 23:3542-3553.

Bartles, J.R., L. Zheng, A. Li, A. Wierda, and B. Chen. 1998. Small espin: a third actin-bundling protein and potential forked protein ortholog in brush border microvilli. *J Cell Biol*. 143:107-119.

Bement, W.M., T. Hasson, J.A. Wirth, R.E. Cheney, and M.S. Mooseker. 1994. Identification and overlapping expression of multiple unconventional myosin genes in vertebrate cell types. *Proc Natl Acad Sci U S A*. 91:6549-6553.

Birdsall, H.H., and T.G. Hammond. 2021. Role of Shear Stress on Renal Proximal Tubular Cells for Nephrotoxicity Assays. *J Toxicol*. 2021:6643324.

Bitner-Glindzicz, M., K.J. Lindley, P. Rutland, D. Blaydon, V.V. Smith, P.J. Milla, K. Hussain, J. Furth-Lavi, K.E. Cosgrove, R.M. Shepherd, P.D. Barnes, R.E. O'Brien, P.A. Farndon, J. Sowden, X.Z. Liu, M.J. Scanlan, S. Malcolm, M.J. Dunne, A. Aynsley-Green, and B.

Glaser. 2000. A recessive contiguous gene deletion causing infantile hyperinsulinism, enteropathy and deafness identifies the Usher type 1C gene. *Nat Genet*. 26:56-60.

Bondow, B.J., M.L. Faber, K.J. Wojta, E.M. Walker, and M.A. Battle. 2012. E-cadherin is required for intestinal morphogenesis in the mouse. *Dev Biol*. 371:1-12.

Bretscher, A., and K. Weber. 1979. Villin: the major microfilament-associated protein of the intestinal microvillus. *Proc Natl Acad Sci U S A*. 76:2321-2325.

Bretscher, A., and K. Weber. 1980. Fimbrin, a new microfilament-associated protein present in microvilli and other cell surface structures. *J Cell Biol*. 86:335-340.

Brunet, T., B.T. Larson, T.A. Linden, M.J.A. Vermeij, K. McDonald, and N. King. 2019. Light-regulated collective contractility in a multicellular choanoflagellate. *Science*. 366:326-334.

Buckley, C.D., J. Tan, K.L. Anderson, D. Hanein, N. Volkmann, W.I. Weis, W.J. Nelson, and A.R. Dunn. 2014. Cell adhesion. The minimal cadherin-catenin complex binds to actin filaments under force. *Science*. 346:1254211.

Buning, C., N. Geissler, M. Prager, A. Sturm, D.C. Baumgart, J. Buttner, S. Buhner, V. Haas, and H. Lochs. 2012. Increased small intestinal permeability in ulcerative colitis: rather genetic than environmental and a risk factor for extensive disease? *Inflamm Bowel Dis*. 18:1932-1939.

Campellone, K.G. 2010. Cytoskeleton-modulating effectors of enteropathogenic and enterohaemorrhagic Escherichia coli: Tir, EspFU and actin pedestal assembly. *FEBS J*. 277:2390-2402.

Carlier, M.F. 1990. Actin polymerization and ATP hydrolysis. *Adv Biophys*. 26:51-73.

Cavey, M., M. Rauzi, P.F. Lenne, and T. Lecuit. 2008. A two-tiered mechanism for stabilization and immobilization of E-cadherin. *Nature*. 453:751-756.

Cencer, C.S., J.B. Silverman, L.M. Meenderink, E.S. Krystofiak, B.A. Millis, and M.J. Tyska. 2023. Adhesion-based capture stabilizes nascent microvilli at epithelial cell junctions. *Dev Cell*.

Charras, G., and A.S. Yap. 2018. Tensile Forces and Mechanotransduction at Cell-Cell Junctions. *Curr Biol*. 28:R445-R457.

Chen, Z.Y., T. Hasson, D.S. Zhang, B.J. Schwender, B.H. Derfler, M.S. Mooseker, and D.P. Corey. 2001. Myosin-VIIb, a novel unconventional myosin, is a constituent of microvilli in transporting epithelia. *Genomics*. 72:285-296.

Childress, K.O., C.S. Cencer, M.J. Tyska, and D.B. Lacy. 2023. Nectin-3 and shed forms of CSPG4 can serve as epithelial cell receptors for Clostridioides difficile TcdB. *mBio*:e0185723.

Chinowsky, C.R., J.A. Pinette, L.M. Meenderink, K.S. Lau, and M.J. Tyska. 2020. Nonmuscle myosin-2 contractility-dependent actin turnover limits the length of epithelial microvilli. *Mol Biol Cell*. 31:2803-2815.

Choi, M.S., M.J. Graves, S. Matoo, Z.A. Storad, R.A. El Sheikh Idris, M.L. Weck, Z.B. Smith, M.J. Tyska, and S.W. Crawley. 2020. The small EF-hand protein CALML4 functions as a critical myosin light chain within the intermicrovillar adhesion complex. *J Biol Chem*. 295:9281-9296.

Clarke, D.N., and A.C. Martin. 2021. Actin-based force generation and cell adhesion in tissue morphogenesis. *Curr Biol*. 31:R667-R680.

Collatz, M.B., R. Rudel, and H. Brinkmeier. 1997. Intracellular calcium chelator BAPTA protects cells against toxic calcium overload but also alters physiological calcium responses. *Cell Calcium*. 21:453-459.

Conant, D., T. Hsiau, N. Rossi, J. Oki, T. Maures, K. Waite, J. Yang, S. Joshi, R. Kelso, K. Holden, B.L. Enzmann, and R. Stoner. 2022. Inference of CRISPR Edits from Sanger Trace Data. *CRISPR J*. 5:123-130.

Coudrier, E., D. Kerjaschki, and D. Louvard. 1988. Cytoskeleton organization and submembranous interactions in intestinal and renal brush borders. *Kidney Int*. 34:309-320.

Crawley, S.W., M.S. Mooseker, and M.J. Tyska. 2014a. Shaping the intestinal brush border. *J Cell Biol*. 207:441-451.

Crawley, S.W., D.A. Shifrin, Jr., N.E. Grega-Larson, R.E. McConnell, A.E. Benesh, S. Mao, Y. Zheng, Q.Y. Zheng, K.T. Nam, B.A. Millis, B. Kachar, and M.J. Tyska. 2014b. Intestinal

brush border assembly driven by protocadherin-based intermicrovillar adhesion. *Cell*. 157:433-446.

Crawley, S.W., M.L. Weck, N.E. Grega-Larson, D.A. Shifrin, Jr., and M.J. Tyska. 2016. ANKS4B Is Essential for Intermicrovillar Adhesion Complex Formation. *Dev Cell*. 36:190-200.

Croce, A., G. Cassata, A. Disanza, M.C. Gagliani, C. Tacchetti, M.G. Malabarba, M.F. Carlier, G. Scita, R. Baumeister, and P.P. Di Fiore. 2004. A novel actin barbed-end-capping activity in EPS-8 regulates apical morphogenesis in intestinal cells of Caenorhabditis elegans. *Nat Cell Biol*. 6:1173-1179.

Delacour, D., J. Salomon, S. Robine, and D. Louvard. 2016. Plasticity of the brush border - the yin and yang of intestinal homeostasis. *Nat Rev Gastroenterol Hepatol*. 13:161-174.

Ding, X., X. Tian, W. Liu, and Z. Li. 2020. CDHR5 inhibits proliferation of hepatocellular carcinoma and predicts clinical prognosis. *Ir J Med Sci*. 189:439-447.

Disanza, A., M.F. Carlier, T.E. Stradal, D. Didry, E. Frittoli, S. Confalonieri, A. Croce, J. Wehland, P.P. Di Fiore, and G. Scita. 2004. Eps8 controls actin-based motility by capping the barbed ends of actin filaments. *Nat Cell Biol*. 6:1180-1188.

Disanza, A., S. Mantoani, M. Hertzog, S. Gerboth, E. Frittoli, A. Steffen, K. Berhoerster, H.J. Kreienkamp, F. Milanesi, P.P. Di Fiore, A. Ciliberto, T.E. Stradal, and G. Scita. 2006. Regulation of cell shape by Cdc42 is mediated by the synergic actin-bundling activity of the Eps8-IRSp53 complex. *Nat Cell Biol*. 8:1337-1347.

Diz-Munoz, A., D.A. Fletcher, and O.D. Weiner. 2013. Use the force: membrane tension as an organizer of cell shape and motility. *Trends Cell Biol*. 23:47-53.

Du, Z., Y. Duan, Q. Yan, A.M. Weinstein, S. Weinbaum, and T. Wang. 2004. Mechanosensory function of microvilli of the kidney proximal tubule. *Proc Natl Acad Sci U S A*. 101:13068-13073.

Ebrahim, S., T. Fujita, B.A. Millis, E. Kozin, X. Ma, S. Kawamoto, M.A. Baird, M. Davidson, S. Yonemura, Y. Hisa, M.A. Conti, R.S. Adelstein, H. Sakaguchi, and B. Kachar. 2013. NMII forms a contractile transcellular sarcomeric network to regulate apical cell junctions and tissue geometry. *Curr Biol*. 23:731-736.

Engstrom, H., and B. Engstrom. 1978. Structure of the hairs on cochlear sensory cells. *Hear Res*. 1:49-66.

Fanning, A.S., B.J. Jameson, L.A. Jesaitis, and J.M. Anderson. 1998. The tight junction protein ZO-1 establishes a link between the transmembrane protein occludin and the actin cytoskeleton. *J Biol Chem*. 273:29745-29753.

Fanning, A.S., T.Y. Ma, and J.M. Anderson. 2002. Isolation and functional characterization of the actin binding region in the tight junction protein ZO-1. *FASEB J*. 16:1835-1837.

Farquhar, M.G., and G.E. Palade. 1963. Junctional complexes in various epithelia. *J Cell Biol*. 17:375-412.

Fath, K.R., S.D. Obenauf, and D.R. Burgess. 1990. Cytoskeletal protein and mRNA accumulation during brush border formation in adult chicken enterocytes. *Development*. 109:449-459.

Fievet, B.T., A. Gautreau, C. Roy, L. Del Maestro, P. Mangeat, D. Louvard, and M. Arpin. 2004. Phosphoinositide binding and phosphorylation act sequentially in the activation mechanism of ezrin. *J Cell Biol*. 164:653-659.

Firat-Karalar, E.N., and M.D. Welch. 2011. New mechanisms and functions of actin nucleation. *Curr Opin Cell Biol*. 23:4-13.

Fitz, G.N., M.L. Weck, C. Bodnya, O.L. Perkins, and M.J. Tyska. 2023. Protrusion growth driven by myosin-generated force. *Dev Cell*. 58:18-33 e16.

Footer, M.J., J.W. Kerssemakers, J.A. Theriot, and M. Dogterom. 2007. Direct measurement of force generation by actin filament polymerization using an optical trap. *Proc Natl Acad Sci U S A*. 104:2181-2186.

Gaeta, I.M., L.M. Meenderink, M.M. Postema, C.S. Cencer, and M.J. Tyska. 2021a. Direct visualization of epithelial microvilli biogenesis. *Curr Biol*. 31:2561-2575 e2566.

Gaeta, I.M., L.M. Meenderink, and M.J. Tyska. 2021b. A protocol for imaging microvilli biogenesis on the surface of cultured porcine kidney epithelial cell monolayers. *STAR Protoc*. 2:100998.

Gaeta, I.M., and M.J. Tyska. 2023. BioID2 screening identifies KIAA1671 as an EPS8 proximal factor that marks sites of microvillus growth. *Mol Biol Cell*. 34:ar31.

Garcia, M.A., W.J. Nelson, and N. Chavez. 2018. Cell-Cell Junctions Organize Structural and Signaling Networks. *Cold Spring Harb Perspect Biol*. 10.

Garcia-Castillo, M.D., D.J. Chinnapen, and W.I. Lencer. 2017. Membrane Transport across Polarized Epithelia. *Cold Spring Harb Perspect Biol*. 9.

Gary, R., and A. Bretscher. 1995. Ezrin self-association involves binding of an N-terminal domain to a normally masked C-terminal domain that includes the F-actin binding site. *Mol Biol Cell*. 6:1061-1075.

Goldberg, M., C. Peshkovsky, A. Shifteh, and Q. Al-Awqati. 2000. mu-Protocadherin, a novel developmentally regulated protocadherin with mucin-like domains. *J Biol Chem*. 275:24622-24629.

Gov, N.S. 2006. Dynamics and morphology of microvilli driven by actin polymerization. *Phys Rev Lett*. 97:018101.

Granger, B., and R.F. Baker. 1950. Electron microscope investigation of the striated border of intestinal epithelium. *Anat Rec*. 107:423-441.

Grati, M., and B. Kachar. 2011. Myosin VIIa and sans localization at stereocilia upper tip-link density implicates these Usher syndrome proteins in mechanotransduction. *Proc Natl Acad Sci U S A*. 108:11476-11481.

Gray, M.E., Z.R. Johnson, D. Modak, E. Tamilselvan, M.J. Tyska, and M. Sotomayor. 2021. Heterophilic and homophilic cadherin interactions in intestinal intermicrovillar links are species dependent. *PLoS Biol*. 19:e3001463.

Grimm-Gunter, E.M., C. Revenu, S. Ramos, I. Hurbain, N. Smyth, E. Ferrary, D. Louvard, S. Robine, and F. Rivero. 2009. Plastin 1 binds to keratin and is required for terminal web assembly in the intestinal epithelium. *Mol Biol Cell*. 20:2549-2562.

Gumbiner, B.M. 2005. Regulation of cadherin-mediated adhesion in morphogenesis. *Nat Rev Mol Cell Biol*. 6:622-634.

Guo, B., and W.H. Guilford. 2006. Mechanics of actomyosin bonds in different nucleotide states are tuned to muscle contraction. *Proc Natl Acad Sci U S A*. 103:9844-9849.

Halbleib, J.M., and W.J. Nelson. 2006. Cadherins in development: cell adhesion, sorting, and tissue morphogenesis. *Genes Dev*. 20:3199-3214.

Hall, P.A., P.J. Coates, B. Ansari, and D. Hopwood. 1994. Regulation of cell number in the mammalian gastrointestinal tract: the importance of apoptosis. *J Cell Sci*. 107 (Pt 12):3569-3577.

Hegan, P.S., H. Giral, M. Levi, and M.S. Mooseker. 2012. Myosin VI is required for maintenance of brush border structure, composition, and membrane trafficking functions in the intestinal epithelial cell. *Cytoskeleton (Hoboken)*. 69:235-251.

Heintzelman, M.B., and M.S. Mooseker. 1990. Assembly of the brush border cytoskeleton: changes in the distribution of microvillar core proteins during enterocyte differentiation in adult chicken intestine. *Cell Motil Cytoskeleton*. 15:12-22.

Helander, H.F., and L. Fandriks. 2014. Surface area of the digestive tract - revisited. *Scand J Gastroenterol*. 49:681-689.

Hertzog, M., F. Milanesi, L. Hazelwood, A. Disanza, H. Liu, E. Perlade, M.G. Malabarba, S. Pasqualato, A. Maiolica, S. Confalonieri, C. Le Clainche, N. Offenhauser, J. Block, K. Rottner, P.P. Di Fiore, M.F. Carlier, N. Volkmann, D. Hanein, and G. Scita. 2010. Molecular basis for the dual function of Eps8 on actin dynamics: bundling and capping. *PLoS Biol*. 8:e1000387.

Hidalgo, I.J., T.J. Raub, and R.T. Borchardt. 1989. Characterization of the human colon carcinoma cell line (Caco-2) as a model system for intestinal epithelial permeability. *Gastroenterology*. 96:736-749.

Higashi, T., A.C. Saito, Y. Fukazawa, M. Furuse, A.Y. Higashi, M. Ono, and H. Chiba. 2023. EpCAM proteolysis and release of complexed claudin-7 repair and maintain the tight junction barrier. *J Cell Biol*. 222.

Higgs, H.N. 2004. There goes the neighbourhood: Eps8 joins the barbed-end crowd. *Nat Cell Biol*. 6:1147-1149.

Hirokawa, N., L.G. Tilney, K. Fujiwara, and J.E. Heuser. 1982. Organization of actin, myosin, and intermediate filaments in the brush border of intestinal epithelial cells. *J Cell Biol*. 94:425-443.

Hoffman, B.D., and A.S. Yap. 2015. Towards a Dynamic Understanding of Cadherin-Based Mechanobiology. *Trends Cell Biol*. 25:803-814.

Hollander, D., C.M. Vadheim, E. Brettholz, G.M. Petersen, T. Delahunty, and J.I. Rotter. 1986. Increased intestinal permeability in patients with Crohn's disease and their relatives. A possible etiologic factor. *Ann Intern Med*. 105:883-885.

Honda, H. 2017. The world of epithelial sheets. *Dev Growth Differ*. 59:306-316.

Houdusse, A., and M.A. Titus. 2021. The many roles of myosins in filopodia, microvilli and stereocilia. *Curr Biol*. 31:R586-R602.

Huang, L.Y., Y.P. Wang, B.F. Wei, J. Yang, J.Q. Wang, B.H. Wu, Z.Z. Zhang, Y.Y. Hou, W.M. Sun, R.M. Hu, G. Ning, and Z.G. Han. 2013. Deficiency of IRTKS as an adaptor of insulin receptor leads to insulin resistance. *Cell Res*. 23:1310-1321.

Hudspeth, A.J. 1985. The cellular basis of hearing: the biophysics of hair cells. *Science*. 230:745-752.

Hull, B.E., and L.A. Staehelin. 1979. The terminal web. A reevaluation of its structure and function. *J Cell Biol*. 81:67-82.

Hull, R.N., W.R. Cherry, and G.W. Weaver. 1976. The origin and characteristics of a pig kidney cell strain, LLC-PK. *In Vitro*. 12:670-677.

Hutchinson, E.G., and J.M. Thornton. 1993. The Greek key motif: extraction, classification and analysis. *Protein Eng*. 6:233-245.

In, J., J. Foulke-Abel, N.C. Zachos, A.M. Hansen, J.B. Kaper, H.D. Bernstein, M. Halushka, S. Blutt, M.K. Estes, M. Donowitz, and O. Kovbasnjuk. 2016. Enterohemorrhagic Escherichia coli reduce mucus and intermicrovillar bridges in human stem cell-derived colonoids. *Cell Mol Gastroenterol Hepatol*. 2:48-62 e43.

Jumarie, C., and C. Malo. 1991. Caco-2 cells cultured in serum-free medium as a model for the study of enterocytic differentiation in vitro. *J Cell Physiol*. 149:24-33.

Kachar, B., M. Parakkal, M. Kurc, Y. Zhao, and P.G. Gillespie. 2000. High-resolution structure of hair-cell tip links. *Proc Natl Acad Sci U S A*. 97:13336-13341.

Kale, G.R., X. Yang, J.M. Philippe, M. Mani, P.F. Lenne, and T. Lecuit. 2018. Distinct contributions of tensile and shear stress on E-cadherin levels during morphogenesis. *Nat Commun*. 9:5021.

Kaszak, I., O. Witkowska-Pilaszewicz, Z. Niewiadomska, B. Dworecka-Kaszak, F. Ngosa Toka, and P. Jurka. 2020. Role of Cadherins in Cancer-A Review. *Int J Mol Sci*. 21.

Katsaros, C., D. Karyophyllis, and B. Galatis. 2006. Cytoskeleton and morphogenesis in brown algae. *Ann Bot*. 97:679-693.

Kazmierczak, P., H. Sakaguchi, J. Tokita, E.M. Wilson-Kubalek, R.A. Milligan, U. Muller, and B. Kachar. 2007. Cadherin 23 and protocadherin 15 interact to form tip-link filaments in sensory hair cells. *Nature*. 449:87-91.

Kim, S.Y., S. Yasuda, H. Tanaka, K. Yamagata, and H. Kim. 2011. Non-clustered protocadherin. *Cell Adh Migr*. 5:97-105.

Klezovitch, O., and V. Vasioukhin. 2015. Cadherin signaling: keeping cells in touch. *F1000Res*. 4:550.

Kong, F., A.J. Garcia, A.P. Mould, M.J. Humphries, and C. Zhu. 2009. Demonstration of catch bonds between an integrin and its ligand. *J Cell Biol*. 185:1275-1284.

Kovar, D.R., and T.D. Pollard. 2004. Insertional assembly of actin filament barbed ends in association with formins produces piconewton forces. *Proc Natl Acad Sci U S A*. 101:14725-14730.

Kowalczyk, A.P., and K.J. Green. 2013. Structure, function, and regulation of desmosomes. *Prog Mol Biol Transl Sci*. 116:95-118.

Krndija, D., F. El Marjou, B. Guirao, S. Richon, O. Leroy, Y. Bellaiche, E. Hannezo, and D. Matic Vignjevic. 2019. Active cell migration is critical for steady-state epithelial turnover in the gut. *Science*. 365:705-710.

Kuo, W.T., L. Zuo, M.A. Odenwald, S. Madha, G. Singh, C.B. Gurniak, C. Abraham, and J.R. Turner. 2021. The Tight Junction Protein ZO-1 Is Dispensable for Barrier Function but Critical for Effective Mucosal Repair. *Gastroenterology*. 161:1924-1939.

Kurochkina, N., and U. Guha. 2013. SH3 domains: modules of protein-protein interactions. *Biophys Rev*. 5:29-39.

Ladwein, M., U.F. Pape, D.S. Schmidt, M. Schnolzer, S. Fiedler, L. Langbein, W.W. Franke, G. Moldenhauer, and M. Zoller. 2005. The cell-cell adhesion molecule EpCAM interacts directly with the tight junction protein claudin-7. *Exp Cell Res*. 309:345-357.

Lea, T. 2015. Caco-2 Cell Line. *In* The Impact of Food Bioactives on Health: in vitro and ex vivo models. K. Verhoeckx, P. Cotter, I. Lopez-Exposito, C. Kleiveland, T. Lea, A. Mackie, T. Requena, D. Swiatecka, and H. Wichers, editors, Cham (CH). 103-111.

Leerberg, J.M., G.A. Gomez, S. Verma, E.J. Moussa, S.K. Wu, R. Priya, B.D. Hoffman, C. Grashoff, M.A. Schwartz, and A.S. Yap. 2014. Tension-sensitive actin assembly supports contractility at the epithelial zonula adherens. *Curr Biol*. 24:1689-1699.

Lei, Z., T. Maeda, A. Tamura, T. Nakamura, Y. Yamazaki, H. Shiratori, K. Yashiro, S. Tsukita, and H. Hamada. 2012. EpCAM contributes to formation of functional tight junction in the intestinal epithelium by recruiting claudin proteins. *Dev Biol*. 371:136-145.

Li, J., Y. He, Q. Lu, and M. Zhang. 2016. Mechanistic Basis of Organization of the Harmonin/USH1C-Mediated Brush Border Microvilli Tip-Link Complex. *Dev Cell*. 36:179-189.

Li, J., Y. He, M.L. Weck, Q. Lu, M.J. Tyska, and M. Zhang. 2017. Structure of Myo7b/USH1C complex suggests a general PDZ domain binding mode by MyTH4-FERM myosins. *Proc Natl Acad Sci U S A*. 114:E3776-E3785.

Li, J., J. Li, Jr., S.Y. Zhang, R.X. Li, X. Lin, Y.L. Mi, and C.Q. Zhang. 2018. Culture and characterization of chicken small intestinal crypts. *Poult Sci*. 97:1536-1543.

Liu, K.C., and R.E. Cheney. 2012. Myosins in cell junctions. *Bioarchitecture*. 2:158-170.

Loomis, P.A., L. Zheng, G. Sekerkova, B. Changyaleket, E. Mugnaini, and J.R. Bartles. 2003. Espin cross-links cause the elongation of microvillus-type parallel actin bundles in vivo. *J Cell Biol*. 163:1045-1055.

Losi, L., C. Lancellotti, S. Parenti, L. Scurani, T. Zanocco-Marani, F. Buffoli, R. Grassia, S. Ferrari, and A. Grande. 2019. Loss of expression of mu-protocadherin and protocadherin-24 in sporadic and hereditary nonpolyposis colorectal cancers. *Hum Pathol*. 84:299-308.

Losi, L., S. Parenti, F. Ferrarini, F. Rivasi, M. Gavioli, G. Natalini, S. Ferrari, and A. Grande. 2011. Down-regulation of mu-protocadherin expression is a common event in colorectal carcinogenesis. *Hum Pathol*. 42:960-971.

Louvard, D., M. Kedinger, and H.P. Hauri. 1992. The differentiating intestinal epithelial cell: establishment and maintenance of functions through interactions between cellular structures. *Annu Rev Cell Biol*. 8:157-195.

Lynn, K.S., R.J. Peterson, and M. Koval. 2020. Ruffles and spikes: Control of tight junction morphology and permeability by claudins. *Biochim Biophys Acta Biomembr*. 1862:183339.

Madara, J.L., D. Barenberg, and S. Carlson. 1986. Effects of cytochalasin D on occluding junctions of intestinal absorptive cells: further evidence that the cytoskeleton may influence paracellular permeability and junctional charge selectivity. *J Cell Biol*. 102:2125-2136.

Mangeol, P., D. Massey-Harroche, F. Richard, J.P. Concordet, P.F. Lenne, and A. Le Bivic. 2022. Super-resolution imaging uncovers the nanoscopic segregation of polarity proteins in epithelia. *Elife*. 11.

Manor, U., A. Disanza, M. Grati, L. Andrade, H. Lin, P.P. Di Fiore, G. Scita, and B. Kachar. 2011. Regulation of stereocilia length by myosin XVa and whirlin depends on the actin-regulatory protein Eps8. *Curr Biol*. 21:167-172.

Manor, U., and B. Kachar. 2008. Dynamic length regulation of sensory stereocilia. *Semin Cell Dev Biol*. 19:502-510.

Matoo, S., M.J. Graves, M.S. Choi, R.A.E.S. Idris, P. Acharya, G. Thapa, T. Nguyen, S.Y. Atallah, A.K. Tipirneni, P.J. Stevenson, and S.W. Crawley. 2023. Isoform-specific targeting properties of the protocadherin CDHR5 control its apical delivery to promote brush border assembly. *bioRxiv*:2023.2002.2022.529570.

Mazerik, J.N., L.J. Kraft, A.K. Kenworthy, and M.J. Tyska. 2014. Motor and tail homology 1 (Th1) domains antagonistically control myosin-1 dynamics. *Biophys J*. 106:649-658.

Mazerik, J.N., and M.J. Tyska. 2012. Myosin-1A targets to microvilli using multiple membrane binding motifs in the tail homology 1 (TH1) domain. *J Biol Chem*. 287:13104-13115.

McConnell, R.E., A.E. Benesh, S. Mao, D.L. Tabb, and M.J. Tyska. 2011. Proteomic analysis of the enterocyte brush border. *American journal of physiology. Gastrointestinal and liver physiology*. 300:G914-926.

McGuckin, M.A., R. Eri, L.A. Simms, T.H. Florin, and G. Radford-Smith. 2009. Intestinal barrier dysfunction in inflammatory bowel diseases. *Inflamm Bowel Dis*. 15:100-113.

Meenderink, L.M., I.M. Gaeta, M.M. Postema, C.S. Cencer, C.R. Chinowsky, E.S. Krystofiak, B.A. Millis, and M.J. Tyska. 2019. Actin Dynamics Drive Microvillar Motility and Clustering during Brush Border Assembly. *Dev Cell*. 50:545-556 e544.

Meng, W., and M. Takeichi. 2009. Adherens junction: molecular architecture and regulation. *Cold Spring Harb Perspect Biol*. 1:a002899.

Mogilner, A., and B. Rubinstein. 2005. The physics of filopodial protrusion. *Biophys J*. 89:782-795.

Mooseker, M.S., T.A. Graves, K.A. Wharton, N. Falco, and C.L. Howe. 1980. Regulation of microvillus structure: calcium-dependent solation and cross-linking of actin filaments in the microvilli of intestinal epithelial cells. *J Cell Biol*. 87:809-822.

Mooseker, M.S., and L.G. Tilney. 1975. Organization of an actin filament-membrane complex. Filament polarity and membrane attachment in the microvilli of intestinal epithelial cells. *J Cell Biol*. 67:725-743.

Morales, E.A., C. Arnaiz, E.S. Krystofiak, M. Zanic, and M.J. Tyska. 2022. Mitotic Spindle Positioning (MISP) is an actin bundler that selectively stabilizes the rootlets of epithelial microvilli. *Cell Rep*. 39:110692.

Moulton, D.E., W. Crandall, R. Lakhani, and M.E. Lowe. 2004. Expression of a novel cadherin in the mouse and human intestine. *Pediatr Res*. 55:927-934.

Narai, A., S. Arai, and M. Shimizu. 1997. Rapid decrease in transepithelial electrical resistance of human intestinal Caco-2 cell monolayers by cytotoxic membrane perturbents. *Toxicol In Vitro*. 11:347-354.

Nepal, B., A. Sepehri, and T. Lazaridis. 2021. Mechanism of negative membrane curvature generation by I-BAR domains. *Structure*. 29:1440-1452 e1444.

Nielsen, R., H. Birn, S.K. Moestrup, M. Nielsen, P. Verroust, and E.I. Christensen. 1998. Characterization of a kidney proximal tubule cell line, LLC-PK1, expressing endocytotic active megalin. *J Am Soc Nephrol*. 9:1767-1776.

Nielsen, R., B.S. Sorensen, H. Birn, E.I. Christensen, and E. Nexo. 2001. Transcellular transport of vitamin B(12) in LLC-PK1 renal proximal tubule cells. *J Am Soc Nephrol*. 12:1099-1106.

Niggli, V., C. Andreoli, C. Roy, and P. Mangeat. 1995. Identification of a phosphatidylinositol-4,5-bisphosphate-binding domain in the N-terminal region of ezrin. *FEBS Lett*. 376:172-176.

Oda, H., and M. Takeichi. 2011. Evolution: structural and functional diversity of cadherin at the adherens junction. *J Cell Biol*. 193:1137-1146.

Odenwald, M.A., W. Choi, W.T. Kuo, G. Singh, A. Sailer, Y. Wang, L. Shen, A.S. Fanning, and J.R. Turner. 2018. The scaffolding protein ZO-1 coordinates actomyosin and epithelial apical specializations in vitro and in vivo. *J Biol Chem*. 293:17317-17335.

Ohta, K., R. Higashi, A. Sawaguchi, and K. Nakamura. 2012. Helical arrangement of filaments in microvillar actin bundles. *Journal of structural biology*. 177:513-519.

Okazaki, N., N. Takahashi, S. Kojima, Y. Masuho, and H. Koga. 2002. Protocadherin LKC, a new candidate for a tumor suppressor of colon and liver cancers, its association with contact inhibition of cell proliferation. *Carcinogenesis*. 23:1139-1148.

Ose, R., T. Yanagawa, S. Ikeda, O. Ohara, and H. Koga. 2009. PCDH24-induced contact inhibition involves downregulation of beta-catenin signaling. *Mol Oncol*. 3:54-66.

Pan, L., and M. Zhang. 2012. Structures of usher syndrome 1 proteins and their complexes. *Physiology (Bethesda)*. 27:25-42.

Pantaloni, D., C. Le Clainche, and M.F. Carlier. 2001. Mechanism of actin-based motility. *Science*. 292:1502-1506.

Paradis, T., H. Begue, L. Basmaciyan, F. Dalle, and F. Bon. 2021. Tight Junctions as a Key for Pathogens Invasion in Intestinal Epithelial Cells. *Int J Mol Sci*. 22.

Paul, A.S., and T.D. Pollard. 2009. Energetic requirements for processive elongation of actin filaments by FH1FH2-formins. *J Biol Chem*. 284:12533-12540.

Paunola, E., P.K. Mattila, and P. Lappalainen. 2002. WH2 domain: a small, versatile adapter for actin monomers. *FEBS Lett*. 513:92-97.

Pedersen, G.A., H.H. Jensen, A.B. Schelde, C. Toft, H.N. Pedersen, M. Ulrichsen, F.H. Login, M.R. Amieva, and L.N. Nejsum. 2017. The basolateral vesicle sorting machinery and basolateral proteins are recruited to the site of enteropathogenic E. coli microcolony growth at the apical membrane. *PLoS One*. 12:e0179122.

Perantoni, A., and J.J. Berman. 1979. Properties of Wilms' tumor line (TuWi) and pig kidney line (LLC-PK1) typical of normal kidney tubular epithelium. *In Vitro*. 15:446-454.

Perrin, B.J., and J.M. Ervasti. 2010. The actin gene family: function follows isoform. *Cytoskeleton (Hoboken)*. 67:630-634.

Peterson, M.D., and M.S. Mooseker. 1992. Characterization of the enterocyte-like brush border cytoskeleton of the C2BBe clones of the human intestinal cell line, Caco-2. *J Cell Sci*. 102 (Pt 3):581-600.

Peterson, M.D., and M.S. Mooseker. 1993. An in vitro model for the analysis of intestinal brush border assembly. I. Ultrastructural analysis of cell contact-induced brush border assembly in Caco-2BBe cells. *J Cell Sci*. 105 (Pt 2):445-460.

Pettersen, E.F., T.D. Goddard, C.C. Huang, E.C. Meng, G.S. Couch, T.I. Croll, J.H. Morris, and T.E. Ferrin. 2021. UCSF ChimeraX: Structure visualization for researchers, educators, and developers. *Protein Sci*. 30:70-82.

Pinette, J.A., S. Mao, B.A. Millis, E.S. Krystofiak, J.J. Faust, and M.J. Tyska. 2019. Brush border protocadherin CDHR2 promotes the elongation and maximized packing of microvilli in vivo. *Mol Biol Cell*. 30:108-118.

Pinheiro, D., and Y. Bellaiche. 2018. Mechanical Force-Driven Adherens Junction Remodeling and Epithelial Dynamics. *Dev Cell*. 47:3-19.

Pinheiro, D., and Y. Bellaïche. 2018. Mechanical Force-Driven Adherens Junction Remodeling and Epithelial Dynamics. *Dev Cell*. 47:3-19.

Pokutta, S., and W.I. Weis. 2007. Structure and mechanism of cadherins and catenins in cell-cell contacts. *Annu Rev Cell Dev Biol*. 23:237-261.

Pollard, T.D. 1986. Rate constants for the reactions of ATP- and ADP-actin with the ends of actin filaments. *J Cell Biol*. 103:2747-2754.

Pollard, T.D., and G.G. Borisy. 2003. Cellular motility driven by assembly and disassembly of actin filaments. *Cell*. 112:453-465.

Postema, M.M., N.E. Grega-Larson, A.C. Neininger, and M.J. Tyska. 2018. IRTKS (BAIAP2L1) Elongates Epithelial Microvilli Using EPS8-Dependent and Independent Mechanisms. *Curr Biol*. 28:2876-2888 e2874.

Pouliot, Y. 1992. Phylogenetic analysis of the cadherin superfamily. *Bioessays*. 14:743-748.

Qian, H., M.P. Sheetz, and E.L. Elson. 1991. Single particle tracking. Analysis of diffusion and flow in two-dimensional systems. *Biophys J*. 60:910-921.

Rakshit, S., Y. Zhang, K. Manibog, O. Shafraz, and S. Sivasankar. 2012. Ideal, catch, and slip bonds in cadherin adhesion. *Proc Natl Acad Sci U S A*. 109:18815-18820.

Rao, Y., and V. Haucke. 2011. Membrane shaping by the Bin/amphiphysin/Rvs (BAR) domain protein superfamily. *Cell Mol Life Sci*. 68:3983-3993.

Revenu, C., F. Ubelmann, I. Hurbain, F. El-Marjou, F. Dingli, D. Loew, D. Delacour, J. Gilet, E. Brot-Laroche, F. Rivero, D. Louvard, and S. Robine. 2012. A new role for the architecture of microvillar actin bundles in apical retention of membrane proteins. *Mol Biol Cell*. 23:324-336.

Rice, W.L., A.N. Van Hoek, T.G. Paunescu, C. Huynh, B. Goetze, B. Singh, L. Scipioni, L.A. Stern, and D. Brown. 2013. High resolution helium ion scanning microscopy of the rat kidney. *PLoS One*. 8:e57051.

Rodgers, L.S., M.T. Beam, J.M. Anderson, and A.S. Fanning. 2013. Epithelial barrier assembly requires coordinated activity of multiple domains of the tight junction protein ZO-1. *J Cell Sci*. 126:1565-1575.

Rogez, B., L. Wurthner, A.B. Petrova, F.B. Zierhut, D. Saczko-Brack, M.A. Huergo, C. Batters, E. Frey, and C. Veigel. 2019. Reconstitution reveals how myosin-VI self-organises to generate a dynamic mechanism of membrane sculpting. *Nat Commun*. 10:3305.

Rousset, M. 1986. The human colon carcinoma cell lines HT-29 and Caco-2: two in vitro models for the study of intestinal differentiation. *Biochimie*. 68:1035-1040.

Roxas, J.L., A. Koutsouris, A. Bellmeyer, S. Tesfay, S. Royan, K. Falzari, A. Harris, H. Cheng, K.J. Rhee, and G. Hecht. 2010. Enterohemorrhagic E. coli alters murine intestinal epithelial tight junction protein expression and barrier function in a Shiga toxin independent manner. *Lab Invest*. 90:1152-1168.

Roy, P., and B.J. Perrin. 2018. The stable actin core of mechanosensory stereocilia features continuous turnover of actin cross-linkers. *Mol Biol Cell*. 29:1856-1865.

Rzadzinska, A.K., M.E. Schneider, C. Davies, G.P. Riordan, and B. Kachar. 2004. An actin molecular treadmill and myosins maintain stereocilia functional architecture and self-renewal. *J Cell Biol*. 164:887-897.

Saito, M., D.K. Tucker, D. Kohlhorst, C.M. Niessen, and A.P. Kowalczyk. 2012. Classical and desmosomal cadherins at a glance. *J Cell Sci*. 125:2547-2552.

Sakaguchi, H., J. Tokita, U. Muller, and B. Kachar. 2009. Tip links in hair cells: molecular composition and role in hearing loss. *Curr Opin Otolaryngol Head Neck Surg*. 17:388-393.

Sauvanet, C., J. Wayt, T. Pelaseyed, and A. Bretscher. 2015. Structure, regulation, and functional diversity of microvilli on the apical domain of epithelial cells. *Annu Rev Cell Dev Biol*. 31:593-621.

Sept, D., and J.A. McCammon. 2001. Thermodynamics and kinetics of actin filament nucleation. *Biophys J*. 81:667-674.

Shapiro, L., A.M. Fannon, P.D. Kwong, A. Thompson, M.S. Lehmann, G. Grubel, J.F. Legrand, J. Als-Nielsen, D.R. Colman, and W.A. Hendrickson. 1995. Structural basis of cell-cell adhesion by cadherins. *Nature*. 374:327-337.

Sheetz, M.P., S. Turney, H. Qian, and E.L. Elson. 1989. Nanometre-level analysis demonstrates that lipid flow does not drive membrane glycoprotein movements. *Nature*. 340:284-288.

Shen, L., C.R. Weber, and J.R. Turner. 2008. The tight junction protein complex undergoes rapid and continuous molecular remodeling at steady state. *J Cell Biol*. 181:683-695.

Shifrin, D.A., Jr., S.W. Crawley, N.E. Grega-Larson, and M.J. Tyska. 2014. Dynamics of brush border remodeling induced by enteropathogenic E. coli. *Gut Microbes*. 5:504-516.

Shifrin, D.A., Jr., R.E. McConnell, R. Nambiar, J.N. Higginbotham, R.J. Coffey, and M.J. Tyska. 2012. Enterocyte microvillus-derived vesicles detoxify bacterial products and regulate epithelial-microbial interactions. *Curr Biol*. 22:627-631.

Skamrahl, M., H. Pang, M. Ferle, J. Gottwald, A. Rubeling, R. Maraspini, A. Honigmann, T.A. Oswald, and A. Janshoff. 2021. Tight Junction ZO Proteins Maintain Tissue Fluidity, Ensuring Efficient Collective Cell Migration. *Adv Sci (Weinh)*. 8:e2100478.

Sokurenko, E.V., V. Vogel, and W.E. Thomas. 2008. Catch-bond mechanism of force-enhanced adhesion: counterintuitive, elusive, but ... widespread? *Cell Host Microbe*. 4:314-323.

Sotomayor, M., R. Gaudet, and D.P. Corey. 2014. Sorting out a promiscuous superfamily: towards cadherin connectomics. *Trends Cell Biol*. 24:524-536.

Specian, R.D., and M.R. Neutra. 1981. The surface topography of the colonic crypt in rabbit and monkey. *The American journal of anatomy*. 160:461-472.

Srinivasan, B., A.R. Kolli, M.B. Esch, H.E. Abaci, M.L. Shuler, and J.J. Hickman. 2015. TEER measurement techniques for in vitro barrier model systems. *J Lab Autom*. 20:107-126.

Steinmassl, D., W. Pfaller, G. Gstraunthaler, and W. Hoffmann. 1995. LLC-PK1 epithelia as a model for in vitro assessment of proximal tubular nephrotoxicity. *In Vitro Cell Dev Biol Anim*. 31:94-106.

Stevens, J.M., E.E. Galyov, and M.P. Stevens. 2006. Actin-dependent movement of bacterial pathogens. *Nat Rev Microbiol*. 4:91-101.

Stevenson, B.R., J.D. Siliciano, M.S. Mooseker, and D.A. Goodenough. 1986. Identification of ZO-1: a high molecular weight polypeptide associated with the tight junction (zonula occludens) in a variety of epithelia. *J Cell Biol*. 103:755-766.

Sullivan, L.H. 1896. The Tall Office Buildign Artistically Considered. *In* Lippincott's Magazine Vol. 57. 403-409.

Sumi, A., P. Hayes, A. D'Angelo, J. Colombelli, G. Salbreux, K. Dierkes, and J. Solon. 2018. Adherens Junction Length during Tissue Contraction Is Controlled by the Mechanosensitive Activity of Actomyosin and Junctional Recycling. *Dev Cell*. 47:453-463 e453.

Suraneni, P., B. Rubinstein, J.R. Unruh, M. Durnin, D. Hanein, and R. Li. 2012. The Arp2/3 complex is required for lamellipodia extension and directional fibroblast cell migration. *J Cell Biol*. 197:239-251.

Svitkina, T.M., E.A. Bulanova, O.Y. Chaga, D.M. Vignjevic, S. Kojima, J.M. Vasiliev, and G.G. Borisy. 2003. Mechanism of filopodia initiation by reorganization of a dendritic network. *J Cell Biol*. 160:409-421.

Takeichi, M. 1977. Functional correlation between cell adhesive properties and some cell surface proteins. *J Cell Biol*. 75:464-474.

Takeichi, M. 1995. Morphogenetic roles of classic cadherins. *Curr Opin Cell Biol*. 7:619-627.

Takeichi, M. 2018. Historical review of the discovery of cadherin, in memory of Tokindo Okada. *Dev Growth Differ*. 60:3-13.

Thomas, W. 2006. For catch bonds, it all hinges on the interdomain region. *J Cell Biol*. 174:911-913.

Thomas, W. 2008. Catch bonds in adhesion. *Annu Rev Biomed Eng*. 10:39-57.

Tian, X., Z. Liu, B. Niu, J. Zhang, T.K. Tan, S.R. Lee, Y. Zhao, D.C. Harris, and G. Zheng. 2011. E-cadherin/beta-catenin complex and the epithelial barrier. *J Biomed Biotechnol*. 2011:567305.

Tilney, L.G., and R.R. Cardell. 1970. Factors controlling the reassembly of the microvillous border of the small intestine of the salamander. *J Cell Biol*. 47:408-422.

Tilney, L.G., and D.J. DeRosier. 1986. Actin filaments, stereocilia, and hair cells of the bird cochlea. IV. How the actin filaments become organized in developing stereocilia and in the cuticular plate. *Dev Biol*. 116:119-129.

Tilney, L.G., D.J. Derosier, and M.J. Mulroy. 1980. The organization of actin filaments in the stereocilia of cochlear hair cells. *J Cell Biol*. 86:244-259.

Tilney, L.G., M.S. Tilney, and D.J. DeRosier. 1992. Actin filaments, stereocilia, and hair cells: how cells count and measure. *Annu Rev Cell Biol*. 8:257-274.

Tocchetti, A., C.B. Soppo, F. Zani, F. Bianchi, M.C. Gagliani, B. Pozzi, J. Rozman, R. Elvert, N. Ehrhardt, B. Rathkolb, C. Moerth, M. Horsch, H. Fuchs, V. Gailus-Durner, J. Beckers, M. Klingenspor, E. Wolf, M. Hrabe de Angelis, E. Scanziani, C. Tacchetti, G. Scita, P.P. Di Fiore, and N. Offenhauser. 2010. Loss of the actin remodeler Eps8 causes intestinal defects and improved metabolic status in mice. *PLoS One*. 5:e9468.

Tokuda, S., T. Higashi, and M. Furuse. 2014. ZO-1 knockout by TALEN-mediated gene targeting in MDCK cells: involvement of ZO-1 in the regulation of cytoskeleton and cell shape. *PLoS One*. 9:e104994.

Trier, J.S. 1963. Studies on Small Intestinal Crypt Epithelium. I. The Fine Structure of the Crypt Epithelium of the Proximal Small Intestine of Fasting Humans. *J Cell Biol*. 18:599-620.

Turner, J.R., B.K. Rill, S.L. Carlson, D. Carnes, R. Kerner, R.J. Mrsny, and J.L. Madara. 1997. Physiological regulation of epithelial tight junctions is associated with myosin light-chain phosphorylation. *Am J Physiol*. 273:C1378-1385.

Turpin, W., S.H. Lee, J.A. Raygoza Garay, K.L. Madsen, J.B. Meddings, L. Bedrani, N. Power, O. Espin-Garcia, W. Xu, M.I. Smith, A.M. Griffiths, P. Moayyedi, D. Turner, E.G. Seidman, A.H. Steinhart, J.K. Marshall, K. Jacobson, D. Mack, H. Huynh, C.N. Bernstein, A.D. Paterson, Crohn's, C. Colitis Canada Genetic Environmental Microbial Project Research, C.G.P.r.s.d.i.M. Abreu, and K. Croitoru. 2020. Increased Intestinal Permeability Is Associated With Later Development of Crohn's Disease. *Gastroenterology*. 159:2092-2100 e2095.

Tyska, M.J., A.T. Mackey, J.D. Huang, N.G. Copeland, N.A. Jenkins, and M.S. Mooseker. 2005. Myosin-1a is critical for normal brush border structure and composition. *Mol Biol Cell*. 16:2443-2457.

Valenta, T., G. Hausmann, and K. Basler. 2012. The many faces and functions of beta-catenin. *EMBO J*. 31:2714-2736.

van der Flier, L.G., and H. Clevers. 2009. Stem cells, self-renewal, and differentiation in the intestinal epithelium. *Annu Rev Physiol*. 71:241-260.

Van Itallie, C.M., and J.M. Anderson. 2014. Architecture of tight junctions and principles of molecular composition. *Semin Cell Dev Biol*. 36:157-165.

Van Itallie, C.M., A.S. Fanning, A. Bridges, and J.M. Anderson. 2009. ZO-1 stabilizes the tight junction solute barrier through coupling to the perijunctional cytoskeleton. *Mol Biol Cell*. 20:3930-3940.

VanDussen, K.L., A. Stojmirovic, K. Li, T.C. Liu, P.K. Kimes, B.D. Muegge, K.F. Simpson, M.A. Ciorba, J.G. Perrigoue, J.R. Friedman, J.E. Towne, R.D. Head, and T.S. Stappenbeck. 2018. Abnormal Small Intestinal Epithelial Microvilli in Patients With Crohn's Disease. *Gastroenterology*. 155:815-828.

Vanslembrouck, B., J.H. Chen, C. Larabell, and J. van Hengel. 2022. Microscopic Visualization of Cell-Cell Adhesion Complexes at Micro and Nanoscale. *Front Cell Dev Biol*. 10:819534.

Velle, K.B., and K.G. Campellone. 2017. Extracellular motility and cell-to-cell transmission of enterohemorrhagic E. coli is driven by EspFU-mediated actin assembly. *PLoS Pathog*. 13:e1006501.

Venkatachalam, M.A., D.B. Bernard, J.F. Donohoe, and N.G. Levinsky. 1978. Ischemic damage and repair in the rat proximal tubule: differences among the S1, S2, and S3 segments. *Kidney Int*. 14:31-49.

Verpy, E., M. Leibovici, I. Zwaenepoel, X.Z. Liu, A. Gal, N. Salem, A. Mansour, S. Blanchard, I. Kobayashi, B.J. Keats, R. Slim, and C. Petit. 2000. A defect in harmonin, a PDZ domain-containing protein expressed in the inner ear sensory hair cells, underlies Usher syndrome type 1C. *Nat Genet*. 26:51-55.

Volkmann, N., K.J. Amann, S. Stoilova-McPhie, C. Egile, D.C. Winter, L. Hazelwood, J.E. Heuser, R. Li, T.D. Pollard, and D. Hanein. 2001. Structure of Arp2/3 complex in its activated state and in actin filament branch junctions. *Science*. 293:2456-2459.

Weck, M.L., S.W. Crawley, C.R. Stone, and M.J. Tyska. 2016. Myosin-7b Promotes Distal Tip Localization of the Intermicrovillar Adhesion Complex. *Curr Biol*. 26:2717-2728.

Wegner, A. 1976. Head to tail polymerization of actin. *J Mol Biol*. 108:139-150.

Wei, Q., and H. Huang. 2013. Insights into the role of cell-cell junctions in physiology and disease. *Int Rev Cell Mol Biol*. 306:187-221.

Weinman, M.D., C.H. Allan, J.S. Trier, and S.J. Hagen. 1989. Repair of microvilli in the rat small intestine after damage with lectins contained in the red kidney bean. *Gastroenterology*. 97:1193-1204.

Welling, L.W., and D.J. Welling. 1975. Surface areas of brush border and lateral cell walls in the rabbit proximal nephron. *Kidney Int*. 8:343-348.

Wessely, O., D.M. Cerqueira, U. Tran, V. Kumar, J.M. Hassey, and D. Romaker. 2014. The bigger the better: determining nephron size in kidney. *Pediatr Nephrol*. 29:525-530.

Whatley, M., A. Francis, Z.Y. Ng, X.E. Khoh, M.D. Atlas, R.J. Dilley, and E.Y.M. Wong. 2020. Usher Syndrome: Genetics and Molecular Links of Hearing Loss and Directions for Therapy. *Front Genet*. 11:565216.

Winkelman, J.D., C.G. Bilancia, M. Peifer, and D.R. Kovar. 2014. Ena/VASP Enabled is a highly processive actin polymerase tailored to self-assemble parallel-bundled F-actin networks with Fascin. *Proc Natl Acad Sci U S A*. 111:4121-4126.

Wolverton, T., and M. Lalande. 2001. Identification and characterization of three members of a novel subclass of protocadherins. *Genomics*. 76:66-72.

Wu, C.J., P. Mannan, M. Lu, and M.C. Udey. 2013. Epithelial cell adhesion molecule (EpCAM) regulates claudin dynamics and tight junctions. *J Biol Chem*. 288:12253-12268.

Wu, S.K., G.A. Gomez, M. Michael, S. Verma, H.L. Cox, J.G. Lefevre, R.G. Parton, N.A. Hamilton, Z. Neufeld, and A.S. Yap. 2014. Cortical F-actin stabilization generates apical-

lateral patterns of junctional contractility that integrate cells into epithelia. *Nat Cell Biol*. 16:167-178.

Wyatt, J., H. Vogelsang, W. Hubl, T. Waldhoer, and H. Lochs. 1993. Intestinal permeability and the prediction of relapse in Crohn's disease. *Lancet*. 341:1437-1439.

Yan, W., G. Chen, and J. Li. 2022. Structure of the Harmonin PDZ2 and coiled-coil domains in a complex with CDHR2 tail and its implications. *FASEB J*. 36:e22425.

Yap, A.S. 1998. The morphogenetic role of cadherin cell adhesion molecules in human cancer: a thematic review. *Cancer Invest*. 16:252-261.

Yuan, L., H.C. van der Mei, H.J. Busscher, and B.W. Peterson. 2020. Two-Stage Interpretation of Changes in TEER of Intestinal Epithelial Layers Protected by Adhering Bifidobacteria During E. coli Challenges. *Front Microbiol*. 11:599555.

Zampini, V., L. Ruttiger, S.L. Johnson, C. Franz, D.N. Furness, J. Waldhaus, H. Xiong, C.M. Hackney, M.C. Holley, N. Offenhauser, P.P. Di Fiore, M. Knipper, S. Masetto, and W. Marcotti. 2011. Eps8 regulates hair bundle length and functional maturation of mammalian auditory hair cells. *PLoS Biol*. 9:e1001048.

Zhang, D.S., V. Piazza, B.J. Perrin, A.K. Rzadzinska, J.C. Poczatek, M. Wang, H.M. Prosser, J.M. Ervasti, D.P. Corey, and C.P. Lechene. 2012. Multi-isotope imaging mass spectrometry reveals slow protein turnover in hair-cell stereocilia. *Nature*. 481:520-524.

Zhao, H., A. Pykalainen, and P. Lappalainen. 2011. I-BAR domain proteins: linking actin and plasma membrane dynamics. *Curr Opin Cell Biol*. 23:14-21.

Zhuo, J.L., and X.C. Li. 2013. Proximal nephron. *Compr Physiol*. 3:1079-1123.